

A FULLY-DIFFERENTIAL BULK-MICROMACHINED MEMS  
ACCELEROMETER WITH INTERDIGITATED FINGERS

A THESIS SUBMITTED TO  
THE GRADUATE SCHOOL OF NATURAL AND APPLIED SCIENCES  
OF  
MIDDLE EAST TECHNICAL UNIVERSITY

BY

OSMAN AYDIN

IN PARTIAL FULFILLMENT OF THE REQUIREMENTS  
FOR  
THE DEGREE OF MASTER OF SCIENCE  
IN  
ELECTRICAL AND ELECTRONICS ENGINEERING

FEBRUARY 2012

Approval of the thesis:

**A FULLY-DIFFERENTIAL BULK-MICROMACHINED MEMS  
ACCELEROMETER WITH INTERDIGITATED FINGERS**

submitted by **OSMAN AYDIN** in partial fulfillment of the requirements for the degree of **Master of Science in Electrical and Electronics Engineering Department, Middle East Technical University** by,

Prof. Dr. Canan Özgen  
Dean, Graduate School of **Natural and Applied Sciences**

\_\_\_\_\_

Prof. Dr. İsmet Erkmén  
Head of Department, **Electrical and Electronics Eng.**

\_\_\_\_\_

Prof. Dr. Tayfun Akın  
Supervisor, **Electrical and Electronics Eng. Dept., METU**

\_\_\_\_\_

**Examining Committee Members**

Prof. Dr. Mehmet Ali Sahir Arıkan  
Mechanical Eng. Dept., METU

\_\_\_\_\_

Prof. Dr. Tayfun Akın  
Electrical and Electronics Eng. Dept., METU

\_\_\_\_\_

Assoc. Prof. Dr. Haluk Klah  
Electrical and Electronics Eng. Dept., METU

\_\_\_\_\_

Assist. Prof. Dr. Barıř Bayram  
Electrical and Electronics Eng. Dept., METU

\_\_\_\_\_

Dr. Said Emre Alper  
Technical Vocational School of Higher Education, METU

\_\_\_\_\_

**Date:** 09.02.2012

**I hereby declare that all information in this document has been obtained and presented in accordance with academic rules and ethical conduct. I also declare that, as required by these rules and conduct, I have fully cited and referenced all referenced material and results that are not original to this work.**

Name, Surname: Osman AYDIN

Signature:

# ABSTRACT

## A FULLY-DIFFERENTIAL BULK-MICROMACHINED MEMS ACCELEROMETER WITH INTERDIGITATED FINGERS

Aydın, Osman

M. Sc., Department of Electrical and Electronics Engineering

Supervisor: Prof. Dr. Tayfun Akın

February 2012, 107 pages

Accelerometer sensors fabricated with micromachining technologies started to take place of yesterday's bulky sensors in many application areas. The application areas include a wide range from consumer electronics and health systems to military and aerospace applications. Therefore, the performance requirements extend from  $1 \mu\text{g}$ 's to 100 thousand  $\text{g}$ 's. However, high performance strategic grade MEMS accelerometer sensors still do not exist in the literature. Smart designs utilizing the MEMS technology is necessary in order to acquire high performance specifications.

This thesis reports a high performance accelerometer with a new process by making the use of bulk-micromachining technology. The new process includes the utilization of Silicon-on-Insulator (SOI) wafer and its buried oxide (BOX) layer. The BOX layer helps to realize interdigitated finger structures, which commonly find place in surface-micromachined CMOS-MEMS capacitive accelerometers. The

multi-metal layered CMOS-MEMS devices inherently incorporate interdigitated finger structures. Interdigitated finger structures are highly sensitive to acceleration in comparison with comb-finger structures, which generally find usage in bulk-micromachined devices, due to absence of anti-gap. The designed sensors based on this fabrication process is sought to form a fully-differential signal interfaced sensor with incorporation of the advantages of high sensitive interdigitated finger electrodes and high aspect ratio SOI wafer's bulk single crystal silicon device.

Under the light of the envisaged process, sensor designs were made, and verified using a computing environment, MATLAB, and a finite element analysis simulator, CoventorWARE. The verified two designs were fabricated, and all the tests, except the centrifuge test, were made at METU-MEMS Research Center. Among the fabricated sensors, the one designed for the high performance achieves a capacitance sensitivity of 178 fF with a rest capacitance of 8.1 pF by employing interdigitated finger electrodes, while its comb-finger implementation can only achieve a capacitance sensitivity of 75 fF with a rest capacitance of 10 pF.

Key Words: Micro Electro Mechanical Systems (MEMS), Bulk-Micromachined Accelerometer, Fully-Differential Finger Structure, Silicon-on-Insulator (SOI) Wafer.

# ÖZ

## İÇİÇE GEÇMİŞ PARMAKLAR İLE TAM-DİFERANSİYEL GÖVDE-MİKROİŞLENMİŞ MEMS İVMEÖLÇER

Aydın, Osman

Yüksek Lisans, Elektrik ve Elektronik Mühendisliği Bölümü

Tez Yöneticisi: Prof. Dr. Tayfun Akın

Şubat 2012, 107 sayfa

Mikroişleme teknolojisi ile üretilen ivmeölçer pek çok uygulama alanında dünün hantal duyargaların yerine geçmeye başladı. Uygulama alanları tüketici elektroniği ve sağlık sistemlerinden askeri ve hava-uzay uygulamalarına kadar geniş bir alanı kapsar. Bu yüzden, başarımların gereksinimleri 1 µg'den 100 binlerce g değerine uzanabilir. Yine de literatürde yüksek başarımlı stratejik seviye MEMS ivmeölçer duyargalar bulunmamaktadır. Yüksek başarımlı özelliklerini elde etmek için mevcut teknolojileri kullanan akıllı tasarımlar gerekmektedir.

Bu tez kütle işleme teknolojisinden faydalanarak yeni bir işleme ile yüksek performanslı bir duyarga rapor etmektedir. Yeni işleme Yalıtkan-Üstü-Silisyum (YÜS) pul ve onun gömülü oksit tabakasını kullanmayı içermektedir. Gömülü oksit tabakası yüzey-işlenmiş CMOS-MEMS kapasitif ivmeölçerlerde oldukça sık kullanılan içiçe geçmiş parmak yapısını gerçekleştirmeye yardım etmektedir. Oksit tabakası üstünden alınacak bağlantılarla CMOS-MEMS ivmeölçerlerdeki çok katlı

metal yapı oluşturulmaktadır. Çoklu metal tabakalı CMOS-MEMS cihazlar doğal olarak içiçe geçmiş parmak yapıları içerir. İçiçe geçmiş parmak yapıları genellikle kütle mikroişlemeli cihazlarda kullanılmakta olan taraklı parmak yapılara nazaran ivmeye oldukça duyarlıdır. Bu üretim işlemine dayandırılarak tasarlanan duyargaların yüksek hassasiyetli içiçe geçmiş parmak elektrotlarını ve yüksek cephe oranlı YÜS pulun kütleli tek kristal silisyum yapısal tabakasının avantajlarından faydalanarak tam diferansiyel sinyal arayüzlü bir duyarga üretmek amaçlanmıştır.

Öngörölmüş işlemenin ışığı altında duyarga tasarımları yapılmış ve MATLAB hesaplama ortamı ile CoventorWARE sonlu elaman analiz benzetisinde doğrulanmıştır. Doğrulanmış iki tasarım üretilmiş ve merkezkaç testi hariç bütün testler METU-MEMS Araştırma Merkezinde yapılmıştır. Üretilmiş duyargalar arasında, yüksek performans için tasarlanan duyarga taraklı uygulaması ile 10 pF durağan kapasitans ile sadece 75 fF'lık bir kapasitans duyarlılığı gösterirken, içiçe geçmiş elektrotları kullanarak 8.1 pF durağan kapasitans ile 178 fF'lık bir kapasitans duyarlılığı göstermektedir.

Anahtar Kelimeler: Mikro Elektro Mekanik Sistemler (MEMS), Mikro işlenmiş İvmeölçer, Tam Diferansiyel Parmak Yapısı, Yalıtkan-Üstü-Silisyum (SOI) Pul.

*To my family,  
to the memory of my aunt Şakire AYDIN, and  
to my love Kıvılcım SÜMER...*

# ACKNOWLEDGEMENTS

First and foremost I want to thank my supervisor Prof. Dr. Tayfun AKIN for his generous support at my graduate studies and the development of this thesis. It is a great opportunity for me to work with him and being a part of his group at METU-MEMS Research Center.

Right after, I want to thank Dr. Said E. Alper for his guidance and didactic conversations, which helped a lot during this thesis work. His is one of the fine role models with his approach to the problems and systematic working style.

I want to specially thank to Orhan Ş. Akar for helping me to sharpen my process skills, being a model of a great process engineer, and also for his patience to my unending questions.

I would specially thank to IMU Group for their invaluable helps during my studies. Working with Serdar Tez, Dr. İlker E. Ocak, Akın Aydemir, Uğur Sönmez, M. Mert Torunbalci, Erdinç Tatar, Burak Eminoglu, Tunjar Askarli and Soner Sönmezoğlu side by side is a great opportunity for sharing their experiences and precious friendship during the development of this thesis.

I also would like to thank my colleges who put their flavor to my life and the ones who turned the clean room into an enjoyable work environment: Dr. Yusuf Tanrikulu, Dr. Özge Zorlu, Selçuk Keskin, Numan Eroğlu, Hatice Koydemir, Ufuk Şenveli, Başak Kebapçı, Şeniz E. Küçük, Özgecan Dervişoğlu, Kaan Demirel, Evrim Özçakır, Evren Erdil, Levent Beker, Deniz Eroğlu, Cavid Musayev, Dinçay Akçören, Alperen Toprak, Fırat Tankut, Zeynep S. Lüleç, Ceren Tüfekçi, Ilker Comart, Alper Küçükkömürler, Onur Yalçın, Korkut K. Tokgöz and staff of the METU-MEMS Research Center.

I am grateful to the memories that we shared in this small period of time and being a part of MEMS-VLSI Lab.

I also want to show my special thanks to Kıvılcım Sümer, who enriched my life with her beautiful presence and for her never ending support and love.

Finally and most importantly, I want to thank my parents Tülay and Mahmut AYDIN for their endless support throughout my life with their love and prayers, my brother Ekin AYDIN for the joys brightened my life, and to my aunt and grandma Şakire and Menşure AYDIN who raised me with great care and responsibility without stinting their affections.

# TABLE OF CONTENTS

ABSTRACT .....	iv
ÖZ .....	vi
ACKNOWLEDGEMENTS .....	ix
TABLE OF CONTENTS .....	xi
LIST OF FIGURES .....	xiv
LIST OF TABLES .....	xx
CHAPTERS	
1 INTRODUCTION .....	1
1.1 Application Areas of MEMS Accelerometers.....	4
1.2 Figure of Merits of the MEMS Accelerometer System .....	6
1.3 Classification of Accelerometers According to Sensing Schemes.....	8
1.4 Literature Review of Capacitive MEMS Accelerometers.....	11
1.4.1.1 Surface-Micromachined (SMM) Accelerometers .....	13
1.4.1.2 Bulk-Micromachined (BMM) Accelerometers .....	18
1.5 The Objective and Organization of Thesis.....	22
2 THE THEORY OF CAPACITIVE MEMS ACCELEROMETERS AND DESIGN OF THE FULLY-DIFFERENTIAL ACCELEROMETER WITH INTERDIGITATED FINGERS.....	25
2.1 Mechanical Design .....	26
2.1.1 Sensor as a System.....	27
2.1.1.1 Static (DC) Response of the System.....	29

2.1.1.2	Dynamic (Frequency) Response of the System .....	29
2.1.2	Mass Calculation .....	30
2.1.3	Spring Design and its Calculation.....	32
2.1.4	Damping Calculation .....	33
2.1.5	Electrostatic Spring Effect .....	34
2.2	Design of the Fully-Differential (FD) MEMS Capacitive Accelerometer ..	37
2.2.1	Differential Interfaces with Capacitive Sensing .....	37
2.2.2	Fully Differential Sense Electrodes Design .....	38
2.3	Fully-Differential MEMS Accelerometer's Design and Verification .....	45
2.3.1	1 <sup>st</sup> Generation Sensor .....	45
2.3.1.1	Modal Analysis of the 1 <sup>st</sup> Generation Sensor .....	47
2.3.1.2	Capacitance Analysis .....	48
2.3.2	2 <sup>nd</sup> Generation Sensor .....	51
2.3.2.1	Modal Analysis .....	53
2.3.2.2	Capacitance Analysis .....	54
2.4	Summary of the Chapter.....	55
3	FABRICATION OF THE FULLY-DIFFERENTIAL MEMS ACCELEROMETER WITH INTERDIGITATED FINGERS.....	56
3.1	Introduction to the MEMS Fabrication .....	57
3.2	Fully-Differential (FD) Accelerometer Process Overview .....	59
3.2.1	Glass Wafer Process.....	59
3.2.1.1	Anchor Formation.....	59
3.2.1.2	Pad Metal Formation .....	60
3.2.2	SOI Wafer Process .....	61
3.2.3	Anodic bonding of SOI and Glass Wafers.....	61
3.2.4	Following Anodic Bonding Process .....	63
3.2.4.1	Via Formation .....	64

3.2.4.2	Top Metal Formation .....	65
3.2.4.3	Pad Window Opening .....	65
3.2.4.4	Release of the Devices .....	67
3.2.5	Problems and Modifications .....	74
3.2.5.1	Frameless Wafer Process .....	75
3.2.5.2	Shorting the Pad Metallization Mask .....	77
3.3	Fabrication Results .....	79
3.4	Summary of the Chapter .....	84
4	TEST RESULTS AND DISCUSSIONS .....	85
4.1	Sensor Level Tests .....	86
4.1.1	1 <sup>st</sup> Generation Sensor Tests .....	87
4.1.2	2 <sup>nd</sup> Generation Sensor Tests .....	89
4.2	System Level Tests .....	91
4.2.1	The Glass Substrate .....	92
4.2.2	Static Measurements .....	94
4.2.3	Dynamic Measurements .....	95
4.3	Comparison of the Measurement Results .....	96
4.4	Summary of the Chapter .....	98
5	CONCLUSIONS AND FUTURE RESEARCH .....	99
5.1	FUTURE RESEARCH .....	100
	REFERENCES .....	102

# LIST OF FIGURES

## FIGURES

Figure 1.1: Change of MEMS sensors market size in years. ....	2
Figure 1.2: Prediction of MEMS market among the sensors in 2016. ....	2
Figure 1.3: Change of Inertial MEMS market size in terms of Million US Dollars from 2006 to 2012. ....	3
Figure 1.4: Fully-differential interface (a) with and (b) without on-chip reference capacitors. ....	13
Figure 1.5: The out-of-plane sensor (a) before the curl compensation, and (b) after the curl compensation. The serpentine springs have also effect in curl compensation. ....	15
Figure 1.6: Comparison of curl compensation in (a) H. Luo's in-plane and (b) H. Zang's out-of-plane sensors. ....	15
Figure 1.7: The closed up view of (a) (b) out-plane and (c) (d) in-plane sensors with their springs. ....	16
Figure 1.8: Torsional 3-axis CMOS-MEMS accelerometer. ....	17
Figure 1.9: (a) Device from top view and (b) fingers from a closer look. ....	19
Figure 1.10: The process flow of sensor in ten steps. ....	20
Figure 1.11: The SEM images of the fabricated 3-axis accelerometer's (a) (b) sense elements, (c) top view, and (d) springs. ....	20

Figure 1.12: (a) Definition of Si-vias by dry etch, (b) bonding of Si wafer to glass, (c) reflow of glass into the Si wafer, (d) lapping of glass, (e) contact metal patterning, (f) patterning, and (g) suspending of the device. ....	21
Figure 2.1: Accelerometer sensor model consist of a proof mass, springs, and damper.....	27
Figure 2.2: The amplitude response of the system changes with the quality factor values.....	28
Figure 2.3: MEMS accelerometer with its mechanical parts. ....	31
Figure 2.4: Doubly-folded beam is a serial sum of two guided beams in parallel.....	32
Figure 2.5: (a) Half-bridge configuration with single-ended output, (b) full-bridge configuration with the differential output including on-chip reference capacitors, and (c) full-bridge configuration with the differential output including sensor capacitances of the sensor in place of on-chip capacitances.....	38
Figure 2.6: Conventional bulk-micromachined comb finger array are composed of fingers attached to the fixed electrode and sense fingers attached to the proof mass.	39
Figure 2.7: CMOS-MEMS sensor's finger array composed of interdigitated fingers form compositions allowing differential sense of accelerations. ....	40
Figure 2.8: The anti-gap effect is more noticeable at low-g values, and its effect decreases at high g values. ....	41
Figure 2.9: One of the fixed fingers of the differential finger triplets make connections through the vias on BOX layer of the SOI wafer.....	42
Figure 2.10: The expected sensitivities of the sensor between 0 and 5 Volts by 1 Volt increments. The capacitance change is the deflection times the capacitance sensitivity at desired voltages. ....	46
Figure 2.11: 1 <sup>st</sup> generation sensor layout. The sensor includes five outputs to the readout.....	46

Figure 2.12: The solid model constructed for the modal simulation resonates at 3.6 kHz. The red colored parts in the model have the biggest deflection, while the anchors of the spring have zero deflection.....	48
Figure 2.13: The solid model of the interdigitated finger arrays with 3 $\mu\text{m}$ finger gaps. The highlighted fingers with orange are connected to each other from the top contact metallization. ....	49
Figure 2.14: The solid model of the interdigitated finger arrays with the anchor. ....	50
Figure 2.15: The expected sensitivities of the sensor between 0 and 1 Volts. The sensitivity can only be calculated for voltages below the pull-in voltage of the sensor, since the capacitance per pad will be higher due to decreased gap size. ....	52
Figure 2.16: The layout of the 2 <sup>nd</sup> generation sensor includes etch-holes on the surface of the proof mass that are detectable on the proof mass surface. In addition, the connections to the pads have routings in order to satisfy more equally distributed resistances different than the first generation design. ....	52
Figure 2.17: The solid model constructed for the modal simulation resonates at 2.2 kHz. The red parts of the model have the biggest deflection, while the anchors of the spring have zero deflection. ....	53
Figure 2.18: The solid model of the interdigitated finger arrays for the 2 <sup>nd</sup> generation sensor with 1.8 $\mu\text{m}$ finger gaps. ....	54
Figure 3.1: (a) Partially brown colored imperfect contacts have high resistances, (b) full brown colored contacts show the successful contacts with low resistances. ....	62
Figure 3.2: The schematic of the anodic bonding of SOI and glass wafers.....	62
Figure 3.3: General view of a wafer with removed handle layer by DRIE etching...	64
Figure 3.4: The pad routings' around has direct expose to O <sub>2</sub> plasma. The separations from the edges decrease as the routings go inside the sensor. ....	66
Figure 3.5: Substrate is a 450 $\mu\text{m}$ thick Borosilicate glass wafer.....	67
Figure 3.6: Formation of the anchors by HF etching. ....	68

Figure 3.7: Patterning the pad metallization by successive Au, Cr, and diffused Au etches.....	68
Figure 3.8: 35 $\mu\text{m}$ of thick Silicon device layer on top of the 2 $\mu\text{m}$ BOX layer with a supporting 450 $\mu\text{m}$ thick Silicon handle layer forms the SOI wafer. ....	69
Figure 3.9: Defining the structures by DRIE etching of the device Silicon layer. ....	69
Figure 3.10: Bonding of SOI and glass wafers. ....	70
Figure 3.11: Removal of the supporting handle Silicon layer by DRIE etching. ....	70
Figure 3.12: Formation of vias by RIE. ....	71
Figure 3.13: Patterning the deposited Cr/Au layer. ....	71
Figure 3.14: Reaching out the device Silicon layer by RIE etching of the topmost oxide layers. ....	72
Figure 3.15: Uncover of the pads by RIE etching of the device Silicon layer.....	72
Figure 3.16: Release of the devices by RIE etching of the BOX layer.....	73
Figure 3.17: General view of a fabricated 1 <sup>st</sup> generation FD accelerometer die.....	73
Figure 3.18: The compressive stress of the BOX layer results in bursting of the frame. ....	74
Figure 3.19: The accumulated charge on the isolated anchor regions is the reason of the spark discharge, which pierces through the BOX layer. ....	74
Figure 3.20: Burst out of silicon frame results in severe damage to the devices. ....	75
Figure 3.21: (a) Stress on the BOX layer buckles the Silicon frame, and (b) the frame is flattened after the BHF. ....	75
Figure 3.22: All of the stress accumulates at the ends of the springs, where they are attached to the sensor. ....	76
Figure 3.23: (a) Normal mask without short metals, and (b) mask with short metals allowing the distribution of accumulated charges equally around the wafer. ....	77

Figure 3.24: (a) The fluids leak into devices through the holes, and (b) damage the structure from inside. ....	78
Figure 3.25: (a) Normal mask without short metals, and (b) mask with short metals allowing the distribution of accumulated charges equally around the wafer. ....	78
Figure 3.26: The DRIE undercut results in widening of the gaps and shrinking of the widths of spring arms. ....	79
Figure 3.27: (a) The measured finger gap is 4.716 $\mu\text{m}$ , and (b) width of the spring arm is 5.531 $\mu\text{m}$ , which are smaller than the expected design values due to DRIE undercut. ....	80
Figure 3.28: The faults occurred during the fabrication are (a) PR masking of Si during the device layer etching, (b) stiction of fingers to each other due to polymer or PR residues, (c) deformations on contact areas, and (c) finger ruptures. ....	82
Figure 3.29: The top view taken from a fabricated fully-differential accelerometer die. The gaps are wider than the designed value, and edges of the top metal lines are detached due to final release. ....	83
Figure 4.1: The Agilent 4294A Impedance Analyzer, and probe station are used for the C-V curve measurements. ....	86
Figure 4.2: Test configuration of a FD accelerometer sensor. All of the pads are grounded excepted test pad. ....	87
Figure 4.3: The measured sensitivities from (a) the first electrode, (b) second electrode, (c) third electrode, and (d) fourth electrode at $\pm 5\text{ V}$ . ....	88
Figure 4.4: Measurement results are very close to the calculation results based on the post fabrication SEM measurements. ....	89
Figure 4.5: The measured sensitivities from (a) the first electrode, (b) second electrode, (c) third electrode, and (d) fourth electrode at $\pm 1\text{ V}$ . ....	90
Figure 4.6: Measurement results are very close to the calculation results based on the post fabrication SEM measurements. The calculations are made at voltages with 0.2V increments due to low pull-in voltage. ....	90

Figure 4.7: The accelerometer test setup is mounted on the centrifuge device. .... 91

Figure 4.8: 16-pin package used for housing the sensor and readout circuitry together..... 91

Figure 4.9: The layout of the single metal glass substrate with routings. .... 92

Figure 4.10: The 3D model is constructed for the capacitance simulations of the routings by CoventorWARE. .... 93

Figure 4.11: The Allan-variance plot of the noise data acquired by the static measurements. .... 94

Figure 4.12: The nonlinearity of the 1<sup>st</sup> generation sensor is found to be 21.4 kppm between  $\pm 4.9$  g operation-range with 10 pF integration capacitances. .... 95

Figure 4.13: The nonlinearity of the accelerometer calculated for the range  $\pm 4.9$  g results with a nonlinearity of 8.8 kppm..... 96

# LIST OF TABLES

## TABLES

Table 1.1: Existing capacitance topologies implement differential sensing along their sense axis.....	12
Table 2.1: The design parameters take place in determination of the performance of the fully-differential mechanical sensor element with interdigitated sense fingers. The parameters also include readout specific parameters, as duty cycle. ....	43
Table 2.2: The performance parameters are used to characterize the sensor and their equations using the above design parameters. ....	44
Table 2.3: Design and performance parameters of the 1 <sup>st</sup> generation sensors. ....	45
Table 2.4: The first three modes of the solid model. ....	47
Table 2.5: The capacitance matrix shows the total capacitance between the conductors. The conductors are the Proof Mass, and the fixed finger electrodes, Electrode-1 and Electrode-2.....	49
Table 2.6: The capacitance matrix shows the total capacitance of the anchored array. The conductors are the Proof Mass, and the fixed finger electrodes, Electrode-1 and Electrode-2. ....	50
Table 2.7: Design and performance parameters of the 2 <sup>nd</sup> generation sensors. ....	51
Table 2.8: The first three modes of the solid model. ....	53
Table 2.9: The capacitance matrix of the middle anchor. ....	54
Table 3.1: The comparison of the resistances is made using the two dies of the 2 <sup>nd</sup> generation sensor wafer.....	66

Table 3.2: Comparison of the performance parameters before and after the fabrication for the 1 <sup>st</sup> generation sensor. ....	80
Table 3.3: Comparison of the performance parameters before and after the fabrication for the 2 <sup>nd</sup> generation sensor. ....	81
Table 4.1: Simulation results show capacitances between the routings and the surrounding ground (GND) layer. ....	93
Table 4.2: Comparison of the measured performance parameters between 1 <sup>st</sup> generation sensors with the previous work. (*with 10pF C <sub>int</sub> , **with 1pF C <sub>int</sub> , ***calculated value).....	97

# CHAPTER 1

## INTRODUCTION

A lot has changed after the commercialization of metal film strain gauges that are assumed to be the pioneers of accelerometers. The first strain gauges measuring only vibration and shock were just bulk mechanical structures. Evolution of strain gauges reflects the development of sensor technology throughout the years. The development of the accelerometer and sensor technology sped up with introduction of integrated circuitry (IC) technology. The development of IC technology carried sensor technology to another dimension by introducing electronic control in mechanical devices. Together with the electronic control, electro-mechanical systems became more popular with their enhanced performance and started to find usage in mature automobile and avionic markets. While the IC dimensions were getting smaller, necessity of shrinking the mechanical component had arisen. Adaptation of IC fabrication techniques to Silicon enabled miniaturization of mechanical sensors into the sub-millimeter dimensions. Processing below sub-millimeter dimensions set light to realization of small electro-mechanical systems. Today these systems are named as Micro-Electro-Mechanical Systems (MEMS), which provide not only small dimensions but also low cost fabrication of large scale, low power consuming devices. Their small dimensions and increasing multipurpose usage opened new markets to emerging MEMS applications from biomedical to consumer electronics, and sensor technology still continues its development with increasing capabilities.

The capabilities of the MEMS technology is increasing as different kinds of MEMS based sensors introduce into the market where they cover a wide range of application areas with their unique functionalities. Among the MEMS sensors the place of inertial sensors, which are accelerometers and gyroscopes, cling upwards within time. Figure 1.1 shows predicted market of various MEMS sensors between 2010 and 2016. According to the expectations the applications related with accelerometers are going to cover a more broad area, in the market.

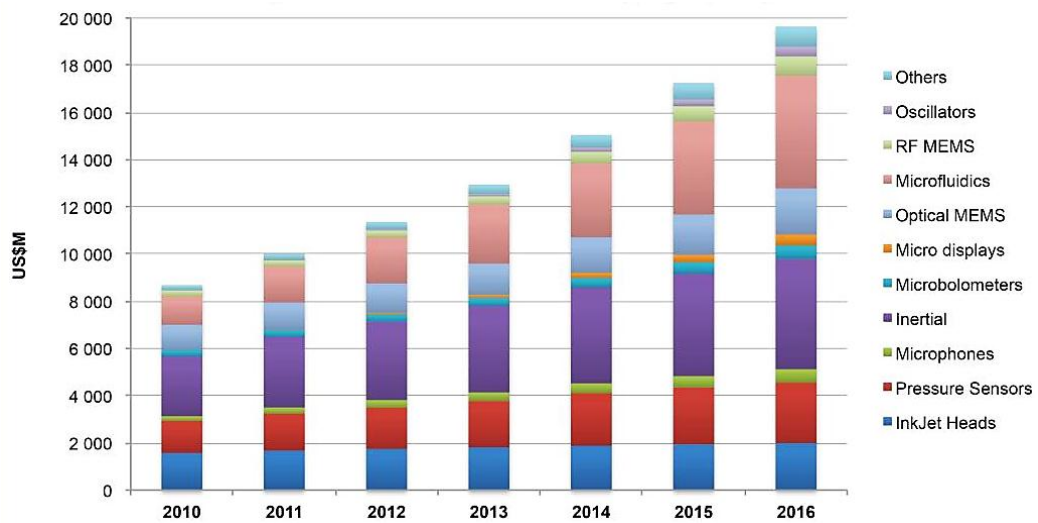


**Figure 1.1:** Change of MEMS sensors market size in years.

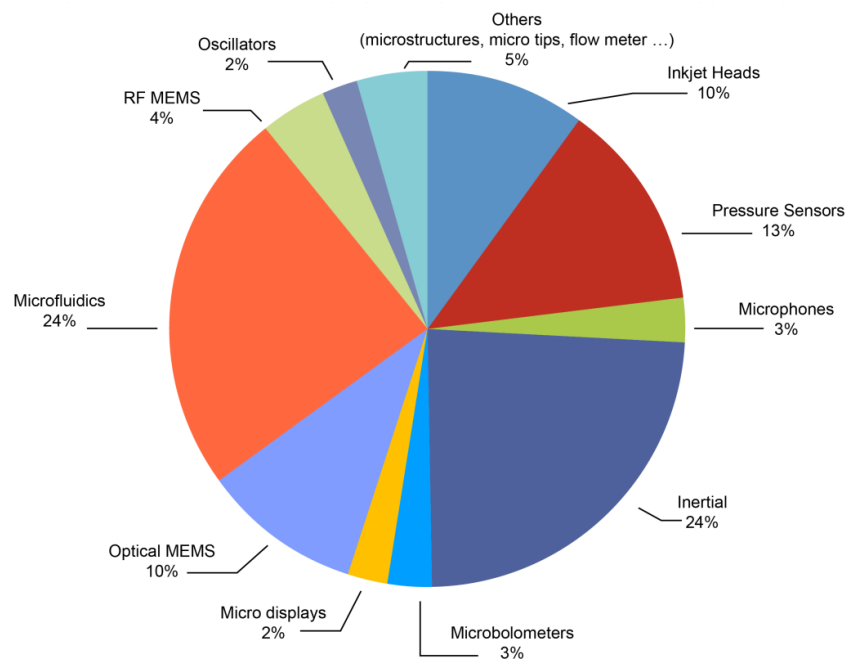


**Figure 1.2:** Prediction of MEMS market among the sensors in 2016.

The accelerometers gather in specific domains such as—automotive industry, consumer electronics, military & aerospace applications, industrial services, medical applications, and etc.—having a wide range of application spectrum. Among the aforementioned domains, the automotive business was the boosting factor in the increase of the investment on accelerometers with airbag, and electronic safety systems. Within time, consumer electronics started to take the lead with entertainment applications, especially in handheld devices, such as smart phones, gamepads, and computer peripherals, where cheap and small sized sensors are functional [2]. Figure 1.3 shows the change of Inertial MEMS Market from 2006 to 2012.

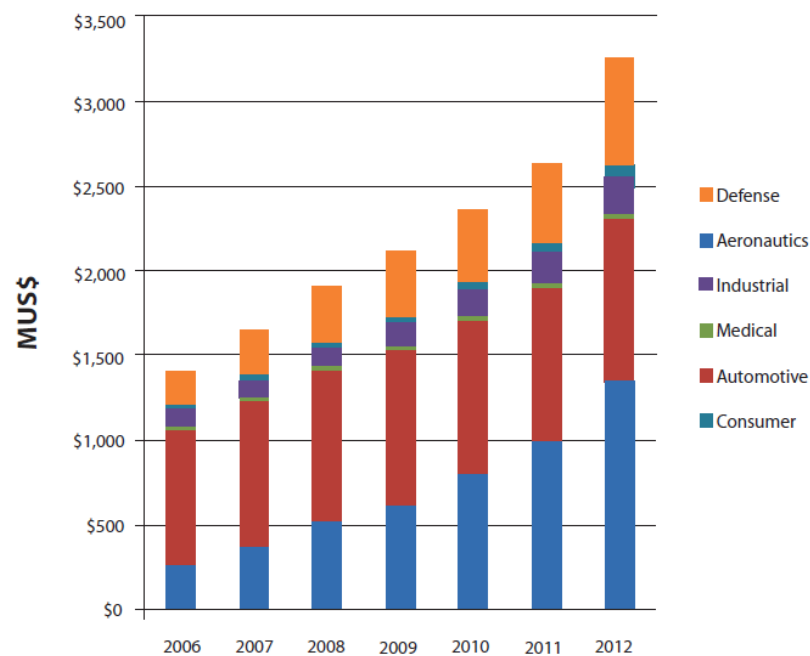


**Figure 1.3:** Change of Inertial MEMS market size in terms of Million US Dollars from 2006 to 2012.

In addition to above applications, accelerometers started to find usage with other sensors to increase the accuracy of the measured data, as well as to decrease the size and costs in various technologies [3]. For instance, combo sensors of accelerometers find usage in tire monitoring and Electronic Stability Control (ESC) systems in automobile technology. Tire monitoring systems include pressure sensors in assistance of accelerometers. The measured pressure changes with the position of the pressure sensor, during the rotation of the tire. In the tire, tilt sensors compensate

the measurement of pressure sensors which may have a varying data with the changing position [4]. In ESC systems, together with gyroscopes, the combo sensors decrease the size and costs in automobile production [5]. In sum, utilization of accelerometers with other MEMS sensors provides improvement in existing systems and opportunity for implementation of new applications.

As told above, the application of accelerometers varies greatly in several domains with a wide range of performance specifications. The following Section introduces the diversified amount of application areas of accelerometers under three main headings.

### **1.1 Application Areas of MEMS Accelerometers**

Today's micromachined sensors are replacing yesterday's bulky accelerometer equivalents in every application where small sized compact designs bring smart solutions. The solutions do not only answer conventional problems where bulky accelerometers do not fulfill the needs of the technology, but also flourish the new applications as in the automotive and consumer electronics. In the side line, high end defensive applications have already started to find appropriate accelerometer solutions in aerospace and navigation applications. To sum them all, today MEMS accelerometers are finding many area of usage in numerous applications. The applications are categorized into three main groups in terms of the measurement [7, 8]:

- Tilt sensing,
- Vibration monitoring,
- Inertial measurement

**Tilt Sensing:** Tilt sensing application of accelerometers find sufficient place in instrumentations and aerospace applications. All tilt applications depends on measuring static (DC) inputs. The sensors measure accelerations by taking the gravity of the earth as a reference. Therefore, a 2 g full scale output (FSO) with a sufficiently low bandwidth will be enough to sense the tilt for the best resolution. The tilt sensing application involves image stabilization of PDAs, camcorders, and

smart phones; platform stabilization of heavy vehicles, electronic compasses in Global Positioning Systems (GPS), patient beds, and industrial instruments. The type of the application defines the resolution of the system where high-end systems as GPS in satellites demand accuracy in  $\mu\text{g}$  resolutions, while surface instrumentations require mg resolutions.

**Vibration Monitoring:** Unlike the tilt sensors, vibration sensors sense dynamic inputs by monitoring transients and constant vibrations. Since the transient vibrations may occur at high frequencies, vibration and shock sensing sensors will need very large bandwidths in contrast to tilt sensors. Monitoring of seismic activities on structures such as bridges and dams, monitoring of vital activities of patients, and periodic vibrations on industrial instrumentation are exemplary to vibration sensor applications. Airbag and test applications in automotive domain, explosion monitoring in defense domain and constructions, and free-fall protection of hard disks' R/W heads for consumer electronics are most known examples to shock sensor applications that necessitate fast response times with very high g ranges about 100 g's to 100 kg's. Even though the accelerometers are used in vibration measurement, their most favored application is to measure the motion of a moving object or its position, which is possible with inertial measurement.

**Inertial Measurement:** The precise detection of the movement and position, which is possible by measuring the acceleration, is the core of many applications. Most of the critical commercial and defensive inertial applications include measurement of position and its stabilization. Tracking of animals and vehicles, navigation of ships and mobile unmanned vehicles, monitoring of patient and healthcare devices, and etc. are some examples to inertial applications. Among those, navigation and aerospace applications demand very tight specifications. In those applications, high resolution detection of the acceleration decreases the loss of information of the position. For instance, missile guidance requires strategic grade accelerometers having a bias drift of 1  $\mu\text{g}$  with a scale factor (SF) stability of 1 ppm [9]. In order to achieve such high performances, one has to satisfy minimum errors with high resolutions.

In the literature various type of accelerometers are reported to satisfy the best performances with different sensing approaches. Before going into detail of the sensing types, knowing the performance evaluation of accelerometers is a must which is named as the Figure of Merits.

## 1.2 Figure of Merits of the MEMS Accelerometer System

The miniaturization with the MEMS technology made it possible to use accelerometers from high technological missile defense systems to toys of children in every possible application. Application area defines the requirements of the accelerometer system. The system requirements greatly depend on performance parameters that are the scale factor, operation range, noise floor, bandwidth, resolution, and dynamic range, respectively.

**Scale factor:** The scale factor is the main performance parameter of a system. System takes acceleration input and gives output in terms of voltage, generally in mV. The components that comprise of the scale factor are stiffness, mass, and capacitive sensitivity regarding the mechanic sensor. More sensitive sensors have more capacitance sensitivities which is the change of the capacitance with respect to amount of the deflection that mechanic components experience. The deflection decreases with the stiffness and increases with the mass. Together, they contribute to the scale factor, which is a measure of the input acceleration in terms of voltage and defined as mV/g. Moreover, capacitance sensitivity contributes to the operation range.

**Operation range:** The range (also called as full scale output (FSO)) of an accelerometer is the maximum acceleration that the sensor is able to detect, and operation range changes depending on whether the operation of the system is open-loop or close-loop. In open-loop operation the range is proportional with the stiffness and the gap between sensitive elements, the fingers. In closed-loop operation the range increases with the capacitive sensitivity. However, the operation range is inversely proportional with mass in both cases. In addition, open and closed loop operation of the accelerometer changes the range. In closed-loop the range is linearly proportional with square of amplitude of the feedback pulse.

**Noise floor (Noise density):** Although, high operation ranges are favored, the sensitivity in downwards is important as well. The minimum detectable acceleration depends on the integrated noise of the accelerometer system in the desired bandwidth. Noise floor is the minimum measurable acceleration per unit bandwidth. The contributing noises to the floor are the mechanical noise (Brownian Noise) and electrical noises [10]. Mechanical noise with its common name Brownian Noise is the oscillation of the mechanical components with the surrounding air due to random drift of the particles, and the electrical noise is the sum of noises generated by the read-out circuitry. In open-loop operation of the read-out circuitry the front-end system noise contributes to the total electronic noise, and the Quantization noise is one of the critical sources among others in closed-loop operation.

**Bandwidth:** Bandwidth defines the maximum frequency limit of accelerations that can be detected. The limiting factor of the measurable band is the natural frequency of the mechanical sensor which depends on damping characteristics. In open-loop, the low pass filter at the output may also decrease the usable bandwidth. In contrast, closed-loop operation increases the bandwidth by increasing the sampling rate of the electronic filters. The maximum achievable bandwidth becomes half of the sampling rate with degradation of the resolution of the system.

**Resolution:** Resolution is the smallest detectable acceleration by the system within a defined bandwidth. As the bandwidth of the operation increases, the resolution decreases. Moreover, the A/D resolution is deterministic on the system resolution.

**Dynamic Range:** The overall performance of the accelerometer system depends on the ratio of FSO to resolution in terms of dB, which gives the dynamic range (DR). Although, system noise increases due to additional electronics and processes, DR increases with increased range in closed-loop operation.

Even though the above performance parameters define how accurately a system measures the applied acceleration, the precise measurement of accelerometers changes due to some error sources. The error sources are the nonlinearity, bias drift, and cross-axis sensitivity which affect the reliability of the accelerometer systems.

These sources may arise due to temperature changes, loadings on the mechanical sensor, or some other reasons, where they are listed below:

**Nonlinearity:** Nonlinearity is the maximum percentage deviation from a fitted curve of the scale factor over FSO of the accelerometer. The scale factor can vary during the operation range due to the hysteresis of the mechanical structure, and process related mismatches.

**Bias Drift:** It is deviation in voltage output without any acceleration. The reasons of the drift are temperature variations, the cyclic loadings on the springs of the sensor, and acceleration dependent behaviors.

**Off-axis sensitivity:** The sensors are sensitive to one axis and insensitive to others up to a percentage. The ratio of the output of the applied acceleration in off-axes to the output of the applied acceleration in sensitive axis in percentage defines the off-axis sensitivity. Process mismatches and alignment to the mounting case are factors that change the off-axis sensitivity.

Knowing the performance parameters with error sources will ease the evaluation of their applications in many occasions.

### **1.3 Classification of Accelerometers According to Sensing Schemes**

According to sensing methods of acceleration, accelerometers are classified as follow:

- Capacitive
- Resonant
- Tunneling current
- Optical
- Piezoresistive
- Piezoelectric
- Thermal

These sensors have various advantages over each other and some have specialized application areas. Among those application area, Capacitive MEMS accelerometers

find more place because of their moderate/high performance parameters. It is followed by Piezoresistive and Piezoelectric MEMS accelerometers. Resonant type accelerometers are also quite attractive for the market where aerospace applications take place. Tunneling, thermal, and optical devices have unique application areas for their specific properties. In addition, there are also examples to other approaches but not common as the above ones.

**Piezoelectric accelerometer (PEA)** is one of the first accelerometers utilizing ceramics (Lead Zirconate Titanate (PZT)) and single crystal materials (quartz, tourmaline) in order to measure the vibration and shock in place of strain gauges. The high modulus of the material allow flat frequency responses for the measurement of large frequency shocks and makes the device appropriate for high g accelerations. The stress due to acceleration induces a stress gradient on the material resulting in a charge build up, while under the applied electrical field the strain is produced on the material causing deformations [11]. The materials unique properties make the device appropriate for low power applications and resilient to temperature variations. However, the crucial drawback of the piezoelectric type accelerometers is the lack of their DC response, where the stored charge on the sensor leaks away under constant stresses [12].

**Piezoresistive accelerometers (PRA)** are alike PEAs in terms of transduction mechanism: the induced stress due to physical deformation of the structure results in a change in the resistance of the material. The materials that show Piezoresistive effects are metal strain gauges or ion implanted Silicon, which have relatively easier fabrication steps than other MEMS accelerometers. The placement of the material is made such that they form a Wheatstone bridge reflecting the change of the resistance of material at the output voltage [13]. The advantages of PRAs are their simple circuit integration and low cost production techniques. Generally, they are less prone to electromagnetic radiations than capacitive accelerometers [14]; however, suffer from temperature variations, where capacitive type accelerometers outperform them [10].

**Resonant type accelerometer (RTA)**, also called as vibrating beam accelerometer, have utilization in aerospace and space applications where high radiation and high

energy particles exist. The radiation in the upper atmosphere and space causes excess charge induction in electrostatically actuated MEMS sensors and cause failure of the devices [15]. The general working principle of those devices depend on the excitation of a shift in the frequency of the resonating structure by inducing extra stress to the device due to the applied acceleration [16]. With this transduction technique, RTAs differ from other displacement measuring accelerometers. The main advantages of RTAs are their high resolution and accuracy. Despite the main advantages, they have some drawbacks such as their complex circuitry, and aging due to continuous cyclic-loadings during operation [17].

**Tunneling current accelerometer** works according to the change of the current tunneling between two opposing conductive parallel plates due to their displacement. Since the conductive area is small, high sensitivities and resolutions are possible. Even sub-angstrom changes in the displacement are detectable due to the enormous change of the tunneling current due to accelerations [18, 19]. High resolution and sensitivity makes them find place in seismic and acoustic applications. However, they are susceptible to temperature variations.

**Optical accelerometers** operate in application areas where electrical accelerometers cannot be used. They are able to work in harsh/explosive environments such as in drill yards, active volcanic areas, and etc. by employing fiber optic cables. Optical cables carry the light to distances away without any danger to the operands. The main advantages of the optical accelerometers are their immunity to electromagnetic interface (EMI), temperature dependencies, and high sensitivities. However, they lack behind other accelerometers having different sensing methods because of their small sizes and fabrication simplicities.

**Thermal accelerometers** use the principle of thermal convection [20] and thermal microbeam techniques [21] to operate. In convection, generated hot bubbles in the middle of the sensor deflect while rising, and in turn, changes the heat of the thermal sensors (thermopiles, or thermocouples). For microbeam case, the thermal sensors, on a suspended beam, deflect under acceleration towards the heating resistors. In both case, the heat difference on the symmetrically placed thermal sensors gives the

amount of the acceleration. They can be produced monolithically at high volumes and low costs by utilizing CMOS technology. However, since the thermal sensors do not have a suspended proof mass as in other MEMS accelerometers, they are more durable to external shocks.

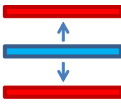
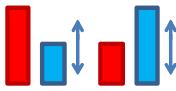
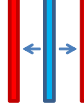
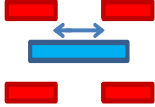
**Capacitive Accelerometers'** working principle depends on well-known parallel plate capacitance. In comparison with the above accelerometer types, they have good DC responses, prone to variations in temperature, are easy to fabricate in large scale, and generally have simplicity in designs. Moderate sensitivity of capacitive accelerometers suffices large bandwidths and low power operations. However, they are susceptible to EMI and space radiation [15]. But, with an appropriate packaging and shielding, capacitive accelerometers can pay their way into space applications. Therefore, capacitive sensors satisfy the most favored attributes of an accelerometer system.

The accelerometer sensor covered in this thesis is also a capacitive one, and concentrates on go beyond of the existing sensors in the literature. The following section reports the capacitive MEMS accelerometer in the literature by treating surface and bulk-micromachined accelerometer studies separately.

#### **1.4 Literature Review of Capacitive MEMS Accelerometers**

Parallel plate capacitance model lies beneath the working principle of capacitive accelerometers. Change of parallel plate's capacitance with respect to changes in gap and area give rise to capacitive topologies to detect acceleration. Mechanical springs that support these capacitive topologies allow sense of acceleration by letting their in-plane or out-of-plane movements. Movements of the accelerometer sensor result in injection of charges accumulated on sensors to read-out circuitry through the signal interface. Although, single and differential signal interfaces exist, differential reading schemes are preferred for the sensors to achieve a better accuracy by suppressing the common mode noise. Table 1.1 shows the existing topologies that the literature covers for differential sensing.

**Table 1.1:** Existing capacitance topologies implement differential sensing along their sense axis.

Topologies				
Direction	Out-of-plane	Out-of-plane	In-plane	In-plane
Variation	Varying gap	Varying area	Varying gap	Varying area

Differential sensing works in such a way that, under the acceleration two complementary capacitances of the sensor changes in an opposite manner, i.e., one of them increases as the other one decreases in a half-bridge configuration. With the capacitive half-bridge in the sensor, employing on-chip reference capacitors within the readout form a full-bridge configuration for sensing. The accumulated charges on sensor capacitances inject through the full-bridge configuration and electronics cancel-out common noises. Subtracting common noises from themselves increases the overall performance of the system by decreasing the noise floor. Therefore, a full-bridge configuration will predominate over the half-bridge configuration without reference capacitors.

However, the full-bridge configuration may corrupt the cancelation of common noises in the measured data unless the on-chip reference capacitors have enough resolution and offsets related mismatches do not exist. In order to make more accurate measurements, reference capacitors must be replaced with capacitors equal to that of the sensor. The low resolution related mismatch problem can be mitigated by dividing the sense capacitors of the sensor. Therefore, elimination of on-chip reference capacitors will allow shrinking the size of the readout; hence true fully-differential interface will be satisfied. Moreover, high power consumption in the front-end will be decreased. Figure 1.4 shows the fully-differential interfaces with and without on-chip reference capacitors.

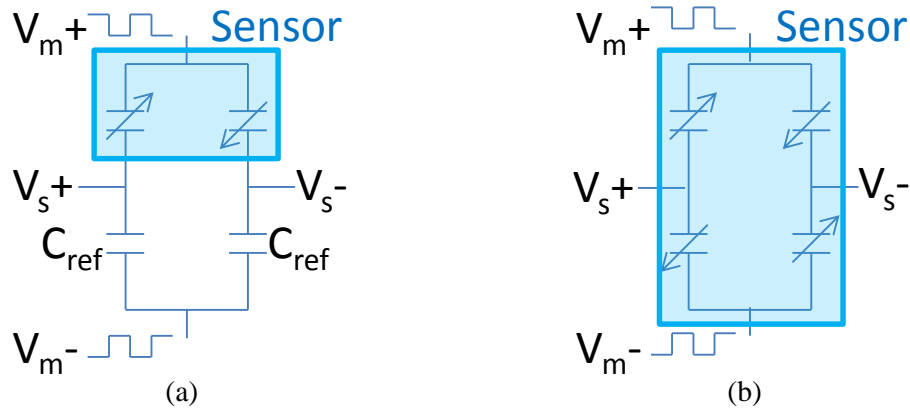


**Figure 1.4:** Fully-differential interface (a) with and (b) without on-chip reference capacitors.

Literature includes novel examples of the above topologies implemented with micromachining technologies. Micromachining technologies are gathered under two headings in terms of applicability: 1) Surface-Micromachining that is capable with monolithic fabrication, and 2) Bulk-Micromachining that is useful for fabrication of high aspect ratio devices. The different process techniques allow implementation of different finger structures used in sensing the acceleration. The multi metal-dielectric layers in CMOS-MEMS devices inherently provide fully-differential (FD) sensing employing interdigitated electrodes. However, in bulk-micromachining sensors' single crystal silicon (SCS) structure does not provide utilization of interdigitated sense electrodes. Thus, comb finger type electrodes are employed, which are less sensitivity than interdigitated ones. The FD accelerometers employing aforementioned electrodes are addressed below in surface and bulk-micromachining accelerometers.

#### 1.4.1.1 Surface-Micromachined (SMM) Accelerometers

The FD surface-micromachined accelerometers are initialized with post-CMOS process. The post-CMOS process is utilized in order to suspend the devices and reveal interdigitated sense electrodes. At the end, monolithic accelerometer is realized employing interdigitated sense electrodes, which provides high sensitivity within the limited die area. However, the fabricated accelerometers mainly suffer from buckling due to the stress gradients between the metal-dielectric interfaces. In 1999, G. Zang and G. Fedder proposed a solution to the existing problem with a curl-matching technique. The post-CMOS process included etching of Silicon with metal

mask layers to achieve a high aspect ratio device with structural curl compensation technique. The technique necessitates anchoring the proof mass and stator fingers together in the same axis in order to make the curl in line along with interdigitated fingers. However, due to the stress of the deposited layer stacks, the sensor still had a certain structural curve resulting in a 32% sensitivity loss from the expected value. The sensor achieved a sensitivity of 1.5 mV/g and a noise floor of  $0.5 \text{ mg}/\sqrt{\text{Hz}}$  with the implementation of curl compensation technique [22]. Subsequently, a year later, H. Xie and G. Fedder reported an out-of-plane accelerometer fabricated with the same process. Existing stress problem could not be solved with this new study, and the problem degraded the performance of the sensor resulting in a measurement range of  $\pm 27 \text{ g}$  with a noise floor of  $6.0 \text{ mg}/\sqrt{\text{Hz}}$ , while  $\pm 600 \text{ g}$  range and a noise floor of  $0.6 \text{ }\mu\text{g}/\sqrt{\text{Hz}}$  were expected, respectively. The achieved sensitivity was  $0.5 \text{ mV/g}$  [23].

In the same year, H. Luo and G. Fedder improved the performance of the out-of-plane accelerometer by adapting the previous [22] curl matching technique into the new design. In the new design, the stator fingers was anchored to the rigid frame that encapsulates the proof mass to decrease curl related sensitivity losses, which allows the finger electrodes curl in line. In addition to that, implemented force-feedback enhanced the performance of the device by increasing the operation range. The measured range of the device was larger than  $\pm 13 \text{ g}$  and the noise floor was  $1 \text{ mg}/\sqrt{\text{Hz}}$  [24]. Figure 1.5 shows the existing curl that significantly degrades the performance of the out-of-plane accelerometer in [22] and curl compensated sensor [24].

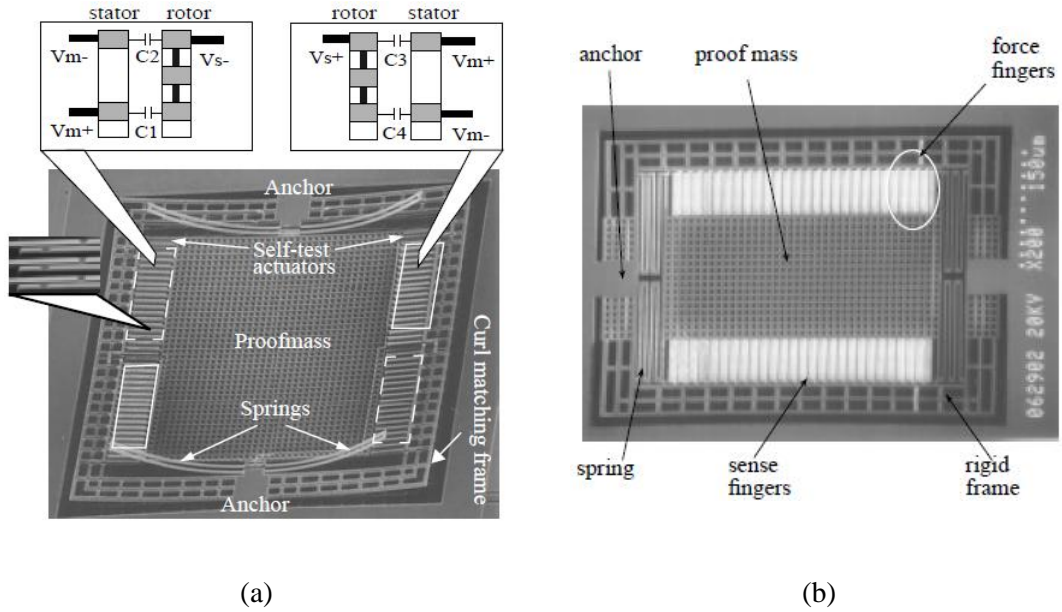


**Figure 1.5:** The out-of-plane sensor (a) before the curl compensation, and (b) after the curl compensation. The serpentine springs have also effect in curl compensation.

Figure 1.6 shows the compensation method in G. Zang’s sensor [22] with the compensation in that of H. Luo’s [24].

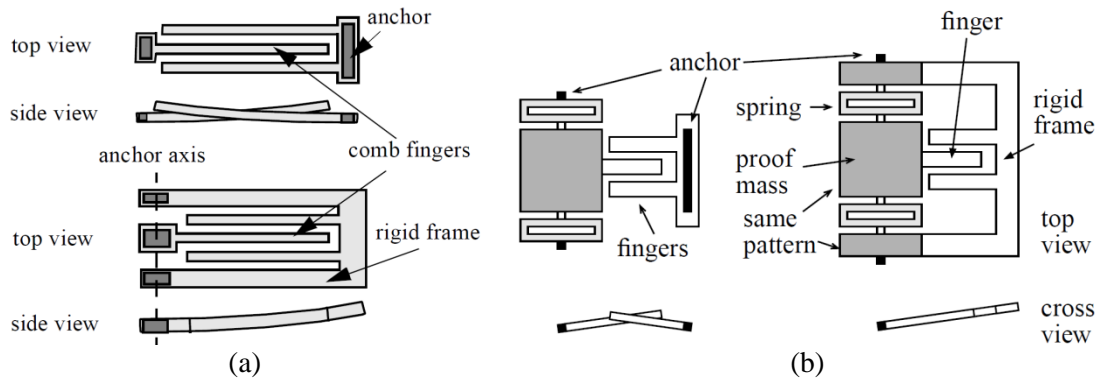


**Figure 1.6:** Comparison of curl compensation in (a) H. Luo’s in-plane and (b) H. Zang’s out-of-plane sensors.

In 2004, H. Qu and H. Xie demonstrated a 3-axis torsional accelerometer fabricated with post-CMOS process. The electrodes that surrounded the proof mass area sense in-plane accelerations, while the torsional structure that senses out-of-plane acceleration resides inside the proof mass. The imbalanced mass on both sides of the spring tilts around during the acceleration. However, the paper did not report any test results, except simulations [25]. In the same year J. Wu *et al.* reported an accelerometer implementing a continuous time voltage (CTV) sensing instead of

switch capacitors to decrease the noise. The measured noise floor was  $50 \mu\text{g}/\sqrt{\text{Hz}}$  by utilizing the CTV technique, which excludes noise folding and switching noise at the sensor interface. The accelerometer achieved a sensitivity of  $130 \text{ mV/g}$  in within a operation range of  $\pm 6 \text{ g}$  [26]. In comparison to that, in 2005, J. M. Tsai and G. Fedder were able to measure a noise of  $45 \mu\text{g}/\sqrt{\text{Hz}}$  with a CMOS-MEMS accelerometer. It's the first time that the measured noise is limited with the Brownian noise of the CMOS-MEMS sensor [27].

In 2007, C. Wang and M. H. Tsai reported a novel out-of-plane CMOS accelerometer. Timed post-CMOS wet etch of the metal lines defined the thickness of the sense electrodes. Sub-micron gaps of sense electrodes and high fill factor enhanced the sensitivity of the sensor. In addition, the sensitivity loss is compensated as in [24] by fixing the outer frame of the sensor. The sensor achieved  $1.14 \text{ mV/g}$  in sensitivity over a noise floor of  $0.05 \text{ mV}/\sqrt{\text{Hz}}$  [28]. Figure 1.7 shows the in-plane and out-of-plane sensors.

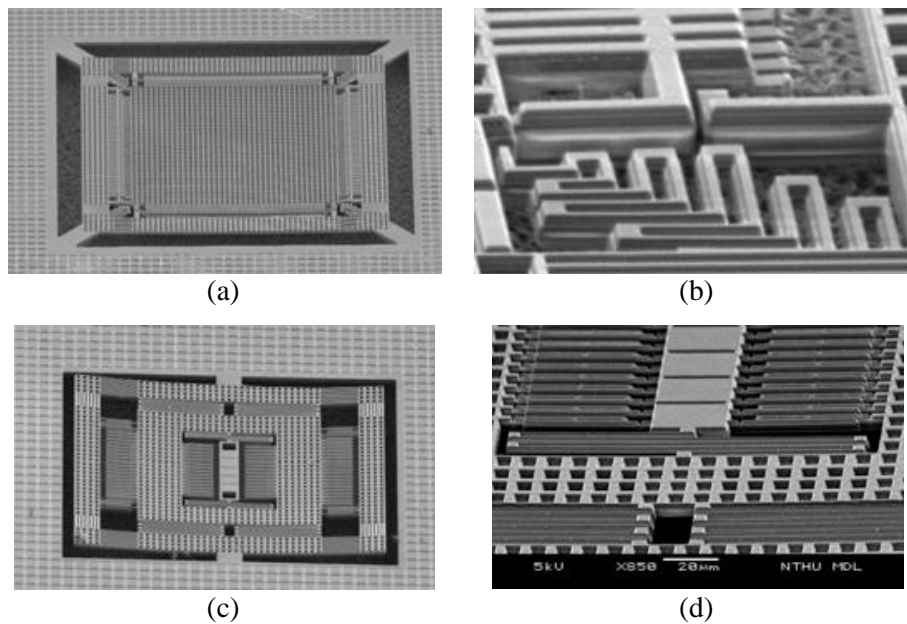


**Figure 1.7:** The closed up view of (a) (b) out-plane and (c) (d) in-plane sensors with their springs.

In 2008, H. Qu *et al.* improved the performance of the previously proposed [25] design. The accelerometer achieves sensitivity values of  $520 \text{ mV/g}$  and  $460 \text{ mV/g}$  in-plane axes, and  $320 \text{ mV/g}$  in out-of-plane axis, respectively. The measured noise

values were  $12 \mu\text{g}/\sqrt{\text{Hz}}$  in-plane axes and  $110 \mu\text{g}/\sqrt{\text{Hz}}$  in out-of-plane axis, respectively satisfying an operation range of  $\pm 50 \text{ g}$ . However, the temperature sensitivity of the sensor is a concern due to thermal coefficient difference of CMOS metals and dielectrics. The coefficient of temperature sensitivity is  $0.285\%/^{\circ}\text{C}$ , which is not close to bulk micromachined capacitive accelerometers [29].

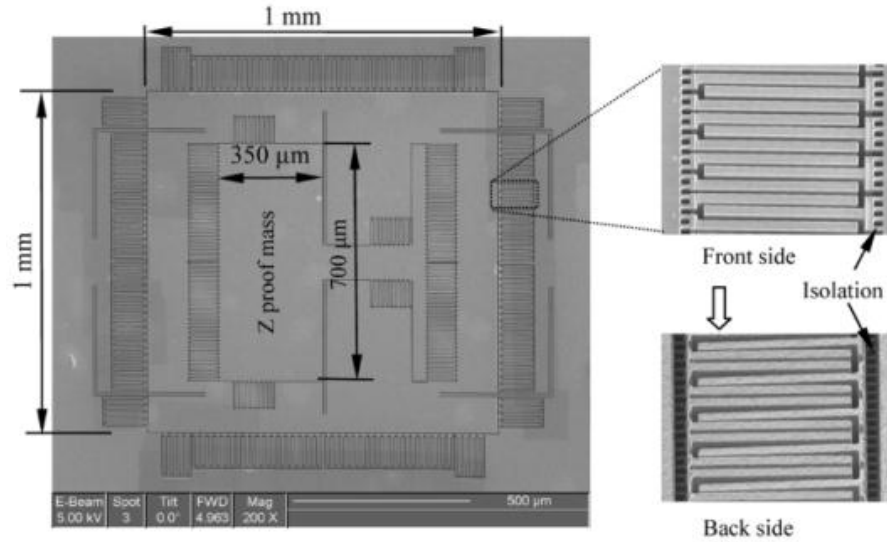


**Figure 1.8:** Torsional 3-axis CMOS-MEMS accelerometer.

In 2011, M. H. Tsai *et al.* achieved to fabricate a CMOS-MEMS sensor in a die area of  $400 \times 400 \mu\text{m}^2$ . The small sized sensor achieves  $14 \text{ mV/g}$  in-plane and  $8 \text{ mV/g}$  out-of-plane sensitivities; however, this sensor also suffers from the small mass as all of the surface-micromachined devices. It performs a noise floor of  $2 \text{ mg}/\sqrt{\text{Hz}}$  in-plane and  $3.4 \text{ mg}/\sqrt{\text{Hz}}$  out-of-plane, respectively [30].

Although the mentioned surface-micromachined sensors achieve sufficient sensitivities with interdigitated electrodes, they lack in mass. Therefore, the absence of mass results in domination of mechanical noise over the electronic noise. On the other hand, bulk-micromachined sensors do not suffer from mechanical noises. In next section, the advantages of bulk-micromachined sensor are given with the review of FD interfaced ones.

### 1.4.1.2 Bulk-Micromachined (BMM) Accelerometers

In contrast with surface-micromachined CMOS-MEMS accelerometers, bulk-micromachined devices offer smaller noises. SCS structure of bulk high aspect ratio devices allows a degree of freedom in sensor designs. Designs of high aspect ratio structures make high sensitivity sensors possible with small noise floors; however, SCS bulk material does not allow interdigitated sense elements, which require multi layered metals. Therefore, they generally implement comb-finger type electrodes as sense elements. Dividing the comb-finger arrays into sub-arrays is used in defining the capacitances in place of on-chip reference capacitors.

In 2004, B. V. Amini *et al.* introduced a bulk-micromachined SCS sensor having separated comb-finger electrodes. The sensor's proof mass was also fixed into a DC potential in order to get of switching noises. By setting the proof mass to a constant voltage, the switching related charge injection noises are significantly eliminated. The overall system achieved 450 mV/g in sensitivity over a range of  $\pm 2$  g with a resolution of 4.4  $\mu\text{g}$  at 150 Hz bandwidth [31]. In the same year, their group reported an accelerometer having 85 dB dynamic range with approximately the same sensitivity. A high aspect ratio device was processed with utilizing bulk-micromachining. However the resolution was smaller due to 110  $\mu\text{g}$  at 75 Hz [32]. After one year, B. V. Amili and F. Ayazi demonstrated a high performance bulk-micromachined FD sub- $\mu\text{g}$  accelerometer. The device has a thick 50  $\mu\text{m}$  of device layer in a SOI wafer to enhance the sensitivity by increasing the capacitive area. The sensor capacitances are split into four by electrically to form a full-bridge structure for FD sensing scheme as the previous ones [31, 32]. In this scheme, the measured capacitive sensitivity is 0.3 pF/g, equivalent to a scale factor of 750 mV/g and the resolution is measured as 11  $\mu\text{g}/\sqrt{\text{Hz}}$  at 2 Hz. The dynamic range increased to 102 dB with the increased sensitivity [33]. Figure 1.9 shows the fabricated FD sensor.

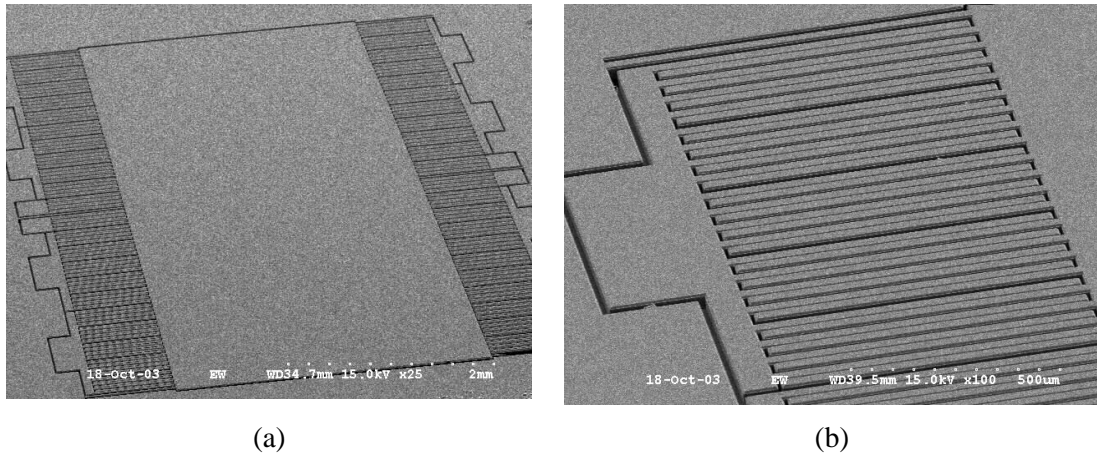


**Figure 1.9:** (a) Device from top view and (b) fingers from a closer look.

A year later, B. V. Amini *et al.* developed another accelerometer having an extra proof mass in comparison with his previous works. The extra mass of the unetched handle Si layer contributes to noise reduction resulting with a resolution of  $4 \mu\text{g}/\sqrt{\text{Hz}}$  and 2 to  $8 \mu\text{g}$  bias drift for 12 hours. However the demonstrated devices do not perform an interdigitated finger operation like post-CMOS processed accelerometers. Therefore, the symmetry does not exist in finger basis, which will enable more accurate measurements with cancelation of common noises [34].

In 2004, T. Tsuchiya *et al.* demonstrated a z-axis SOI accelerometer having differential sensing with vertical comb-electrodes with a new process method. The vertical comb-electrodes was realized on the device layer of the SOI wafer by two dry etch steps. The implemented dry etch steps ease the fabrication of the sense elements by getting rid of precise alignments in [35]. The measured capacitive sensitivity of the z-axis accelerometer was  $1.30 \text{ fF/g}$  [36]. In 2007, H. Hamaguchi *et al.* could implement FD sensing scheme by dividing vertical electrodes on the sensor. The sensor detects acceleration not only in z-axis but also in x- and y-axes having  $1.14 \text{ fF/g}$  and  $1.04 \text{ fF/g}$  capacitive senses, respectively [37]. Figures 1.10 and Figure 1.11 show the process flow and SEM images of the sensing elements, respectively.

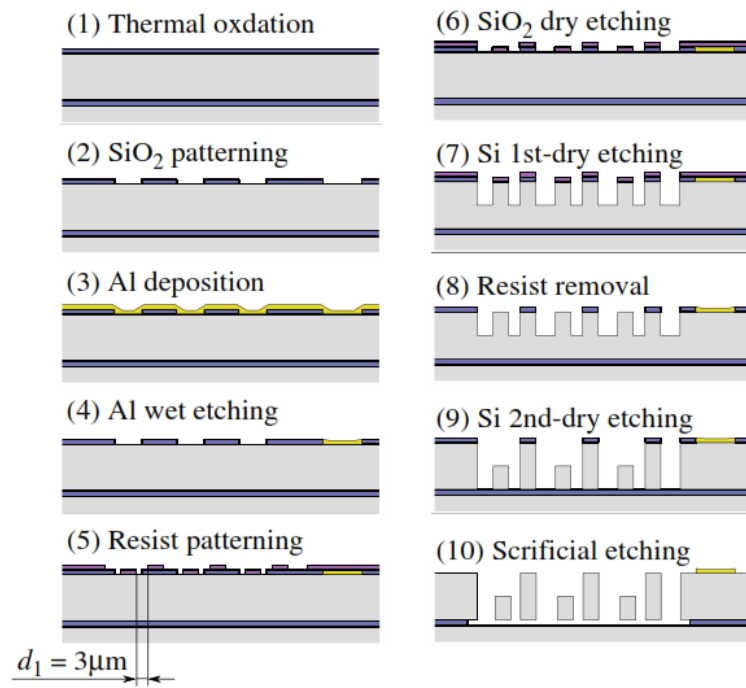


**Figure 1.10:** The process flow of sensor in ten steps.

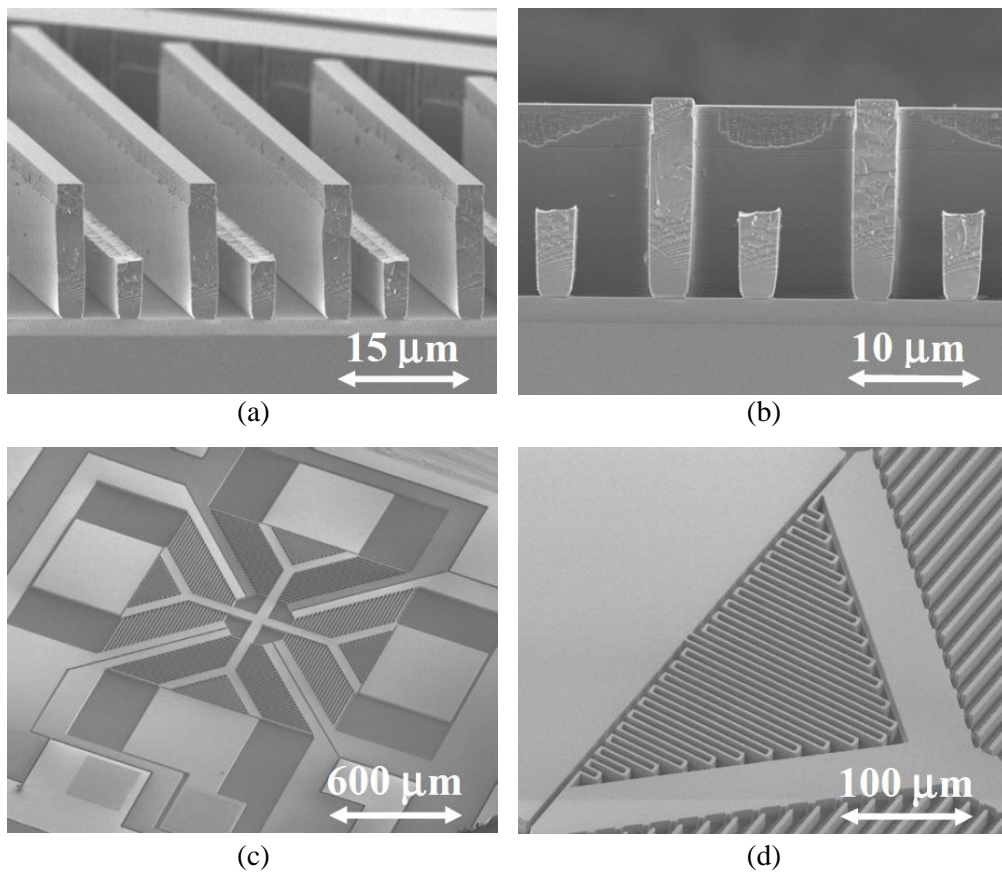


**Figure 1.11:** The SEM images of the fabricated 3-axis accelerometer's (a) (b) sense elements, (c) top view, and (d) springs.

Another interesting bulk micromachined capacitive accelerometer was demonstrated by Y. C. Hsu *et al.* in 2011. The accelerometer sensor was fabricated with a glass reflow process on an etched Silicon wafer employing interdigitated sense fingers, which was generally used in surface-micromachined devices. The glass was utilized as the proof mass, and it carries connections along the sensor using Si vias in order to form electrodes of interdigitated sense fingers. The sensor with the reflowed glass proof mass achieves a noise floor of  $5 \text{ ng}/\sqrt{\text{Hz}}$  with a scale factor of  $14.4 \text{ mV/g}$  [38]. However, the sensor's nonlinearity was 4.91%, and it has a resolution of 10 mg. Figure 1.12 shows the process flow of the sensor.

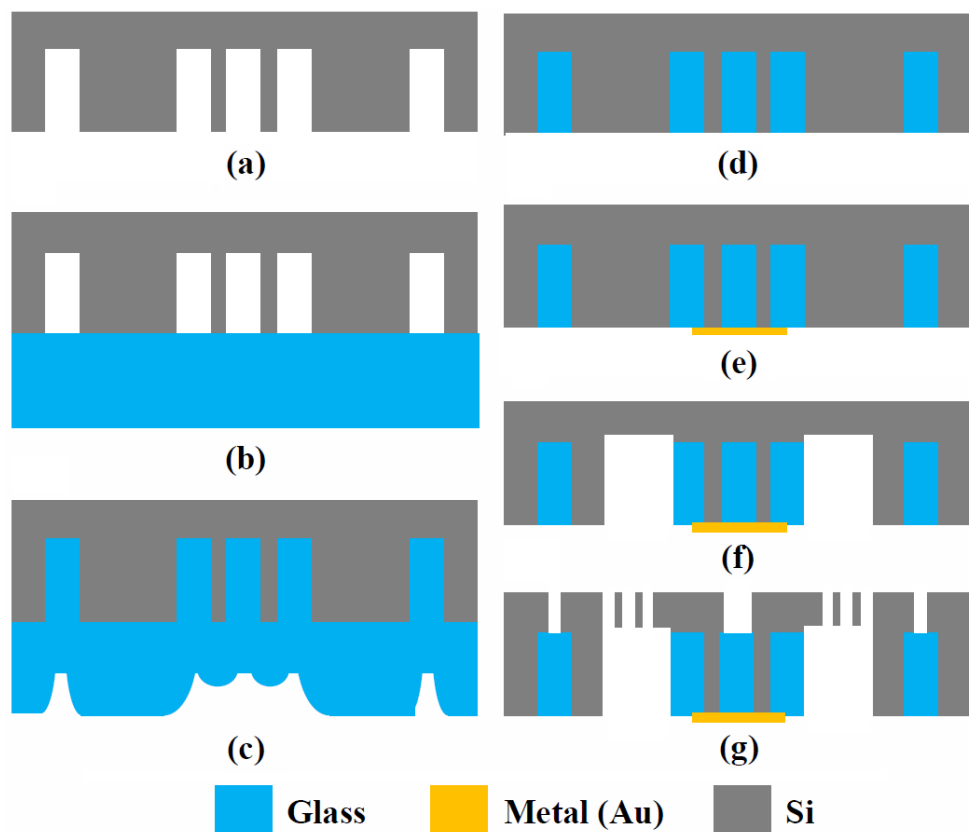


**Figure 1.12:** (a) Definition of Si-vias by dry etch, (b) bonding of Si wafer to glass, (c) reflow of glass into the Si wafer, (d) lapping of glass, (e) contact metal patterning, (f) patterning, and (g) suspending of the device.

The last example shows that the bulk-micromachined sensors are able to achieve sub- $\mu\text{g}$  noise floor. The bulk-micromachined sensors spoken of in the section also achieve high sensitivities due to high aspect ratios even comb-finger sense electrodes were employed.

## 1.5 The Objective and Organization of Thesis

CMOS-MEMS accelerometers provide monolithic fabrication of sensors with their read-out electronics. The monolithic fabrication utilizing the SMM technologies resulted in high volume production of small sized and low cost products, and eventually led to commercialization of MEMS accelerometers. The commercialization of MEMS accelerometers in automotive domain triggered more investments on the technology and commercial electronics became the leading domain in expansion of the accelerometer market [1]. However, high-end devices cannot still populate the market with existing production techniques. The situation addresses bulk micromachined devices having high-aspect ratio, low noise, and high sensitivity properties. Therefore in order to realize high-end accelerometers incorporation of bulk-micromachining techniques into the existing ones will be required. In addition, it means abandoning of monolithic production and adopting 3D integration, and various techniques [39] that allows the reduction of size for BMM sensors.

The aim of this thesis is to demonstrate a novel bulk micromachined MEMS accelerometer design in order to obtain high performance specifications by implementing a FD architecture employing interdigitated electrodes. The FD works having been fabricated with surface-micromachining techniques suffers from inherent buckling problems [22-25]. On the other hand, BMM sensors are able to implement comb-finger sense electrodes, which have smaller sensitivities than interdigitated ones due to SCS structure material. However, the absence of multi-layer metal routings in BMM accelerometers hinders the implementation of interdigitated sense fingers.

The work made for this purpose states a FD accelerometer without on-chip reference capacitors made out of interdigitated fingers using bulk-micromachining on SOI wafer for the first time in the literature. For this purpose, the fabrication takes advantage of the insulating buried oxide layer (BOX) of the Silicon-on-Insulator (SOI) wafer to utilize it as the support of the top metal layers. Therefore, a multi metal layered sensor structure as in CMOS-MEMS accelerometers can be fabricated on a SCS wafer.

This type of design can outperform multi metal layered post-CMOS processed MEMS accelerometers by excluding the internal stress originated buckling and related performance losses. Moreover, the interdigitated electrodes implemented in a bulk-micromachined sensor will provide higher sensitivities in comparison with its kind employing comb-finger sense electrodes.

The objectives of the thesis are as follows:

1. *Developing the process of bulk-micromachined MEMS FD capacitive accelerometer sensor on a SOI wafer employing interdigitated sense fingers.*

Two sensors are designed for the envisaged process: 1) One sensor design aims high yield fabrication with low noise operation, and 2) the other sensor aims high capacitance sensitivity operation.

2. *Modeling of the FD accelerometer system.*

The accelerometer system is simulated in MATLAB Simulink with the read-out electronics. Operational and stability analysis are made.

3. *Identification of the key problems of the fabrication and finding their solutions.*

The problems that have been met with during the fabrication: 1) Broken frame due to the stress of BOX layer in SOI wafer, and 2) charge accumulation during the bonding of SOI and glass wafers. The solutions of the problems are identified, and applied during the fabrication.

4. *Sensor and System level testing of the sensor with the readout electronics.*

Sensor level tests are made to extract C-V curve measurements and contact resistances. The system level tests are made in order to extract noise and bias drift with static measurements, and range and linearity from centrifuge test.

The thesis is comprised of five chapters. Chapter 1 gives an introduction about the MEMS accelerometer basics and types with their usage areas. Furthermore, novel FD surface and bulk-micromachined accelerometers in the literature are discussed. In this discussion, difference of comb and interdigitated sense electrodes was emphasized, briefly. A new FD high performance accelerometer sensor idea is proposed by incorporating the bulk-micromachining techniques allowing the realization of interdigitated sense electrodes employed in surface-micromachined accelerometers.

Chapter 2 covers the sensor mechanics and analyses static and dynamic responses. The design of FD architecture and its advantages are discussed.

Chapter 3 involves the fabrication of the FD accelerometer analyzed in the previous chapter. The process flow of the fabrication was given in detail. The problems encountered during the fabrication are explained with their solutions. Moreover, the chapter discusses fabrication results and their effects on the sensor's performance parameters.

Chapter 4 demonstrates the sensor and system level test results with the test environments and equipment used during the tests. The results of the tests are discussed based on the recalculated performance parameters after the fabrication.

Chapter 5 concludes the work carried out for the thesis. Discussions of the future works are made.

## **CHAPTER 2**

### **THE THEORY OF CAPACITIVE MEMS ACCELEROMETERS AND DESIGN OF THE FULLY-DIFFERENTIAL ACCELEROMETER WITH INTERDIGITATED FINGERS**

The detection of acceleration by capacitance depends on relative deflection of the movable plates. The deflection may result with an area or gap change in direction of acceleration. Movable mechanical components of the accelerometer sensor are its springs, proof mass, and fingers attached to the mass. In addition to those, the medium that the sensor operates in could be thought as one of the main mechanical components defining the sensor's performance parameters. The sensor consists of a number of fingers adjacent to the proof mass in a line (sense fingers). Together they hinge on the springs where they anchor the sensor to the fixed locations. The proof mass deflects along three axes; but more in the sense axis, where the spring constant along the sensitive axis is far smaller than in other axes. Deflection in sensitive axis may increase one side's capacitance of the sensor and decrease the other side's capacitance allowing a differential sensing. As a result of the capacitance change, the charges accumulate on the sensor inject through the interface to the readout.

In read out view, two ways of operation exist: 1) open-loop configuration, that measures the capacitance change, and 2) closed-loop configuration, that measures the capacitance change and sustains the nominal position of the sensor with force-feedback. The open loop architectures are simple, however have limited operation ranges with the gap size of the capacitive plate, and smaller bandwidths [1]. On the

other hand the closed-loop operation increases the range, linearity, and bandwidth; however, introduces noise into the system with increasing power due to the complexity of the electronics.

Since the main argument of this thesis is the mechanical sensor element and not the CMOS readout electronics, the following discussions concentrate on the sensor's mechanical parts and the fully-differential sensor design and verification.

Section 2.1 introduces the mechanical components of a sensor which are the proof mass, springs, and damping, and discusses their effects on static and dynamic responses.

Section 2.2 covers the fully-differential accelerometer concept in both surface and bulk-micromachined sensors, and how does it works in detail with the general sense elements in usage. Subsequently, the section gives the specifications of two sensor designs for the proposed sensor model in Chapter 1.

Section 2.3 shows the verification of the design with simulations of two different sensors named as 1<sup>st</sup> and 2<sup>nd</sup> generation. The 1<sup>st</sup> generation sensor is designed to increase a high yield fabrication with 3  $\mu\text{m}$  gap spacing, and also low noise with large proof mass. The 2<sup>nd</sup> generation sensor aims to achieve a high sensitivity in comparison with the previously fabricated sensor in METU-MEMS Research Center with Dissolved Epitaxial Wafer Process (DEWP) [12] with the new design remedying the deficiencies of the first generation.

Section 2.4 draws the summary of the chapter.

## **2.1 Mechanical Design**

In this section, mechanical parts of the accelerometer system, which are the proof mass, springs, and damping are handled separately. Before going into the detail of the sensor's mechanical components, an overview of the system is necessary.

### 2.1.1 Sensor as a System

The accelerometer is a second order spring-mass-damper system. The external acceleration loads the mechanical structure according to the Newton's 2<sup>nd</sup> law of inertia with a force causing the deflection of the mass in the opposite direction withstanding the damping and spring forces. Figure 2.1 shows the dependent parameters in a lumped element model of the accelerometer.

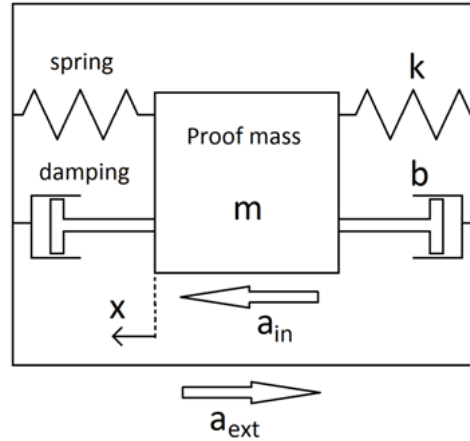


**Figure 2.1:** Accelerometer sensor model consist of a proof mass, springs, and damper.

The behavior of the above system equals to

$$-F_{ext}(t) = -m \cdot a_{ext}(t) = m \cdot \ddot{x}(t) + b \cdot \dot{x}(t) + k \cdot x(t) \quad (2.1)$$

where  $m$  is the proof mass,  $b$  is the damping coefficient acting on the proof mass to decrease its velocity, and  $k$  is the spring constant. With the division of  $m$ , the equation describing the system arrives to

$$a_{in}(t) = F_{ext}(t)/m = \ddot{x}(t) + b/m \cdot \dot{x}(t) + k/m \cdot x(t) \quad (2.2)$$

where  $a_{in}$  represents the acceleration that the sensor experiences. The equivalent of the experienced acceleration depends on the ratios that the Eq. 2.2. The  $s$ -domain transformation of the Eq. (2.2) gives the system's transfer function.

$$H(s) = \frac{X(s)}{A_{in}(s)} = \frac{1}{s^2 + b/m \cdot s + k/m} \quad (2.3)$$

From the Eq. 2.3 the extracted resonant frequency is:

$$w_n = \sqrt{\frac{k}{m}} \quad (2.4)$$

and the quality factor is:

$$Q = \sqrt{\frac{k \cdot m}{b^2}} \quad (2.5)$$

Then, the transfer function can be rewritten in terms of the quality factor and resonant frequency

$$H(s) = \frac{1}{s^2 + \frac{w_n}{Q} \cdot s + w_n^2} \quad (2.6)$$

where Q represents the quality factor, and  $w_n$  is the resonant frequency of the sensor. The quality factor determines whether the natural behavior of the system is underdamped ( $Q < 0.5$ ), critically damped ( $Q = 0.5$ ), or overdamped ( $Q > 0.5$ ). The sensors which work in atmospheric pressures generally show underdamped behavior, where sensors operating in vacuum show overdamped characteristics. The magnitude and phase responses of the system are directly related with those quantities. Figure 2.2 shows the magnitude response of the system with different quality factors.

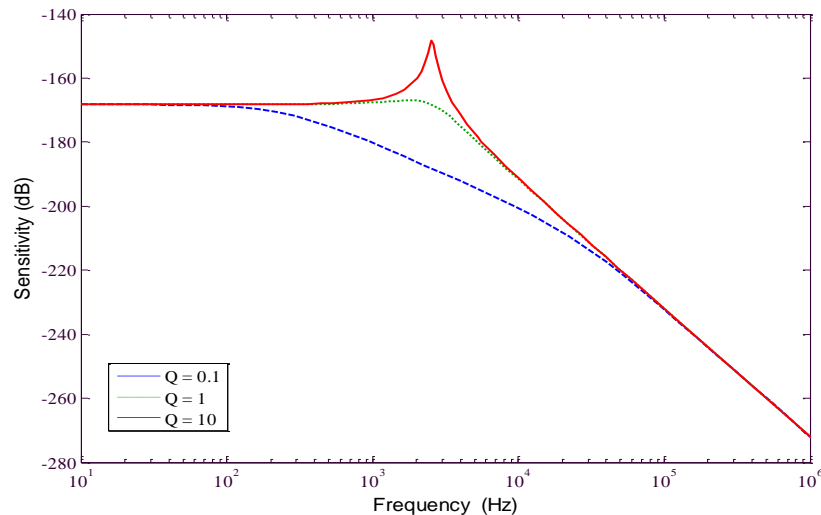


**Figure 2.2:** The amplitude response of the system changes with the quality factor values.

From the transfer function in Eq. 2.6, the deduced magnitude and phase functions are:

$$\frac{|X(j\omega)|}{|A_{in}(j\omega)|} = \frac{1}{\sqrt{(\omega_n^2 - \omega^2)^2 + \left(\frac{\omega_n}{Q}\omega\right)^2}} \quad (2.7)$$

$$\angle \frac{X(j\omega)}{A_{in}(j\omega)} = \tan^{-1}\left(\frac{\frac{\omega_n}{Q}\omega}{\omega_n^2 - \omega^2}\right) \quad (2.8)$$

### 2.1.1.1 Static (DC) Response of the System

Applied acceleration on the system makes the sensor accelerate due to the inertia. Under a static input the sensor will perform a DC response, where the ratio of the mass to the spring constant signifies the capacitance sensitivity of the sensor. Therefore, the scale factor increases with increasing mass and decreasing spring constant.

$$-F_{ext}(t) = -m \cdot a_{ext} = k \cdot x \quad (2.9)$$

$$\frac{x}{a_{ext}} = -\frac{m}{k} \quad (2.10)$$

### 2.1.1.2 Dynamic (Frequency) Response of the System

The dynamic response of the accelerometers can be deduced by introducing a sinusoidal input,  $A \sin(\omega t)$ , into the Eq. 2.1. Therefore, the response of the system will be a sinusoidal function with a magnitude of  $X$  and a lag of  $\theta$  in phase [40].

$$x(t) = X \sin(\omega t - \theta) \quad (2.11)$$

With introduction of Eq. 2.11 into expression, the Eq. 2.1 becomes

$$\ddot{x}(t) + 2\xi\omega_n\dot{x}(t) + \omega_n^2x(t) = \omega^2A \sin(\omega t) \quad (2.12)$$

where  $\xi$  is the damping ratio or in other words damping factor, which is directly proportional with the damping coefficient of the medium.

$$\xi = \frac{b}{2m\omega_n} \quad (2.13)$$

From Eq. 2.11 the magnitude and phase of the output response can be found easily.

$$|X/A| = \frac{\left(\frac{\omega}{\omega_n}\right)^2}{\sqrt{\left[1 - \frac{\omega^2}{\omega_n^2}\right]^2 + \left[2\xi \frac{\omega}{\omega_n}\right]^2}} \quad (2.14)$$

$$\angle X/A = \tan^{-1}\left(\frac{2\xi \frac{\omega}{\omega_n}}{1 - \frac{\omega^2}{\omega_n^2}}\right) \quad (2.15)$$

As  $\frac{\omega}{\omega_n}$ , in the denominator part in Eq. 2.14 goes to zero, the magnitude response approaches to  $\left(\frac{\omega}{\omega_n}\right)^2$ . The result depicts that the sensitivity is inversely proportional with the resonant frequency, where it is proportional with the ratio of the spring constant to the mass of the sensor.

### 2.1.2 Mass Calculation

The total mass has an effect on the overall performance of the system at first hand. The proof mass and attached finger arrays contribute to the total mass, which is inversely proportional with the mechanical noise and operation range. In order to increase the operation range, the total mass must decrease; on the other hand, in order to decrease the mechanical noise, which is a restrictive parameter of the resolution, the total mass needs to increase as in Eq. 2.11 and Eq. 2.12.

$$R = \frac{\partial C / \partial x}{m \cdot g} V^2 \quad (2.11)$$

$$a_n = \frac{1}{g} \sqrt{\frac{4k_b T b}{m^2}} (g / \sqrt{Hz}) \quad [41] \quad (2.12)$$

where R is the range,  $\partial C / \partial x$  is the capacitance sensitivity,  $a_n$  is the mechanical noise,  $k_b$  is the Boltzmann constant, T is the temperature in Kelvin, and b is the damping coefficient.

Up to now various techniques exist in the literature such as–glass reflow for forming the proof mass [38], gold deposition, where its density is eight fold of crystallized Silicon [42], saving the handle layer of the SOI wafer [34], perforation hole opening, and etc.– in order to alter the total mass. The glass reflowed accelerometers decrease the total mass of the proof mass, where the density of Silicon and glass are  $2230\text{kg/m}^3$  and  $2550\text{kg/m}^3$  respectively; and also for electrical isolation, while the metal electroplating takes place to fabricate the proof mass entirely from high density metals, or filling the etched holes on the proof mass. Generally, perforation holes are employed to decrease the damping in z-axis accelerometers; however, they could be employed to reach target operation ranges by changing the mass in restricted areas.

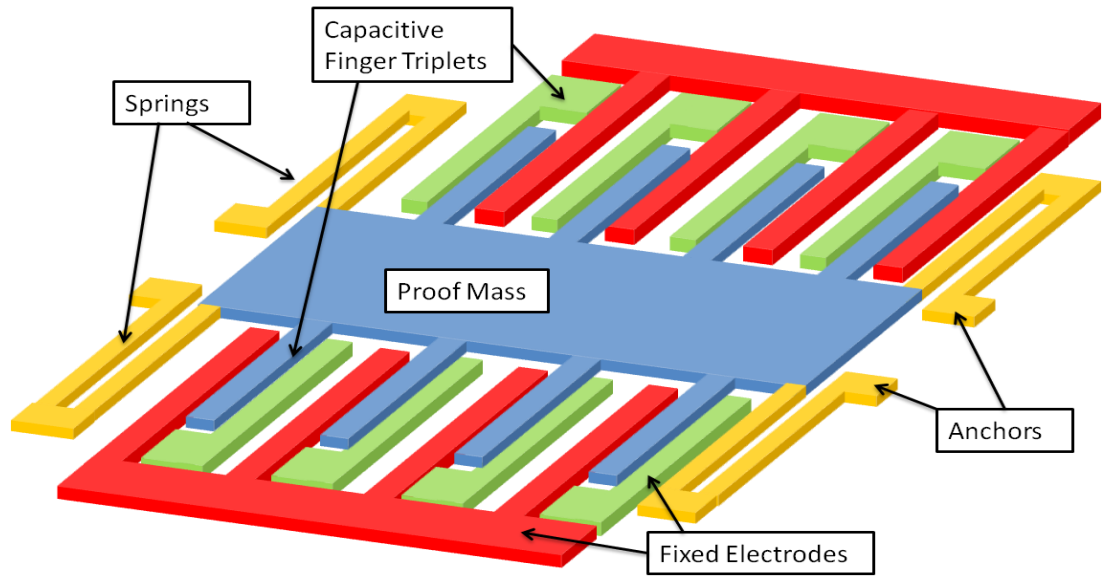


**Figure 2.3:** MEMS accelerometer with its mechanical parts.

The mass of an accelerometer can be calculated as

$$m_{\text{total}} = m_{\text{Proofmass}} + m_{\text{fingers}} - m_{\text{holes}} \quad (2.13)$$

$$m_{\text{total}} = h \cdot L_{\text{Proofmass}} \cdot W_{\text{Proofmass}} + N_{\text{total}} \cdot h \cdot l_{\text{finger}} \cdot w_{\text{finger}} - N_{\text{holes}} h \cdot \pi r^2 \quad (2.14)$$

where  $h$  is the thickness of the proof mass, fingers, and perforation holes.  $N_{\text{total}}$  is the number of sense fingers, whereas  $N_{\text{holes}}$  is the number of perforation holes. In the proposed design the perforation holes are neglected to increase the total mass for the mechanical noise reduction.

### 2.1.3 Spring Design and its Calculation

The structure that makes the sensor deflect along the sensitive axis is the spring. The springs have to be flexible in order to sense the movement of the proof mass in the sensitive axis, and prevent the movement in the cross axes. The stiffness of the spring depends on its geometry and the material. Generally the stiffness is known as the *spring constant*. As the spring constant increases the stiffness increases, therefore the sensor deflects less. Even the crystal structure of the material makes a difference in the spring constant as in the Young's modulus of Silicon. The Young's modulus of the (111) Silicon which is 185 GPa has a higher Young's modulus value than (100) Silicon which is 130 GPa. Since Silicon springs will be subjected to many cyclic loadings in the field of application, a robust design is necessary. Thus, the spring design needs a special attention while taking into account structural and material properties.

The type of the spring employed in this work is called as *doubly-folded beam*, which has an equal spring constant of a single guided beam. The design is first used in [12] and modeled as the parallel sum of the two folded guided beams. Figure 2.4 shows doubly-folded beam structure used in the fully-differential sensor design.

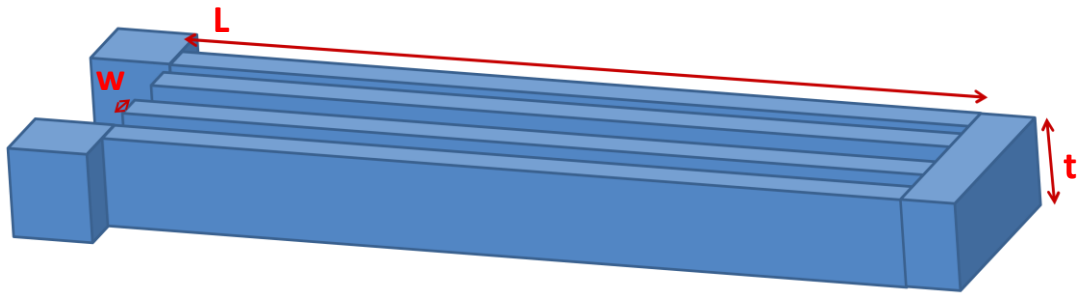


**Figure 2.4:** Doubly-folded beam is a serial sum of two guided beams in parallel.

The equivalent spring constant of the sensor is equal to the spring constant of a single guided cantilever beam with length,  $L$  as in Eq. 2.15.

$$k_{beam} = \frac{E \cdot w \cdot t^3}{L^3} \quad (2.15)$$

Even though the area of the springs is increased, the rigidity of the truss is maintained with a better stress relieving design. Furthermore, the proposed design is more immune to the process mismatches due to increased spring arms.

#### **2.1.4 Damping Calculation**

Damping is a dissipation mechanism of the energy built up in the sensor due to the external acceleration. Various damping mechanisms such as–viscous air damping, thermo-elastic damping [43], support losses [44], surface losses, and losses due to the air flow [45], and etc.–are reported in the literature. Losses due to thermo-elastic deflections and the mechanical structure are important for devices working in vacuum environments with high Q-factors. The predominant one among these mechanisms is the viscous air damping for devices working in underdamped environments as in-plane MEMS capacitive accelerometers. As the accelerometer deflects through the sense axis, two flow mechanisms contribute to the damping: 1) the Couette flow damping, which generates from sidewise slide of two opposing films, and 2) the Squeeze film damping, which generates from closing of parallel films onto each other.

In the mechanical sensor element, the squeeze film damping results from compression of thin air films between the capacitive plates due to the deflection of the proof mass. As the movable plates deflect towards the fixed ones, the thin air films squeeze between plates and viscously flow out.

On the other hand, the Couette flow damping comes along with the deflection of the proof mass contrary to the glass substrate. The friction between the bottom surface and air film opposes the movement, as the proof mass deflects. Additionally, the absence of perforation holes increases the weight of the Couette flow in overall damping factor formula.

The Couette flow damping coefficient can be calculated as below if the gas molecules are assumed to have Newtonian behavior [46]:

$$b_{\text{Couette}} = \mu_{\text{air}} p_{\text{air}} \frac{A_{pm}}{d} \quad (2.16)$$

where  $\mu_{\text{air}} = 3.7 \times 10^{-4} \frac{\text{Kg}}{\text{m}^2 \cdot \text{sec} \cdot \text{Torr}}$  is the viscosity constant of the air,  $p_{\text{air}}$  is the air pressure,  $A_{pm}$  is the bottom surface area of the proof mass, and  $d$  is the elevation of the proof mass from the substrate. According to [46], the squeeze film damping coefficient is calculated as:

$$b_{\text{Squeeze}} = \mu_{\text{air}} p_{\text{air}} \frac{7L \cdot w^3}{d^3} \quad (2.17)$$

where  $L$  is the parallel plates' overlap length, and  $w$  is the width of the plates.

The total damping factor then can be written as the sum of the Couette flow and Squeeze film damping coefficients. The Squeeze film damping coefficient is multiplied by  $N$ , if  $N$  number of sense elements exist in the sensor area.

$$b = b_{\text{Couette}} + b_{\text{Squeeze}} \quad (2.18)$$

$$b = \mu_{\text{air}} p_{\text{air}} \frac{A}{d} + N \cdot \mu_{\text{air}} p_{\text{air}} \frac{7L_f \cdot w_f^3}{d^3} \quad (2.19)$$

Damping affects two important components of the system: 1) the mechanical noise, and more importantly 2) the quality factor in Equation 2.5. The mechanical noise is proportional to the square root of the damping factor; however, the quality factor is inversely proportional to it, as Eq. 2.5 and Eq. 2.12 denote. The quality factor directly affects the system's behavior and changes its dynamic response.

### 2.1.5 Electrostatic Spring Effect

In addition to the mechanical spring forces, there are electrostatic spring forces affecting the response of the sensor. Mechanical springs have a positive spring effect stabilizing the sensor into its nominal position; however, electrostatic forces destabilize the sensor, hence act as a negative spring. This behavior is named as the electrostatic spring effect or electrostatic spring softening.

Equation 2.20 and Equation 2.21 show the effect of electrostatic spring forces, where they alter the resonant frequency of the sensor from its designed value.

$$k_{tot} = k_m - k_e \quad (2.20)$$

$$f_0 = \frac{1}{2\pi} \sqrt{\frac{k_{tot}}{m}} \quad (2.21)$$

More importantly, the electrostatic springs affect the capacitive sensitivity of the sensor. Increased electrostatic spring constant introduces instability to the system. When the electrostatic spring constant exceeds the mechanical spring constant, the sensor attracts and collides with one of the parallel plates, which is called as “snap-in”. The critical voltage before the snap-in is known as the “pull-in voltage”, where the electrostatic spring constant catches up with the mechanical spring constant. The experienced electrostatic force then can be written in terms of the capacitance sensitivity:

$$F_e = \frac{1}{2} \frac{\partial C}{\partial x} V^2 \quad (2.22)$$

The resulting electrostatic spring constant is equal to electrostatic force’s derivative.

$$k_e = \frac{\partial F_e}{\partial x} = \frac{1}{2} \frac{\partial^2 C}{\partial x^2} V^2 \quad (2.23)$$

The derivation of the deflection starts with writing down the forces acting on the system at the steady state condition.

$$F = \frac{1}{2} \frac{\partial C}{\partial x} V^2 - k_m x = \frac{1}{2} N \epsilon_0 \frac{A}{(d-x)^2} V^2 - k_m x \quad (2.24)$$

At equilibrium, the electrostatic force and spring force are equal to each other. In the designed sensor N has to be multiplied by two because of the separated electrodes in fully-differential sensor without on-chip reference capacitors.

$$F_{eq} = 0 \rightarrow k_m x = \frac{1}{2} N \epsilon_0 \frac{A}{(d-x)^2} V^2 \quad (2.25)$$

The derivative of the force acting on the system gives the stiffness at the equilibrium.

$$\frac{\partial F_{eq}}{\partial x} = N\epsilon_0 \frac{A}{(d-x)^3} V^2 - k_m \quad (2.26)$$

The critical point is, therefore, acquired by substituting Eq. 2.25 into Eq. 2.26, and setting the equation to zero.

$$\frac{2k_mx}{d-x} = k_m, \quad (2.27)$$

$$x = \frac{d}{3} \quad (2.28)$$

The pull-in voltage level can be easily derived by substituting the deflection value at the critical point in Eq. 2.28 into Eq. 2.25.

$$V_{pull-in} = \sqrt{\frac{8k_md^3}{27N\epsilon_0A}} \quad (2.29)$$

The pull-in voltage found in Eq. 2.29 is the maximum voltage that can be applied during the sensor level tests of the fabricated accelerometer sensors from one pad. The same equation can be taken into account in order to find the pull-in voltage during the snap-free operation of the system. It is calculated by incorporating other electrodes into the consideration utilizing the Eq. 2.26 when deflection in closed-loop is zero. Therefore, the voltage during the operation is extracted as in below:

$$V_{pull-in} = \sqrt{\frac{k_md^3}{4N\epsilon_0A}} \quad (2.30)$$

Note that the voltage dependency of the electrostatic spring constant restricts the amount of the voltage that can be fed into the sensor without the force feedback option. Despite that, the maximum voltage can be increased beyond pull-in voltage with introduction of the force feedback in the close-loop operation.

## 2.2 Design of the Fully-Differential (FD) MEMS Capacitive Accelerometer

Among the sensing schemes, the electrostatic transduction is the most favored conversation mechanism of the acceleration to electrical signals. The generated signals are generated due to the injected charges from the capacitive sensing elements of the sensor. The main advantages of implementing the capacitive sensing elements are their low power consumption, ease of fabrication, and the integration with electronics. Successful integration of the sensor to the read-out necessitates low noise capacitive interfaces. The low noise is only possible with differential interfaces.

The Section 2.2.1 introduces existing differential interface schemes, concentrating mainly on the FD one. Then, the realization of the fully-differential sensing takes place in the subsequent Section 2.2.2 in discussion with the fabrication utilizing bulk-micromachining.

### 2.2.1 Differential Interfaces with Capacitive Sensing

A capacitor stores energy between two conductive surfaces separated by a dielectric medium. Its capacitance, which is a measure of charge that can be stored, depends on the gap, the intersection area, and the potential difference of the conductors.

$$Q = C \cdot V = \frac{\epsilon_0 \cdot A}{d} V \quad (2.31)$$

The stored charge on the parallel plates varies with the capacitance change due to the acceleration. As movable plates deflect under the acceleration, gaps on one side of the sense element reduce, while gaps on the other side increase allowing a differential sensing of the acceleration. The differential sensing schemes includes three types of architectures. Figure 2.5 illustrates those architectures that are common in the literature:

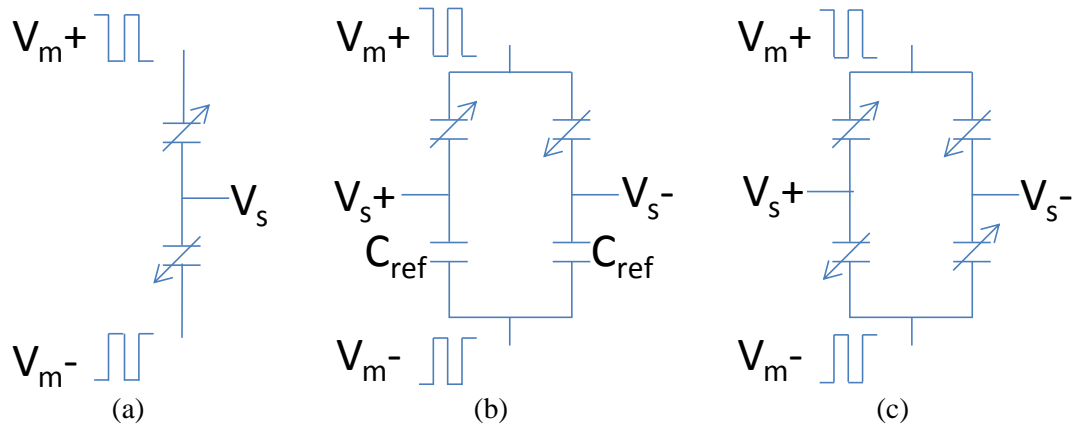


**Figure 2.5:** (a) Half-bridge configuration with single-ended output, (b) full-bridge configuration with the differential output including on-chip reference capacitors, and (c) full-bridge configuration with the differential output including sensor capacitances of the sensor in place of on-chip capacitances.

The linearity in sensitivity increases from left to right in the figure. The (a) cancels common noises at the modulating signals, but process mismatches result in some noise at the common node. Therefore, it is possible to witness better input common noise rejection ratios at the sensor interface. However, high resolution of on-chip capacitances requires more die area of the chip. The (c) is the most robust architecture for linear sensing as the on-chip reference capacitors are expelled from the read-out. The configuration is easily applicable in post-CMOS processed MEMS accelerometers [22-24]. Also similar techniques implemented for full-bridge architectures draw the attention in bulk-micromachined accelerometers by precluding the switching of the proof mass in (c) which results with injection of noises [31-34].

The proposed bulk-micromachined sensor in this thesis provides differential sensing with full-bridge sensing architecture. The following Section 2.2.2 describes how the architecture is implemented in bulk micromachining with interdigitated electrodes.

## 2.2.2 Fully Differential Sense Electrodes Design

The design and comprehension of the advantages of the fully-differential electrodes requires the understanding of comb type finger electrode arrays that find usage in bulk-micromachined sensors and implementation of interdigitated electrodes in CMOS-MEMS accelerometers. The comb fingers consist of parallel plate arrays that extensively take place in accelerometer implementations [12, 31-34]. The movable

part of the comb finger pairs is the sense finger, and the corresponding fixed one of the pair is the fixed finger. Relative motion of the sense fingers to the fixed ones results in the change of capacitance, which is known as the capacitance sensitivity. The total sensitivity is the sum of positive and negative changes in the capacitance of the finger pairs placed in a line. For the maximum sensitivity, the gap between the sense finger and the corresponding fixed finger of the pair must be as smaller than the anti-gap as possible. Figure 2.6 illustrates the gap and anti-gap concept of the existing comb fingers with belonging capacitances.

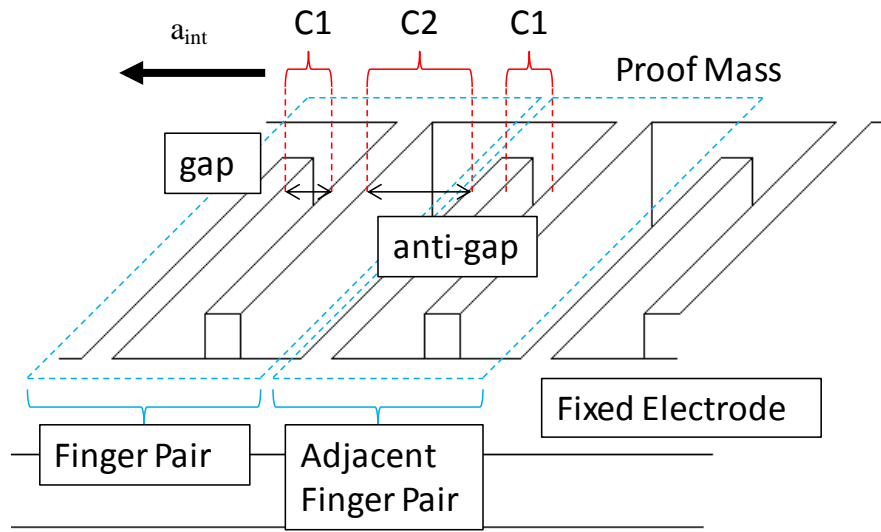


**Figure 2.6:** Conventional bulk-micromachined comb finger array are composed of fingers attached to the fixed electrode and sense fingers attached to the proof mass.

In this configuration, every individual sense finger of the proof mass is drawn away from the one of the neighboring fixed fingers, and gets closer to the its complementary fixed finger under acceleration. Therefore, the total capacitance sensitivity in one pair is the sum of the increasing capacitance  $C_1$  with respect to the decrease on the gap, and the decreasing capacitance  $C_2$  with respect to the increase on the anti-gap. The total capacitance is equal to their sum multiplied by the number of finger pairs.

$$C_{total} = C_1 + C_2 \quad (2.32)$$

$$C_{total} = N_{pair} \cdot \epsilon_0 \cdot h \cdot L_{overlap} \left( \frac{1}{d_1 - x} + \frac{1}{d_2 + x} \right) \quad (2.33)$$

where  $N_{pair}$  is the number of finger pairs,  $\epsilon_0$  is the permittivity of air,  $h$  is the thickness,  $L_{overlap}$  is the overlap length of fingers,  $d_1$  and  $d_2$  are the gap and anti-gap distance, and  $x$  is the deflection. The capacitance sensitivity is the change of the total capacitance with respect to the deflection  $x$ .

$$\frac{dC_{total}}{dx} = N_{pair} \cdot \alpha \cdot \epsilon_0 \cdot h \cdot L_{overlap} \left( \frac{1}{(d_1 - x)^2} - \frac{1}{(d_2 + x)^2} \right) \quad (2.34)$$

In post-CMOS processed MEMS accelerometers, finger triplets take place of finger pairs in conventional bulk-micromachined accelerometers [22-24]. One is the sense finger attached to the proof mass while the other two are complementary fixed fingers attached to separate fixed electrodes. Figure 2.7 illustrates interdigitated fingers, where the three of them form a capacitive pair, which can be used to build one branch of the fully-differential accelerometer sensor in Figure 2.8 (b) and (c).

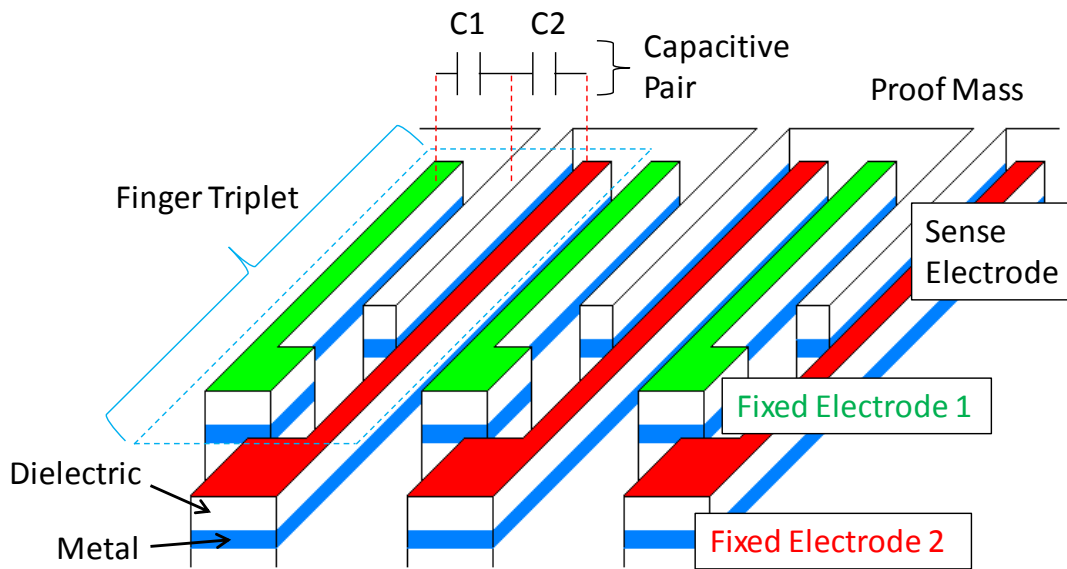


**Figure 2.7:** CMOS-MEMS sensor's finger array composed of interdigitated fingers form compositions allowing differential sense of accelerations.

The discreteness of the fixed electrode fingers provides the addition or subtraction of them from each other. Thus, the capacitive sensitivity can be read in a differential manner.

$$C_{total} = C_1 \quad (2.35)$$

$$C_{total} = N_{triplet} \alpha \epsilon_0 h L_{overlap} \frac{1}{d_1 - x} \quad (2.36)$$

$$\frac{dC_{total}}{dx} = N_{triplet} \alpha \epsilon_0 h L_{overlap} \frac{1}{(d_1 - x)^2} \quad (2.37)$$

where  $N_{triplet}$  represents the number of interdigitated fingers. The advantage of employment of the interdigitated fingers is the cancelation of the anti-gap capacitance, therefore the sensitivity increase slightly.

In order to witness the increase in sensitivities, a comparison with MATLAB is carried out using the same variables except the area occupied for both interdigitated finger arrays and comb finger arrays. Therefore, the definition of sensitivities per the unit length would be more accurate to evaluate the advantage of interdigitated fingers over the comb type ones. Figure 2.11 shows the difference between the sensitivities of the two configurations with area normalization.

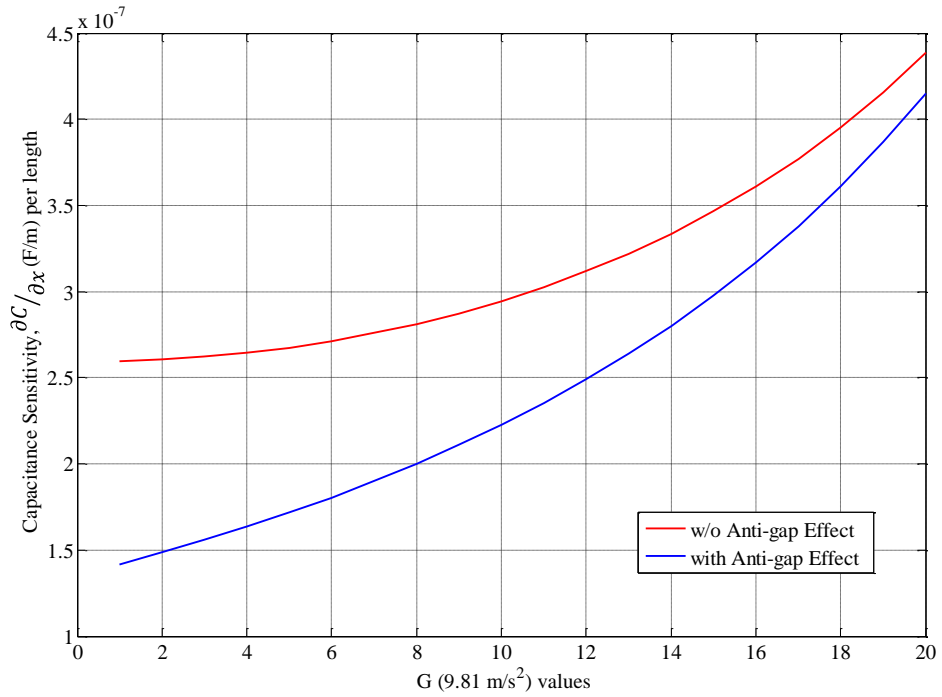


**Figure 2.8:** The anti-gap effect is more noticeable at low-g values, and its effect decreases at high-g values.

According to the calculation of the single branches of the configurations in Figure 2.5 (b) and (c), the difference in capacitance sensitivities are 2 times larger in low-G accelerations. However, the practical sensitivities are always less than the estimated

ones due to structural curling, which arises from the internal stress of the stacked metal-dielectrics, and metal misalignments [22-24, 47].

The realization of crossovers by multi-layer metals is possible by ad hoc methods as in glass lamination [38] or via openings [49] in bulk micro machined sensors. In addition to those methods, it is possible to realize the interdigitated fingers as in CMOS-MEMS accelerometers by vias through the buried oxide (BOX) layer of the Silicon-on-Insulator (SOI) wafer. Working with the SOI wafer is essential by the advantage of BOX layer's placement at the middle of the wafer. The exact placement of the BOX layer at the middle eases the process and makes it repeatable. Although the process repeatability is sustained, the most important point is forming the multi-layer connections between the isolated electrodes that reside in the device layer. Shorting the isolated electrodes is possible by metallization over the opened vias in the BOX layer. Through the vias, isolated Silicon electrodes connect to each other forming interdigitated electrode triplets. The Figure 2.12 illustrates the connection of interdigitated electrodes by metallization forming a capacitance pair.

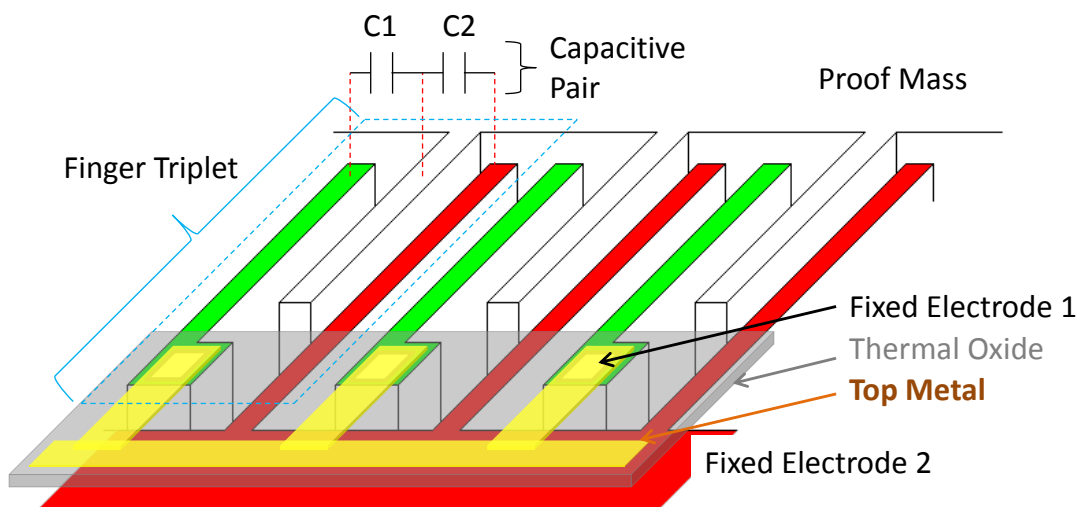


**Figure 2.9:** One of the fixed fingers of the differential finger triplets make connections through the vias on BOX layer of the SOI wafer.

With the proposed design, the capacitance pair formed between the interdigitated electrodes is saved from the negative capacitance term in the comb finger arrays, which is the source of the sensitivity loss in bulk-micromachined devices. Moreover, some of the area is saved for additional fingers that can be employed in place of

on-chip reference capacitors utilized in the read-out circuitry. If not, the extra finger, which fit into place of anti-gap, can be used for increasing the overall sensitivity of the system.

After putting the process of the proposed design forward, the design of the sensor can be carried out. The sensor design can be started by identifying some key parameters, which are used to find desired capacitance sensitivities and operation ranges. Table 2.1 shows the design parameters used in defining the sensor's performance parameters for the fully-differential sensor employing interdigitated sense electrodes based on the proposed process on SOI wafer.

**Table 2.1:** The design parameters take place in determination of the performance of the fully-differential mechanical sensor element with interdigitated sense fingers. The parameters also include readout specific parameters, as duty cycle.

<b>Design Parameters</b>			
<b>Young's Modulus</b>	E	<b>Spring Length</b>	L <sub>s</sub>
<b>Permittivity of Air</b>	$\epsilon_0$	<b>Spring Width</b>	W <sub>s</sub>
<b>Finger Length</b>	L <sub>f</sub>	<b># of Springs</b>	N <sub>springs</sub>
<b>Finger Width</b>	W <sub>f</sub>	<b>Thickness</b>	h
<b>Gap Size</b>	d	<b>Boltzmann</b>	k <sub>B</sub>
<b># of Fingers per Pad</b>	N <sub>fingers</sub>	<b>Temperature</b>	T
<b>Air damping</b>	$\mu_{\text{air}}$	<b>Duty Cycle</b>	c
<b>Gravity</b>	g	<b>Spring Length</b>	L <sub>s</sub>

Among above design parameters, the non-ideality parameter is the correction factor related with the process mismatches such as notching, scalloping, non-ideal finger gap etching, and fringing fields that accumulate at the finger edges and circular parts of the structures. By using the design parameters the performance of the sensor can be calculated with the formulations given in Table 2.2.

**Table 2.2:** The performance parameters are used to characterize the sensor and their equations using the above design parameters.

Identity	Equation
Spring Constant (k)	$N_{springs} \cdot E \cdot h \cdot (Ws/Ls)^3$
Resonance Frequency (f <sub>0</sub> )	$1/2\pi \cdot \sqrt{k/m}$
μ effective (μ <sub>eff</sub> )	$\mu_{air} \cdot (1 - 0.6 \cdot h/Lf)$
Damping Coefficient (b)	$N_{fingers} \cdot \mu_{eff} \cdot Lf \cdot (h/d)^3$
Quality Factor (Q)	$\sqrt{k \cdot m}/b$
Deflection (x)	$m \cdot g/k$
Nominal Capacitance (Crest, x=0)[50]	$\frac{\epsilon_0 \cdot Lf \cdot h \cdot N_{fingers}}{d - x}$ $\cdot \left( 1 + \frac{(d - x) \cdot \left( 1 + \log\left(\frac{2\pi \cdot Lf}{d - x}\right)\right)}{\pi \cdot Lf} \right)$ $+ \frac{2(d - x) \cdot \log\left(1 + \frac{2Wf}{d - x} + 2\sqrt{\frac{Wf}{d - x} + \left(\frac{Wf}{d - x}\right)^2}\right)}{\pi \cdot Lf}$
Capacitance Sensitivity @0g (∂C <sub>0</sub> /∂x)	$\frac{\partial C_{rest}}{\partial x}$
Operation Range (R) (Closed-Loop)	$\frac{\partial C_0}{\partial x} \cdot \frac{V_{DD}^2}{m \cdot g} (1 - 8 \times 10^{-7} c)$
Scale Factor (SF)	$\frac{m}{k} \cdot \frac{\partial C_0}{\partial x} \cdot \frac{3.3}{C_{int}}$
Brownian Noise (a <sub>n</sub> )	$\frac{1}{g} \sqrt{\frac{4k_B \cdot T \cdot b}{m^2}}$

Note that the nominal capacitance calculation includes the fringing fields between fingers and side wall thickness effects [50]. The introduction of these effects into the calculations provides more accurate results of nominal capacitance and capacitance sensitivity values.

After defining the equations used in sensor design, the verification of the designs can succeed.

## 2.3 Fully-Differential MEMS Accelerometer's Design and Verification

Last step before the fabrication is the verification of the design with FEM tool and MATLAB. Having CoventoreWARE made possible to simulate the fabrication and check whether the calculation results are consistent with the capacitance and stress simulation results. The first step of a simulation is constructing the solid model of the sensor from its layout, and meshing the solid model of the device into finite elements with adjusting the mesh sizes. Decreasing mesh sizes take place until a convergence exists in the results of successive simulations. The simulations comprise the calculation of capacitance matrixes, stresses at joints, and modal analyses. Simulations of two types of devices take place in the following sections, which includes the first and the second generation sensor designs.

### 2.3.1 1<sup>st</sup> Generation Sensor

The first generation sensor is designed to satisfy a high yield process with 3  $\mu\text{m}$  gap size, and a low-noise operation with increased sensor size. The two of the four pads from the electrodes take contact from the top metallization, whereas the other two take contact from the complementary electrodes.

**Table 2.3:** Design and performance parameters of the 1<sup>st</sup> generation sensors.

Design Parameters		Performance Parameters	
<b>Proof Mass</b>	$3.83 \times 10^{-7}$ Kg	<b>Operation Range (9.3 V)</b>	$\pm 8.1$ g
<b>Die Area</b>	$5370 \times 4808$ $\mu\text{m}^2$	<b>Damping Coefficient</b>	$2.0 \times 10^{-3}$ Kg/s
<b>Finger Overlap</b>	155 $\mu\text{m}$	<b>Brownian Noise</b>	1.7 $\mu\text{g}/\sqrt{\text{Hz}}$
<b>Gap Distance</b>	3 $\mu\text{m}$	<b>Nominal Capacitance</b>	4.4 pF
<b># of Fingers per Pad</b>	256	<b>Capacitance Sensitivity @0g</b>	$1.39 \times 10^{-6}$ F/m
<b>Spring Constant</b>	214 N/m	<b>Capacitance Change @1g</b>	4.48 fF
<b>Resonance Frequency</b>	3776 Hz	<b>Capacitance Change @1V</b>	4.4 fF
<b>Quality Factor</b>	4.5	<b><math>V_{\text{pull-in}}</math></b>	9.0 V

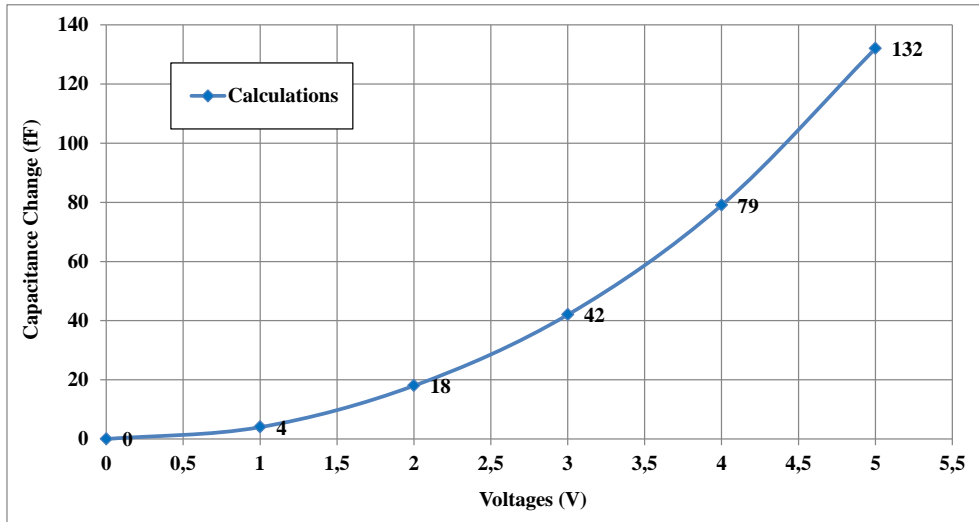


**Figure 2.10:** The expected sensitivities of the sensor between 0 and 5 Volts by 1 Volt increments. The capacitance change is the deflection times the capacitance sensitivity at desired voltages.

With the defined performances parameters the sensor layout is prepared in the Cadence environment. Figure 2.11 shows the 1<sup>st</sup> generation sensor layout.

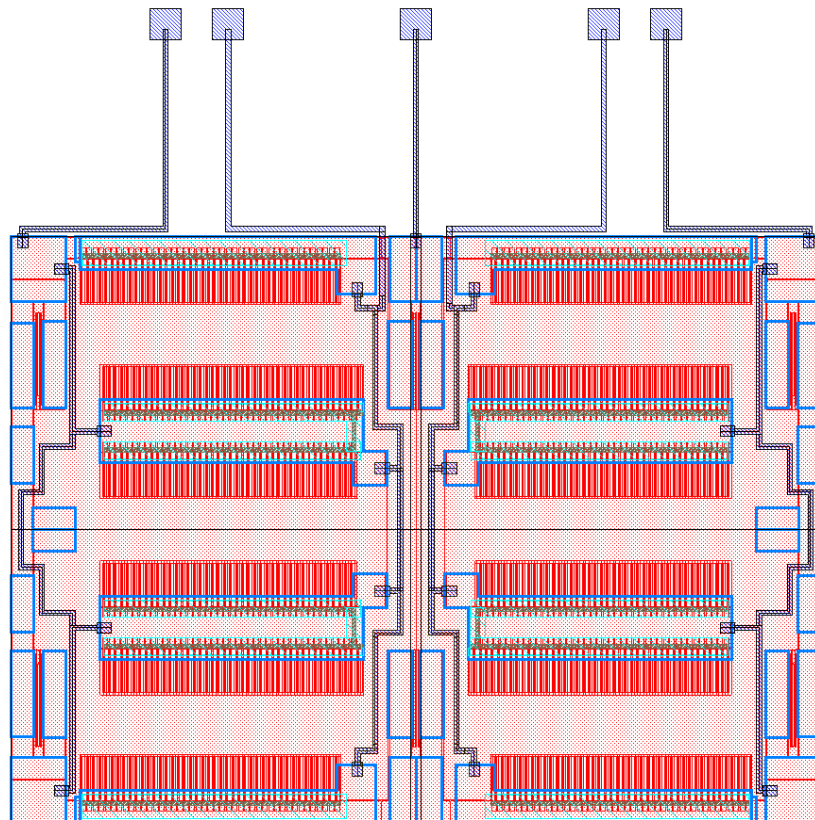


**Figure 2.11:** 1<sup>st</sup> generation sensor layout. The sensor includes five outputs to the readout.

According to the layout, the two of the pads located close to the middle of the proof mass pad have connections to the isolated fingers by top metals through the Silicon and vias on the BOX layer. The vias reside on the isolated fixed fingers in the interdigitated finger triplet. The two of the remaining pads have connections from the other fixed fingers through the Silicon, while the pad at the middle has connection to the proof-mass. It is expected to see a higher resistance in the pads connecting the top metals since the charges have to travel through two Si-metal interfaces two times.

The following section discusses the modal analysis results of the demonstrated sensor.

### 2.3.1.1 Modal Analysis of the 1<sup>st</sup>Generation Sensor

Bandwidth of the accelerometer system is directly related with the resonant frequency of the sensor. Resonant frequency is the first mode of the structure acting in sense direction in contrast with the other modes acting in different directions in higher frequencies. Analysis of modes requires the construction of the solid model of the sensor from its layout. The solid model constructed for the simulation resembles the simplified model of the original structure. In the model of the structure, the fingers and perforation holes are lumped and round corners are tapered to ease the simulation. Figure 2.12 shows the constructed solid model for the simulation, and Table 2.4 presents the first three modes of the solid model. The first mode of the sensor is used in determining the operation bandwidth of the sensor, which is proportional to one-tenth of the resonance frequency.

**Table 2.4:** The first three modes of the solid model.

Number of Modes	1	2	3
Frequency (kHz)	3.6	13.0	15.9

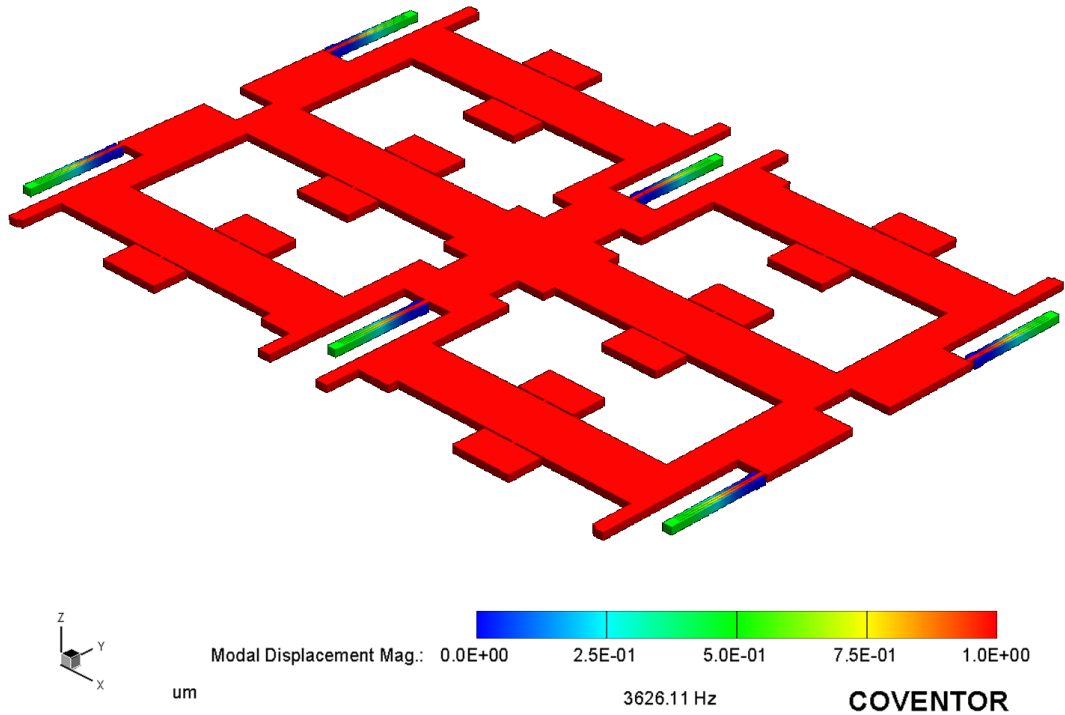
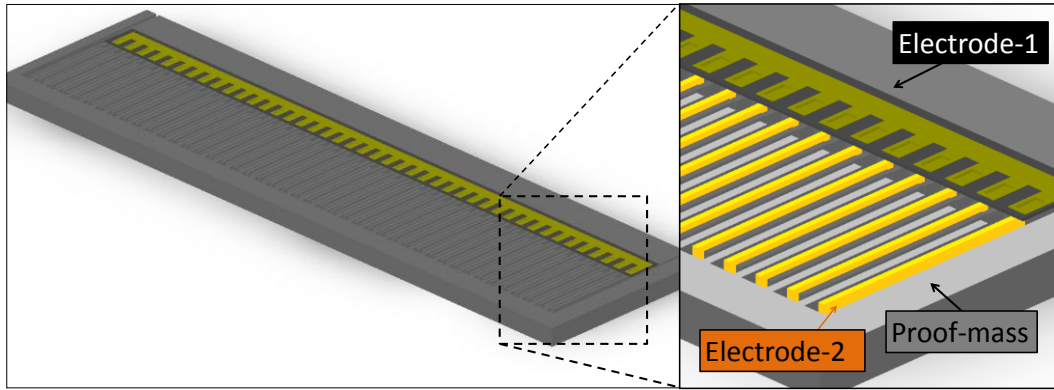


**Figure 2.12:** The solid model constructed for the modal simulation resonates at 3.6 kHz. The red colored parts in the model have the biggest deflection, while the anchors of the spring have zero deflection.

The other modes represent the transverse motion of the sensor, which are desired to be much larger than the resonant frequency. According to the simulations the resonant frequency of the solid model is very close to the calculated value of the design at Table 2.3.

### 2.3.1.2 Capacitance Analysis

The capacitance analysis covers the exact nominal capacitances of two different finger arrays having interdigitated finger triplets. Both of the arrays find place in the sensor area having a difference with the anchor where the top metal makes connection to the bottom pad metal routing. Two different simulations of the arrays are necessary to find their contributions to the total nominal capacitance. Figure 2.13 illustrates the first of the arrays, which has no anchor placement. The anchor placement connects the top metallization to the pad metal routings through the Si.



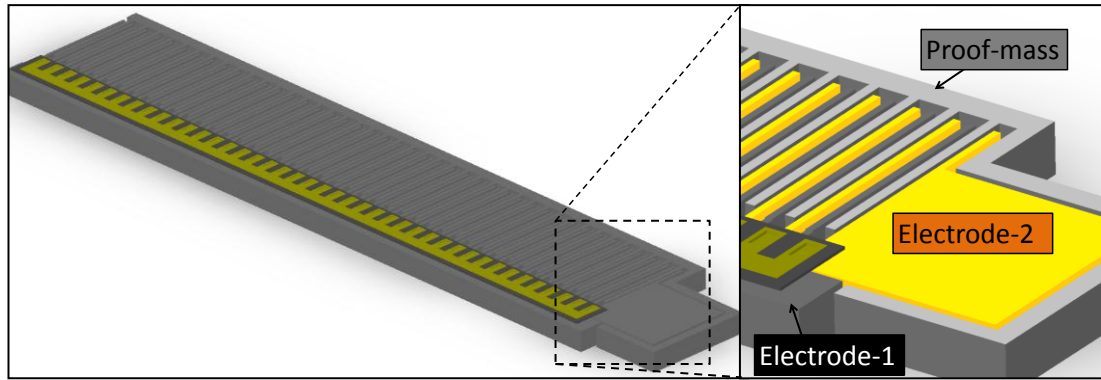
**Figure 2.13:** The solid model of the interdigitated finger arrays with 3  $\mu\text{m}$  finger gaps. The highlighted fingers with orange are connected to each other from the top contact metallization.

Table 2.5 gives the capacitance simulation results according to the model above with decreasing mesh size. The ones highlighted in red color show the static capacitances between the proof mass and fixed sense Electrode-1 and Electrode-2, which are the sum of the grey and orange colored electrodes in Figure 2.13, respectively.

**Table 2.5:** The capacitance matrix shows the total capacitance between the conductors. The conductors are the Proof Mass, and the fixed finger electrodes, Electrode-1 and Electrode-2.

Capacitance Matrices (fF)				
		Electrode-2	Electrode-1	Proof Mass
Default Mesh Size (10)	Electrode-2	238	-150	-886
	Electrode-1	-150	237	-869
	Proof Mass	-886	-869	176
Half Mesh Size (5)	Electrode-2	248	-161	-875
	Electrode-1	-161	248	-876
	Proof Mass	-875	-876	175

The following analysis shows the capacitance simulation results with the solid model of the anchored electrode array. Figure 2.14 illustrates the solid model and Table 2.6 gives the capacitance matrix results.



**Figure 2.14:** The solid model of the interdigitated finger arrays with the anchor.

**Table 2.6:** The capacitance matrix shows the total capacitance of the anchored array. The conductors are the Proof Mass, and the fixed finger electrodes, Electrode-1 and Electrode-2.

Capacitance Matrices (fF)				
		Electrode-2	Electrode-1	Proof Mass
Default Mesh Size (10)	Electrode-2	243	-156	-876
	Electrode-1	-156	238	-826
	Proof Mass	-876	-826	170
Half Mesh Size (5)	Electrode-2	236	-148	-878
	Electrode-1	-148	231	-828
	Proof Mass	-878	-828	171

From the results, it is noticeable that the electrodes with an anchor have slightly higher capacitances than the one without the anchor between Electrode-2 and Proof Mass. The difference in capacitance in both electrodes satisfies the expectations where the anchor sidewall contributes to the nominal capacitance. Based on the above simulations, the capacitance between the pads and the proof mass equals to 5.261 pF for the two pads very near the middle proof mass pad, and 5.063 pF for the other remaining two pads. Capacitances obtained from the simulations are 14.5 and 11.2% larger than the calculated ones in Table 2.3. The difference shows that hand calculations are close to the simulated values, which are acceptable as in comparison with the designs in the literature [10].

### 2.3.2 2<sup>nd</sup> Generation Sensor

The 2<sup>nd</sup> generation sensor differs from the first one with its finger gaps and etch-holes on the proof mass. The gaps of this design shrink to 1.8  $\mu\text{m}$  for enhancing the capacitance sensitivity after a settled process. The etch-holes on the proof mass area provide an exit for the photoresist (PR) residing under the mass and between the fingers. The holes also provide an entrance for the piranha solution during the cleaning of the sensor dies. Moreover, the design lengths and widths are chosen to satisfy the same spring constant and mass values as in devices previously fabricated with bulk micromachining, implementing the comb finger arrays processes, in METU-MEMS Research Center. However, since the fully- differential design requires four electrodes, the damping coefficient will increase with the number of fingers. Therefore, more noise is expected from the sensor in comparison with the 1<sup>st</sup> generation design. Table 2.7 shows the expected design and performance parameters of the 2<sup>nd</sup> generation design.

**Table 2.7:** Design and performance parameters of the 2<sup>nd</sup> generation sensors.

Design Parameters (drawn/estimate)		Performance Parameters	
<b>Proof Mass</b>	$2.30 \times 10^{-7}$ Kg	<b>Operation Range (9.3 V)</b>	$\pm 53.7$ g
<b>Die Area</b>	$6260 \times 3740 \mu\text{m}^2$	<b>Damping Coefficient</b>	$1.4 \times 10^{-2}$ Kg/s
<b>Finger Overlap Length</b>	160 $\mu\text{m}$	<b>Brownian Noise</b>	7.2 $\mu\text{g}/\sqrt{\text{Hz}}$
<b>Gap Distance</b>	1.8 $\mu\text{m}$	<b>Nominal Capacitance</b>	10.5 pF
<b># of Fingers per Pad</b>	352	<b>Capacitance Sensitivity @0g</b>	$5.6 \times 10^{-6}$ F/m
<b>Spring Constant</b>	45 N/m	<b>Capacitance Change @1g</b>	424 fF
<b>Resonance Frequency</b>	2237 Hz	<b>Capacitance Change @1V</b>	435 fF
<b>Quality Factor</b>	0.23	<b>V<sub>pull-in</sub></b>	1.9 V

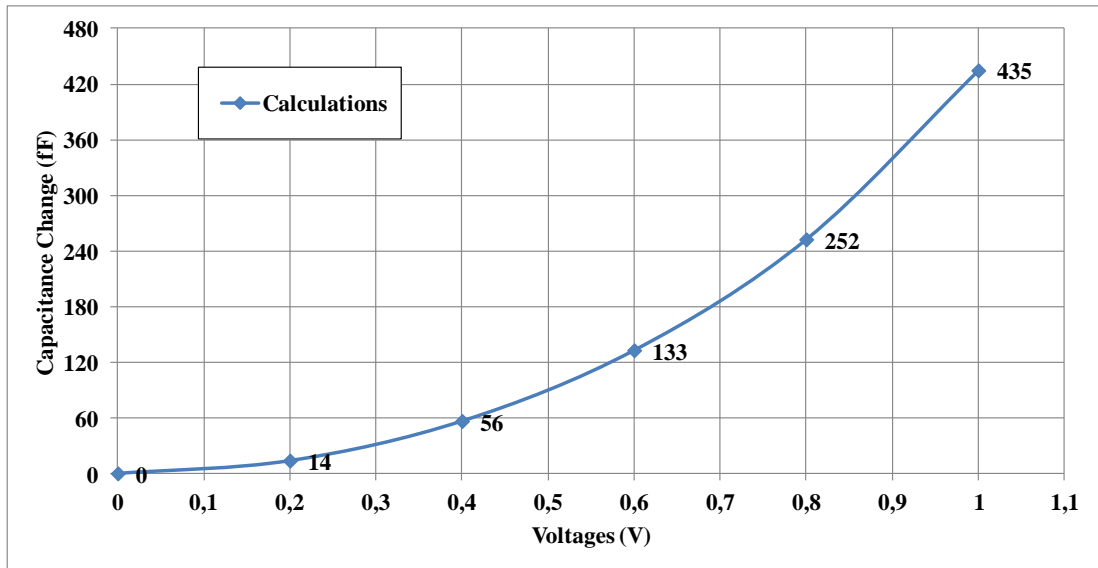


**Figure 2.15:** The expected sensitivities of the sensor between 0 and 1 Volts. The sensitivity can only be calculated for voltages below the pull-in voltage of the sensor, since the capacitance per pad will be higher due to decreased gap size.

Figure 2.16 shows the drawn layout for the 2<sup>nd</sup> generation sensor design.

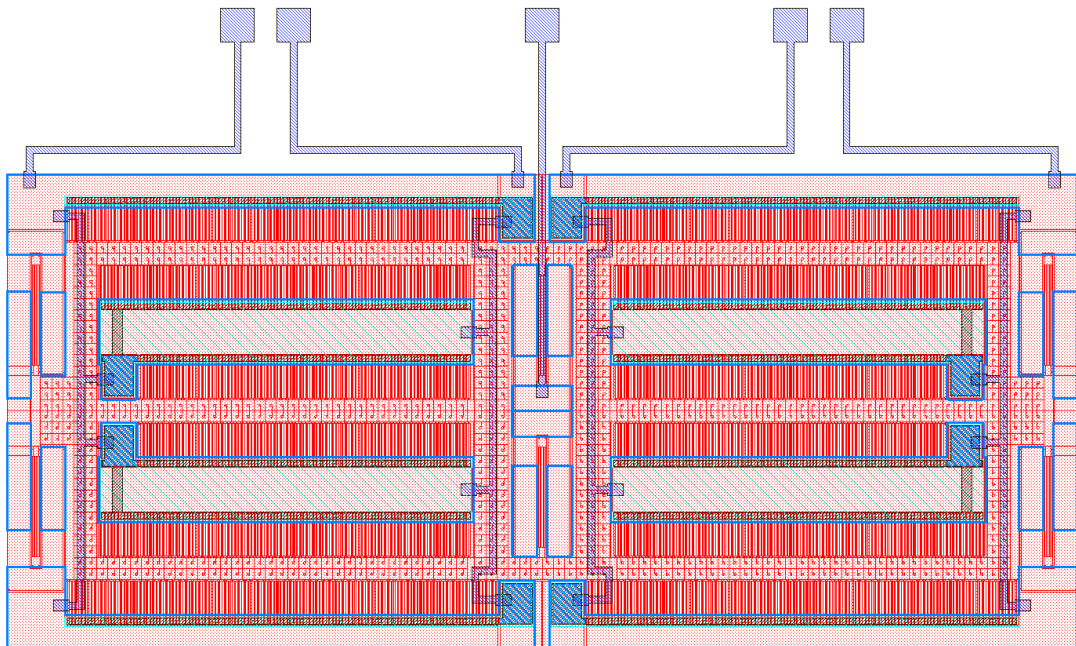


**Figure 2.16:** The layout of the 2<sup>nd</sup> generation sensor includes etch-holes on the surface of the proof mass that are detectable on the proof mass surface. In addition, the connections to the pads have routings in order to satisfy more equally distributed resistances different than the first generation design.

### 2.3.2.1 Modal Analysis

The modal analysis of the sensor has a smaller value than the 1<sup>st</sup> generation sensor. The reason of the smaller resonance frequency is the smaller spring constant of the sensor and its smaller mass. Despite the mass decrease from  $3.80 \times 10^{-7}$  Kg to  $2.30 \times 10^{-7}$  Kg, the spring constant, which is inverselyproportional with the mass, decreases four-fold from 214 N/m to 46 N/m. Table 2.8 shows the first three modes of the constructed solid model for the sensor. The low spring constant to mass ration results with a reduction in resonance frequency; therefore shrinking in the bandwidth.

**Table 2.8:** The first three modes of the solid model.

Number of Modes	1	2	3
Frequency (kHz)	2.2	11.2	12.7

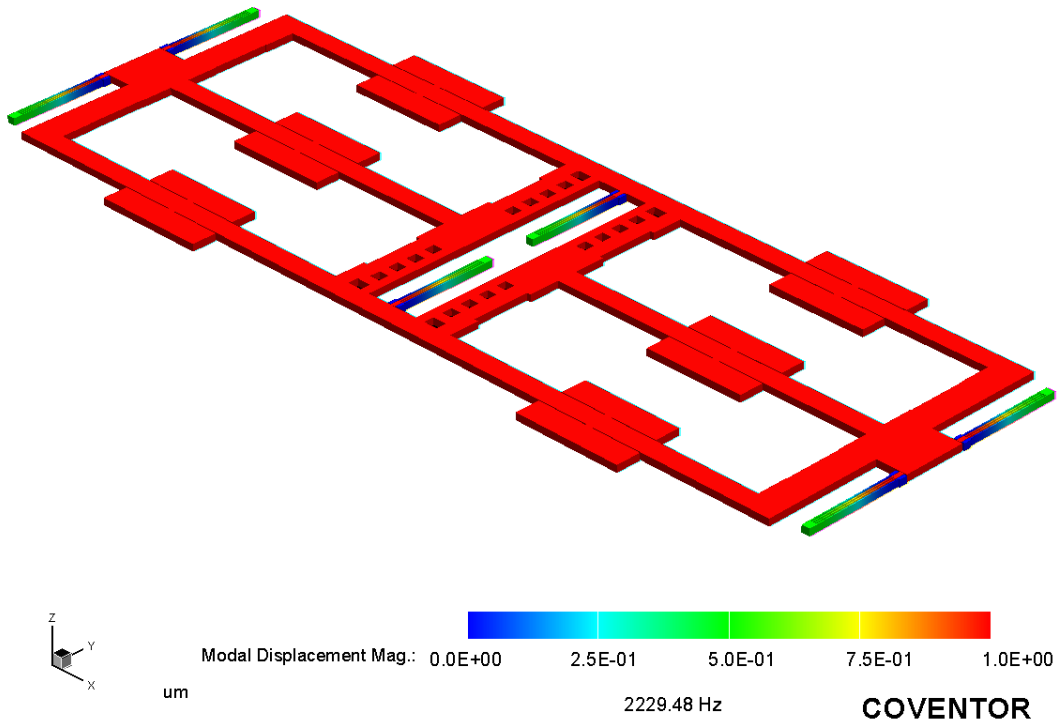


**Figure 2.17:** The solid model constructed for the modal simulation resonates at 2.2 kHz. The red parts of the model have the biggest deflection, while the anchors of the spring have zero deflection.

### 2.3.2.2 Capacitance Analysis

The capacitances residing in the sensor die area can be represented by the calculations according to the simulation of one electrode. Figure 2.18 shows a solid model of the middle anchor. Table 2.9 shows the capacitances matrix of the solid model in Figure 2.18.

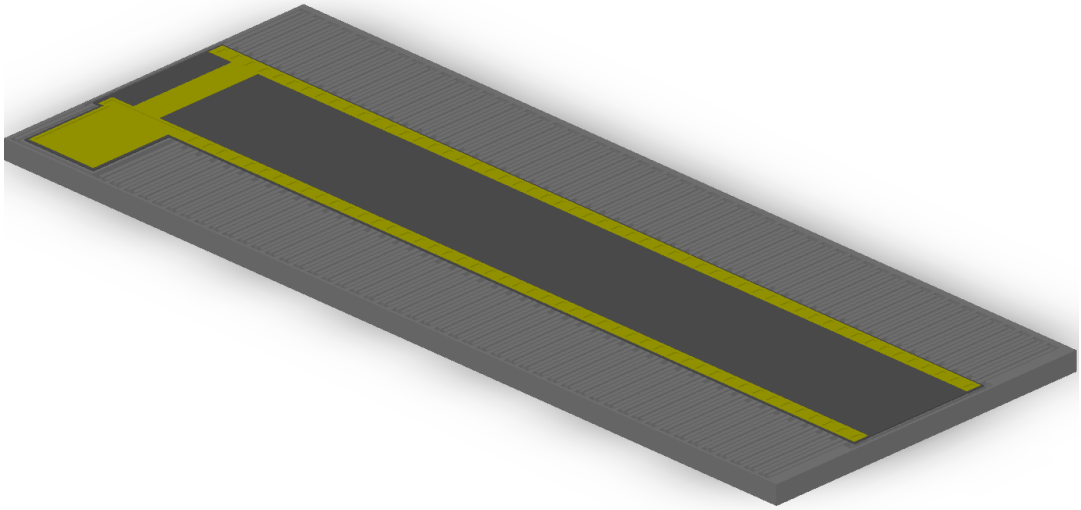


**Figure 2.18:** The solid model of the interdigitated finger arrays for the 2<sup>nd</sup> generation sensor with 1.8  $\mu\text{m}$  finger gaps.

**Table 2.9:** The capacitance matrix of the middle anchor.

Capacitance Matrices (pF)				
Default Mesh Size (5)		Electrode-2	Electrode-1	Proof Mass
	Electrode-2	6.162	-3.222	-2.940
	Electrode-1	-3.222	6.208	-2.986
	Proof Mass	-2.940	-2.986	5.926

With the above simulation results, the total nominal capacitance per pad sums up to 9.50 pF, taking into account the results of the capacitance matrix for both Electrode-1 at the middle anchor and Electrode-2. The simulated values indicate a 14.7% difference between the simulated results and hand calculated nominal capacitances of 9.50 pF in Table 2.7. The percentage wise difference between the simulation and hand calculation is consistent with the discrepancy of the calculation and simulation results of the 1<sup>st</sup> generation sensor's nominal capacitance, which is 14.5%.

## **2.4 Summary of the Chapter**

The chapter introduced the theory of MEMS accelerometers together with their static and dynamic responses. Then, the sensing interfaces were analyzed, and it's shown that the best configuration for detecting of the acceleration was fully-differential architecture. The implementation of the architecture was shown in CMOS-MEMS accelerometers with interdigitated sense arrays. The adaptation of the interdigitated sense arrays to the bulk-micromachined sensors was discussed, and an appropriate sensor design was put forward. Two designs were presented for the proposed process together with their modal and capacitance analyses.

## **CHAPTER 3**

### **FABRICATION OF THE FULLY-DIFFERENTIAL MEMS ACCELEROMETER WITH INTERDIGITATED FINGERS**

This chapter explains the fabrication of the Fully-differential (FD) MEMS accelerometer with interdigitated fingers. The fabrication of the FD sensors makes use of the bulk-micromachining techniques on a Silicon-on-Insulator (SOI) wafer. The buried oxide (BOX) layer of the SOI wafer is utilized to accomplish the desired fabrication methods. The whole fabrication consists of processing seven masks, which are drawn in the Cadence environment. The chapter is divided into four sections and they are summarized as follow.

Section 3.1 introduces the fabrication techniques which are briefly introduced in Chapter 1. The section promotes the surface and bulk-micromachining as general as the fabrication in this thesis requires. The complicated processes such as RIE and DRIE are clarified based on the basics of micro-fabrication. Then, the fabrication can be explained in detail.

Section 3.2 shows the processes of the FD sensor based on the techniques provided in the previous section. The section also covers the stress related problems on SOI wafers and anodic bonding specific problems with their solutions. The appropriate solutions for the problems take place with discussions after the fabrication steps.

Section 3.3 demonstrates the fabrication results. A comparison is made between the fabricated sensors with their initial performance parameters. The reason of deviation in the results is discussed.

Finally, Section 3.3 summarizes the chapter.

### **3.1 Introduction to the MEMS Fabrication**

The micromachining of MEMS devices is composed of various wet and dry etch methods gathered under two headings: Surface and Bulk micromachining. The existing methods are developed and based on the mechanical and structural properties of the MEMS materials. The etching of the MEMS materials takes shape according to the Miller indices ( $\langle 100 \rangle$ ,  $\langle 110 \rangle$ ,  $\langle 111 \rangle$ ) of crystals. The dependence on the crystal orientation changes the isotropy and etch rate. The etch rate in isotropic etches are the same in all Miller directions and greatly varies in anisotropic etches. For instance, wet etches can be both isotropic and anisotropic, whereas dry etches are generally isotropic. Although, the etch rate in wet etches are more selective than dry etches; the dry etches are prominent over wet etches in terms of directionality. Against all differences, both etch techniques extensively take place in processing of device and substrate wafers. The directional etches of the thick device wafers gives rise to the formations of high aspect ratios and small feature sizes by dry etch methods. The common dry etch methods are Reactive Ion Etching (RIE) and Deep RIE (DRIE) where both methods are based on the bombardment of the accelerated ions towards the wafer's surface. Accelerated ions mean free path increases under the vacuum environment in the chamber. Hence, the fabrication of small feature sized devices becomes possible. On the other hand, the substrate wafers are generally processed with wet etch methods comprising the isotropic wet etches of the wafer as well as the deposited materials.

In general, silicon is chosen as the device wafer in MEMS fabrication because of its abundance in the earth's crust. Moreover, Silicon is in an indispensable position by its highly developed production technology, and widespread distribution chain to the world market. The production technology of the silicon allows the producers to play with the properties of the Silicon in its electrical, thermal, and mechanical

characteristics by the amount of the doping that the wafers undergo, as well as in the production of the wafers in different orientations. Besides those, the technology provides the MEMS market with the varieties of the Silicon wafers. For example, Silicon-on-Insulator (SOI), double SOI, and epitaxially grown (Epi) wafers play an important role in the fabrication of the multifarious unique devices. The orientation of the wafers and their doping amount directly affect the processing technique of those devices. On the other hand, the glass wafers are implemented as the substrates of the Silicon devices. Their process has to be compatible with the micromachining techniques and the process of the Silicon wafer. Borosilicate glass wafers have close thermal coefficient of expansion to Silicon's, therefore are used often as substrates to match with the Silicon. The surface and bulk-micromachining techniques are extensively used in the processing of the devices.

Both-micromachining techniques have advantages and disadvantages over each other in many ways. Surface micromachining is the fabrication of the devices on top of the substrate wafers by patterning the deposited thin film layers and the devices are released by etching of the sacrificial layers. The compatibility of the surface micromachining with the IC fabrication makes possible to monolithically fabricate the devices with post-CMOS processes. However, the drawbacks of post-CMOS process exist as in the buckling of the structural layers. Multiple stacks of deposited metal-dielectric layers generate internal stress causing the buckling of the devices [22-24]. Moreover, metal misalignments, from process to process, worsen the repeatability [47]. Therefore, in comparison with the bulk micromachining, the fabricated devices using the surface micromachining techniques have small masses, which can be a certain restriction for the fabrication of the design, where large mass devices find place.

Bulk-micromachining means the processing of wafers, where the devices originate from the bulk of the wafer. The existing techniques in the literature based on the Dissolved Wafer Process (DWP) and Silicon-on-Glass (SOG) processes. The DWP is etching of the Silicon wafer with Etilen Diamine Pyrocatechol (EDP) until the etch stopping highly Boron doped layer Silicon. The structures of the devices are previously defined by DRIE before the anodic bonding of the Silicon to glass wafer.

But, in SOG processes the structures are defined by DRIE after the anodic bonding of SOI and glass wafers. Both methods let the development of Dissolved Epitaxial Wafer Process (DEWP)[12] and modified SOG processes [51]. As mentioned before, the process takes the advantage of wet and dry etches extensively. The sensor design being the subject of this thesis is also carried out by using the bulk-micromachining techniques incorporated with the wet and dry etch methods.

## **3.2 Fully-Differential (FD) Accelerometer Process Overview**

FD capacitive accelerometer fabrication, which requires 7 masks, follows a more complex process than the aforementioned conventional DWP, DEWP, SOG, and modified SOG bulk micromachining processes. The realized sensor fabrication includes the process of SOI and glass wafers and the processes after their anodic bonding. The glass wafer processes make use of wet etch methods, while processes on the SOI wafer favor dry etch methods. Dry etch methods also covers a large portion of the post anodic bonding processes. The following chapters explain the FD accelerometer process in more detail.

### **3.2.1 Glass Wafer Process**

The glass wafer preparation is a two mask process. The process consists of the formation of anchors and pad metals. Anchors are used to fix the Silicon devices while metals climb over the anchors to carry induced charges from the electrodes to the readout.

#### **3.2.1.1 Anchor Formation**

The process starts with the cleaning of Borosilicate glass substrate in 1:1  $\text{H}_2\text{SO}_4:\text{H}_2\text{O}_2$  (piranha) solution for 30 min. The solution provides the cleaning of organic residues prior to the beginning of the process. The substrate process starts with 1 min. of Buffered HF (BHF) to roughen the glass wafer's surface for better adhesion of the metal mask which will be used for the formation of anchors. After that the substrate is subjected to 10 min. oven at 110°C to dehydrate the surface's moisture for enhancing the adhesion. Subsequently, the process follows the deposition of 100/1500 Å of Cr/Au metal mask layers by sputtering. The deposited

chromium layer is a well-known metal that increases the adherence of the Au atoms to the glass surface. Then the wafer is subjected again to dehydration for the lithography step. The SHIPLEY S1813 photoresist (PR) is spin coated on the wafer at a thickness of 1.3  $\mu\text{m}$ , and patterned using the anchor mask. Then the wafer is hard baked at 120°C oven for 40 min. to strengthen the PR for the metal mask formation. The last bake process also increases the protection of the metal mask to etching of the glass wafer by making the surface hydrophobic [52]. The metal mask is realized by successive gold, chromium, and diffused Au etches by commercial TRANSENE etchants. Any gold diffused under the glass surface masks the glass and prevents the formation of the recesses between the anchors. The anchor etch is made by HF solution having a concentration of 49% within a Teflon case, in pursuit of the metal mask formation. The anchor etch continues until the recesses reach a depth of 8-12  $\mu\text{m}$ . The measurement of the depth is made by VEECO DEKTAK surface profilometer. Finally, the remaining PR is stripped away by SVC 2000 PR stripper at 80°C for 20 min., and the metal mask is etched by Cr/Au etchants.

### **3.2.1.2 Pad Metal Formation**

The pad metallization process starts again with the surface roughing as in the beginning of the anchor formation. The wafer is dehydrated and 100/1500 Å Cr/Au layers are sputtered on the glass surface. The Cr layer deposited prior to the Au layer increases the strength of the adherence of Au to the glass surface during the piranha cleaning in anodic bonding step. This step is followed by the lithography of the metal deposited glass wafer with the spin coated SHIPLEY SPR 220-7 at a thickness of 7  $\mu\text{m}$ , which covers the wafer entirely. The coated PR is patterned with the pad metallization mask. After that, the PR is hard baked at 120°C oven for 40 minutes. Then, the deposited Cr/Au layer is patterned by successive gold, chromium, and diffused gold etches. The PR mask is stripped with PR stripper at 80°C after the formation of pad metals.

### **3.2.2 SOI Wafer Process**

Silicon wafer processing requires only one mask to define the structures. A straightforward lithography process is realized by patterning the spin coated SPR220-3 PR with device mask. The structures are defined by DRIE, which is a commonly used tool for high aspect ratio device formation. The DRIE selectively etches the device layer of the SOI wafer until the insulating BOX layer is reached. The PR is stripped in the chamber with the O<sub>2</sub> plasma after the etching. Therefore 35 μm deep trenches are formed with dry etching.

### **3.2.3 Anodic bonding of SOI and Glass Wafers**

Anodic bonding takes place after the processing of both SOI and glass wafers. Before the anodic bonding of SOI and glass wafers, the wafers need to be prepared in piranha solution to etch away the polymers left from the dry etches and possible PR residues. The roughness on the wafer surfaces decreases the bonding quality. In long piranha cleanings, the adherence of the pad metal lines patterned on the glass wafer's surface start to weaken, and eventually peel off from the glass surface. Therefore, the cleaning procedure takes 10 minutes for the glass wafer, while the cleaning of SOI wafer takes 30 minutes. Lastly, just before the anodic bonding, the SOI wafer is subjected to 1 min. of BHF etch to remove the native oxide on the Silicon surface. The sufficient native oxide thickness on the surface of the Silicon enhances the anodic bonding quality [53]. However, the quality of the contacts decreases without the removing the native oxide. While the anodic bonding occurs between the Silicon and glass interface, the gold contacts climbing on the Silicon anchors make eutectic bonding with the Silicon. The Au atoms diffuse in the Silicon, and the Cr adhesive layer diffuse into the Au. The quality of the anodic bonding can be characterized by the brownish color of the eutectic contacts which is a measure of the diffusion rate of the Silicon into the Au. Figure 3.1 shows the comparison of successful and unsuccessful contact formations.

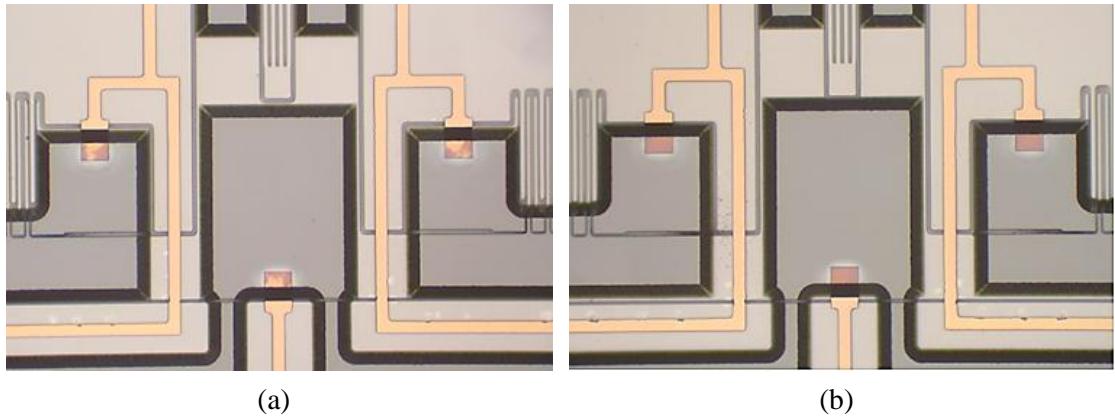


**Figure 3.1:** (a) Partially brown colored imperfect contacts have high resistances, (b) full brown colored contacts show the successful contacts with low resistances.

In Silicon and glass wafers anodic bonding, the voltage is applied between the wafers in temperatures lower than the eutectic temperature of the Au ( $363^{\circ}\text{C}$ ) metallization. Due to the generated electric field, the Sodium ions ( $\text{Na}^+$ ) doped in the glass wafer depletes the Si-glass interface leaving the oxygen ( $\text{O}_2$ ) atoms behind. The remaining  $\text{O}_2$  atoms interact with the Si atoms forming the Silicon dioxide ( $\text{SiO}_2$ ) layer [54]. In the case of the SOI and glass wafers anodic bonding the physic is slightly different than the simple Si-glass bonding.

The theory of anodic bonding of SOI wafer as in [54] depends on the resistor-capacitor series network assumption. Figure 3.2 shows the schematic of the anodic bonding of SOI and glass wafers with the assumed resistance and capacitances configuration.

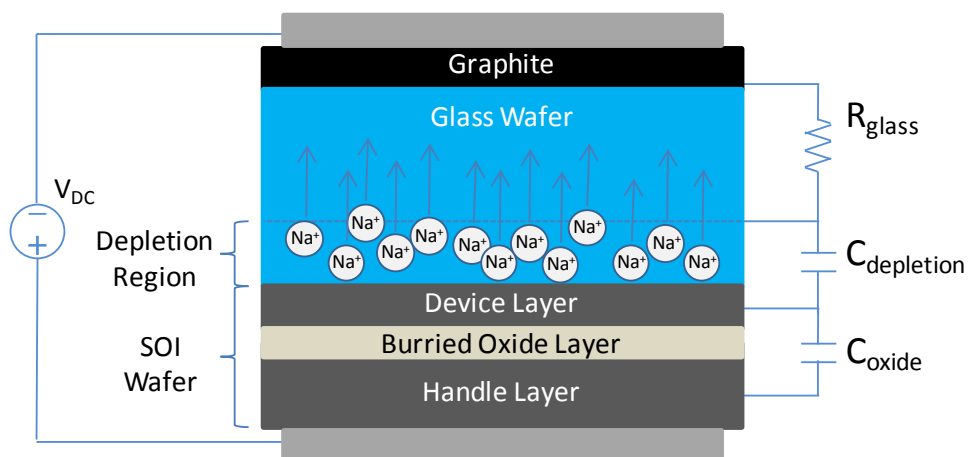


**Figure 3.2:** The schematic of the anodic bonding of SOI and glass wafers.

From top to bottom, the glass wafer is modeled as a resistance,  $R_{\text{glass}}$ . The glass wafer does not exhibit the behavior of a perfect insulator, since it hosts the Na ions. The Si-glass interface, where the  $\text{SiO}_2$  bond forms during the bonding, is the region Na ions deplete and form the  $C_{\text{depletion}}$ . The remaining SOI wafer forms the  $C_{\text{oxide}}$  with the insulating BOX layer serving as the dielectric slab between device and handle layers.

The anodic bonding of SOI and glass wafers takes place by applying 1200 V on the wafers at  $350^\circ\text{C}$  under a force of 1500 N. At the instant the voltage is applied,  $C_{\text{oxide}}$  acts as open circuit and applied voltage falls on the  $C_{\text{depletion}}$ . Due to the increase in thickness of the depletion region the current and voltage on the  $C_{\text{depletion}}$  decrease. At the same time the voltage on the  $C_{\text{oxide}}$  increases while the capacitances shares the charges. Towards the end of the bonding, the voltages on the capacitors meet at a certain value, while the current on the bond interface decreases to zero. The zero current signifies the formation of the  $\text{SiO}_2$  layer between the Si-glass interfaces.

### **3.2.4 Following Anodic Bonding Process**

Up to now, the SOI and glass wafers are processed with common wet and dry etch methods of bulk micromachining. Then, their bonding is made anodically. From now on, the bulk micromachining of the FD sensor process differentiates with processing of the BOX layer of SOI wafer. The processing of the top layer begins with the thinning process of the supporting  $450\ \mu\text{m}$  thick handle layer by DRIE in order to reach the BOX layer. Etching the handle layer may cause the relief of the stress of  $2\ \mu\text{m}$  thick thermally grown BOX layer by the formation of small cracks

Patterning the oxide and top deposited layers cause formation of the cracks, that cannot be detected with human eye. This, in turn, deforms the structures which results in a decrease in the yield. Therefore, a deposition of 200 nm oxide is made by Plasma Enhanced Chemical Vapor Deposition (PECVD) which is preferred for its conformal and low temperature deposition property, which allows the metals on the wafers to be processed without any harm. After that, unexpected consequences of the possible cracks are prevented by a great amount. Note that, the buckling results on the wafers due to internal stress of the deposited oxide layer, if the deposited

PECVD oxide is thicker. Figure 3.3 shows the wafer with removed handle layer by DRIE etching.

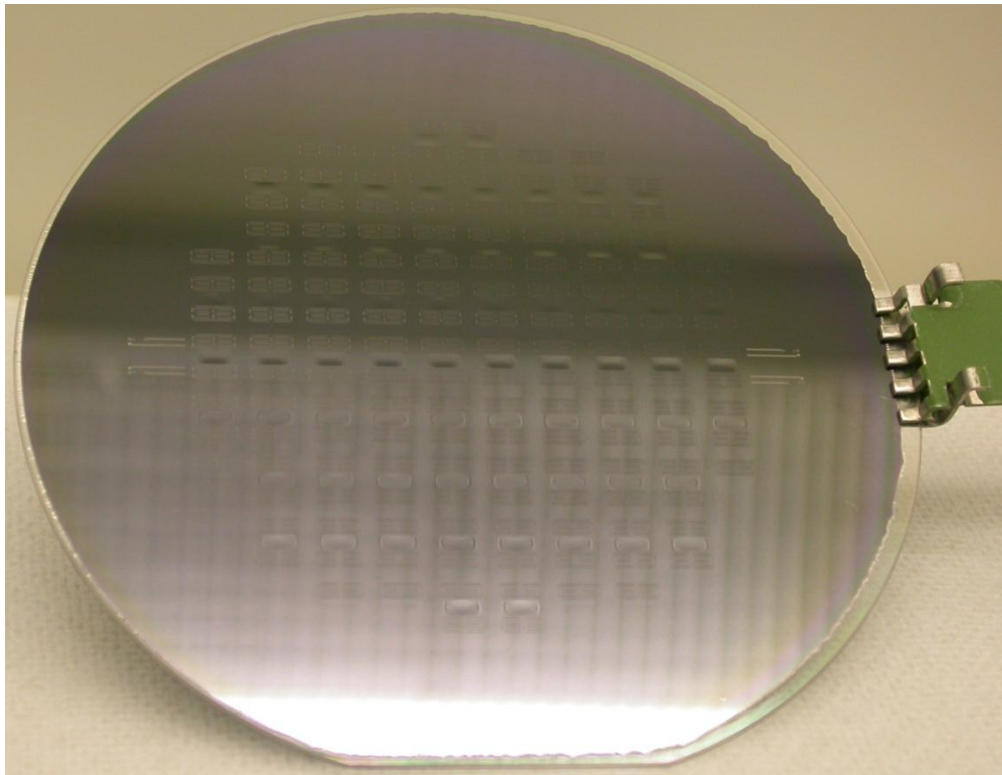


**Figure 3.3:** General view of a wafer with removed handle layer by DRIE etching.

From here on, one mask is used in every step of the process. The process follows with the formation of vias, top metal patterning, pad window opening, and release of the devices.

#### **3.2.4.1 Via Formation**

The wafer is dehydrated after the PECVD oxide deposition. The dehydrated wafer is spin coated with SPR 220-3 PR at a thickness of 3  $\mu\text{m}$ , since the vias have 2.2  $\mu\text{m}$  etch depth. The PR is patterned with vias mask and then, the wafer is subjected to RIE. After that, PR is stripped away by  $\text{O}_2$  plasma using NANOPLAS DSB 6000. The strip process employs  $\text{O}_2$  plasma instead of SVC 2000 due to the precipitated Fluorine atoms inside the protective PR mask [55].

### **3.2.4.2 Top Metal Formation**

The top metal deposition starts with the native oxide removal process. The native oxide that is grown on via openings has a great influence on the contact resistance values of the top contacts. The high resistance values of routings to the readout circuitry may affect the settling time of the accelerometer. After the native oxide removal, 100/3000 Å Cr/Au layers are deposited by the sputtering system without dehydration. The dehydrated wafer is spin covered with SPR220-3PR at a thickness of 3 μm to cover via openings. The PR is patterned by the top metal mask and followed by a hard bake of 120°C for 40 min. to endure the wet etch of the metals. Subsequent etch of Au, Cr, and diffused Au layers are followed by the PR stripping by O<sub>2</sub> plasma.

### **3.2.4.3 Pad Window Opening**

The next step is the pad window opening, which results in the access to the pads on the glass wafer's surface. The pads lie below the BOX and device layers of the SOI wafer. At first, the BOX layer and the deposited PECVD oxide must be etched to reach the device layer. Since the total thickness of the oxide layer to be etched is smaller than 3 μm, the spin-covered SPR220-3 PR satisfies the protection from RIE and DRIE. RIE etches the BOX layer with the PECVD deposited oxide, and DRIE etches the device layer of the SOI, subsequently. High selectivity of DRIE protects the previously spin covered PR along the etch time and the pads are uncovered by a timed etch. O<sub>2</sub> plasma cleans the PR mask on the wafer in the DRIE chamber. However, an over etching might not be avoided, unless a precise timing is made. The over etching might generate scratches on the pad metals, which reside under the pad window. The scratches on the metal are due to the O<sub>2</sub> plasma etching of the diffused Cr in the Au metal. Figure 3.4 shows the over etched pad window resulting with a small amount of scratching on the pads.

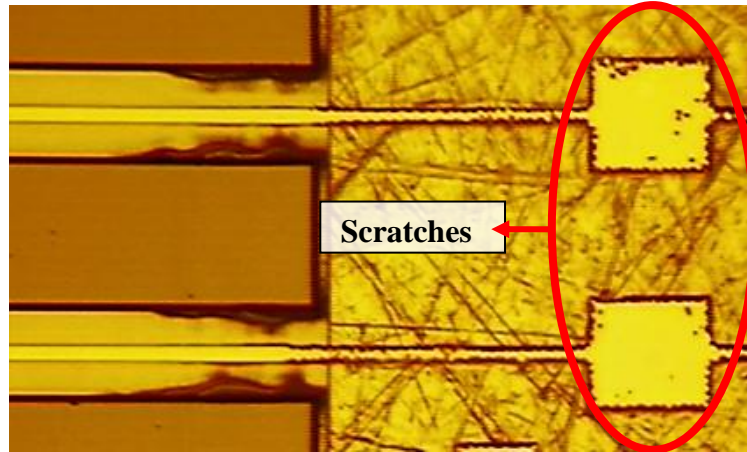


**Figure 3.4:** The pad routings' around has direct expose to O<sub>2</sub> plasma. The separations from the edges decrease as the routings go inside the sensor.

The problem is evitable by depositing a protective layer or terminating the DRIE and O<sub>2</sub> plasma processes, precisely. After the cleaning procedure the contact resistance measurement from the pads takes place. The resistance values between the pads are desired to be as low as possible. The expected values are on the order of 1-2 k $\Omega$  if proper native oxide cleaning is carried out before the metal deposition. The resistance value then can be reduced to the smaller values by thermal annealing. According to [56] 30 min. of thermal annealing at 200°C would decrease the resistances. Table 3.1 tabulates the measured resistance values after the thermal annealing process.

**Table 3.1:** The comparison of the resistances is made using the two dies of the 2<sup>nd</sup> generation sensor wafer.

Pads/ Die ID	F12 ( $\Omega$ )		C3 ( $\Omega$ )	
	Annealing Before	Annealing After	Annealing Before	Annealing After
1	573	1200	1130	36
2	557	290	577	60
3	431	470	582	-----
4	602	700	770	110

The annealing results show that the operation is not effective for some dies. Therefore, further optimization is necessary to optimize the resistance values of the metal lines.

#### 3.2.4.4 Release of the Devices

The last step of the process is the release of the devices by etching the BOX layer of the SOI wafer by RIE. The BOX layer of the SOI wafer holds the suspended proof mass, interdigitated finger triplets, and springs together. With the applied release process the movable structures become free.

The final step uses the advantage of the spray coating. The diluted SHIPLEY S1813 is sprayed on the wafer at a thickness of  $4.5\ \mu\text{m}$ . The spray coating covers the whole wafer, as well as the metal pads on the glass substrate's surface, which are below the  $45\ \mu\text{m}$  deep from the device surface. The final lithography is made with patterning the PR with the release mask. After that, the RIE of the wafer is made and the devices are suspended. Afterwards the wafer is covered with the PR and then diced to separate the dies. The cleaning of the dies follows the subsequent rinse in acetone, IPA, and methanol. The consecutive figures show the process flow of the FD sensor fabrication from Figure 3.5 to Figure 3.16.

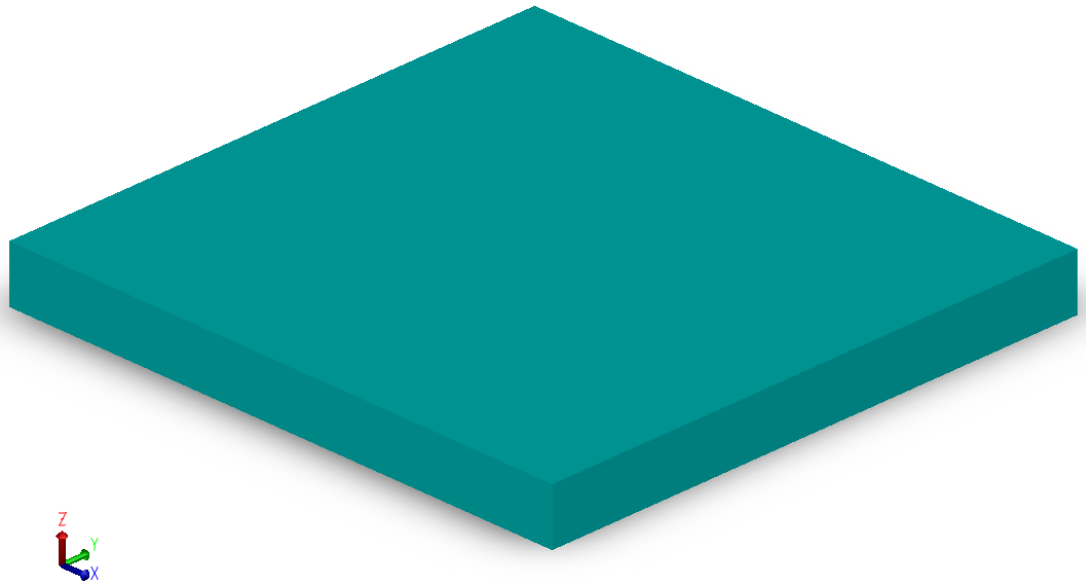


**Figure 3.5:** Substrate is a  $450\ \mu\text{m}$  thick Borosilicate glass wafer.

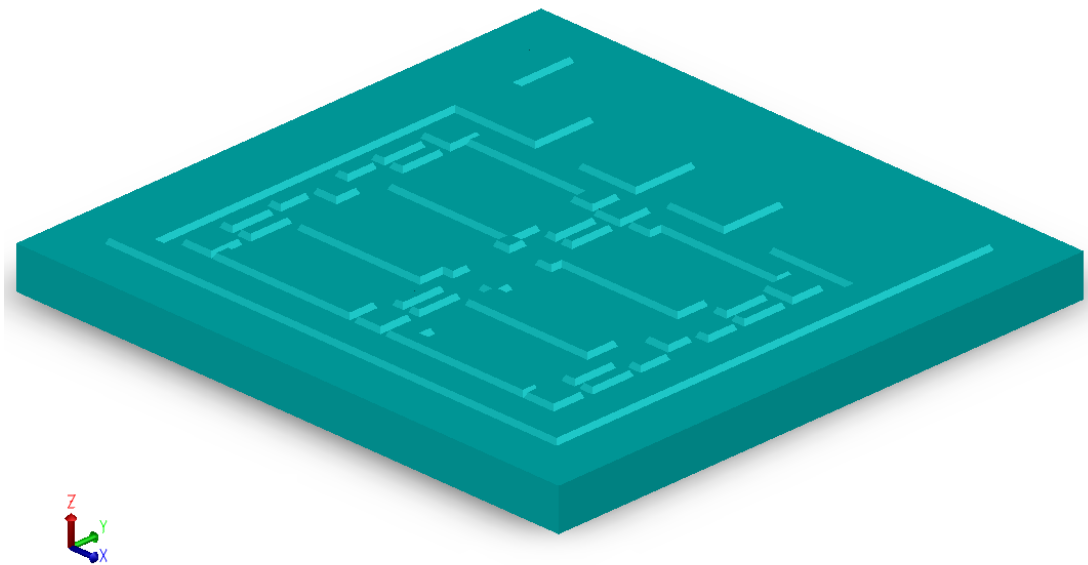


**Figure 3.6:** Formation of the anchors by HF etching.

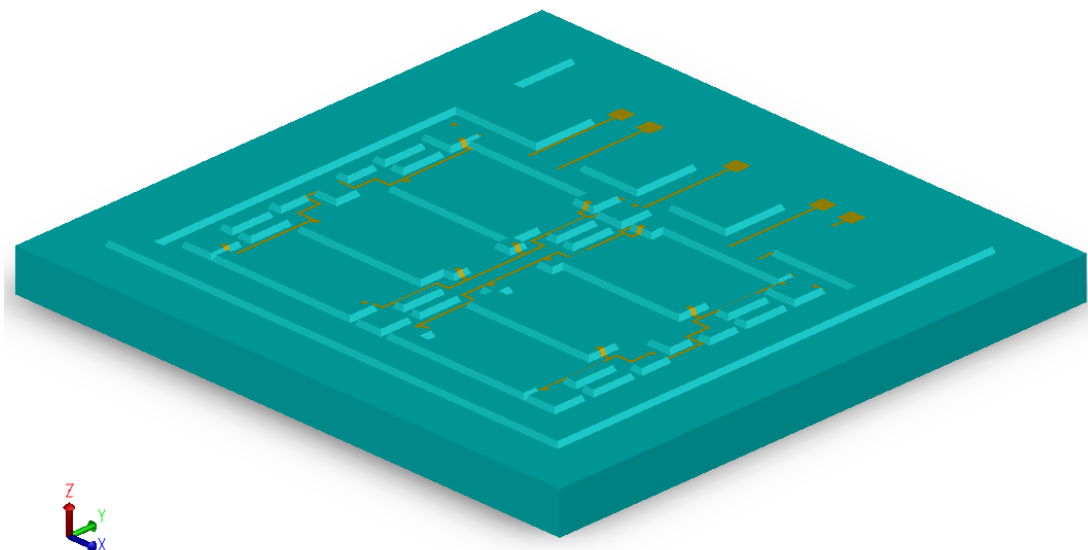


**Figure 3.7:** Patterning the pad metallization by successive Au, Cr, and diffused Au etches.

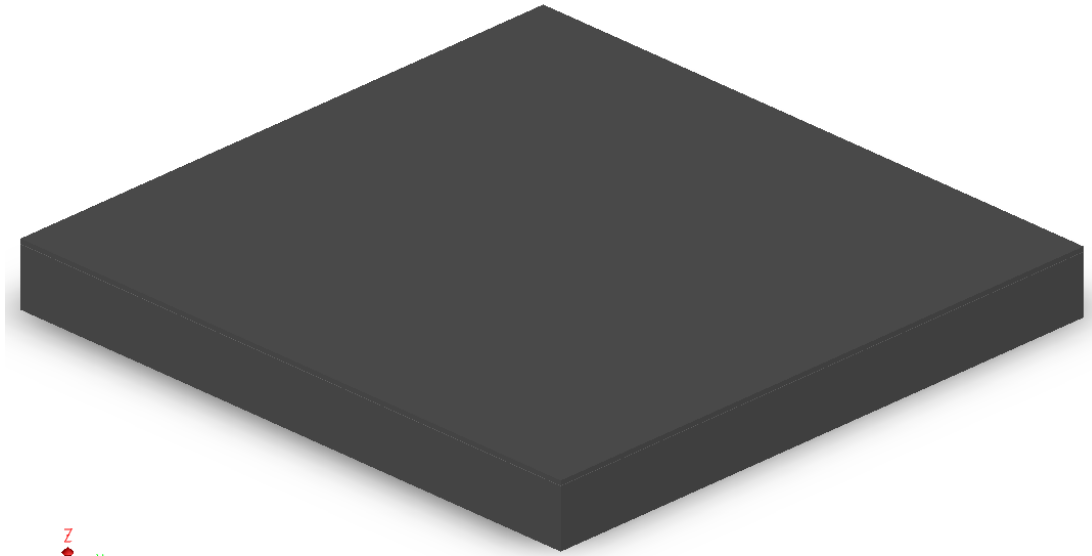


**Figure 3.8:** 35  $\mu\text{m}$  of thick Silicon device layer on top of the 2  $\mu\text{m}$  BOX layer with a supporting 450  $\mu\text{m}$  thick Silicon handle layer forms the SOI wafer.

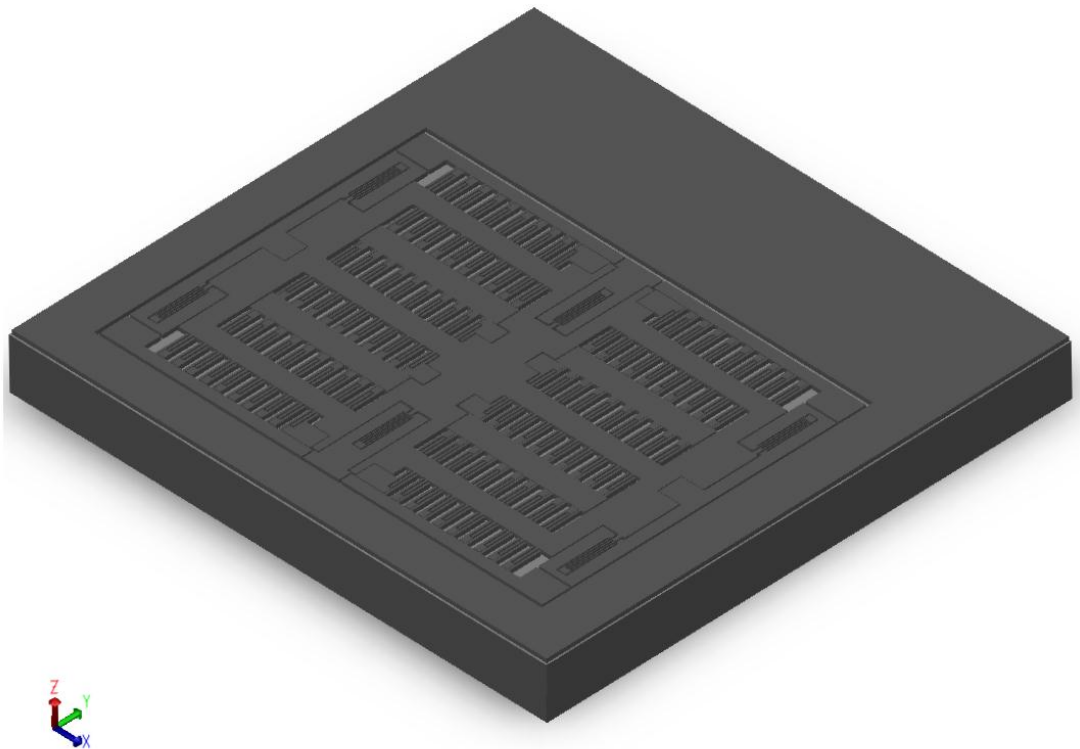


**Figure 3.9:** Defining the structures by DRIE etching of the device Silicon layer.

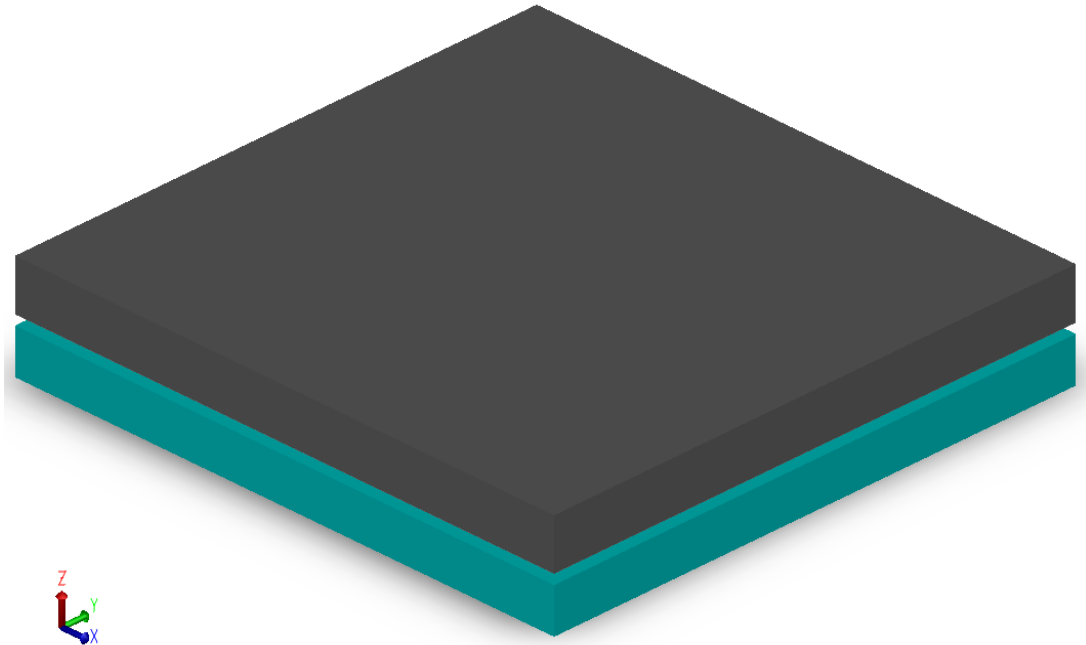


**Figure 3.10:** Bonding of SOI and glass wafers.

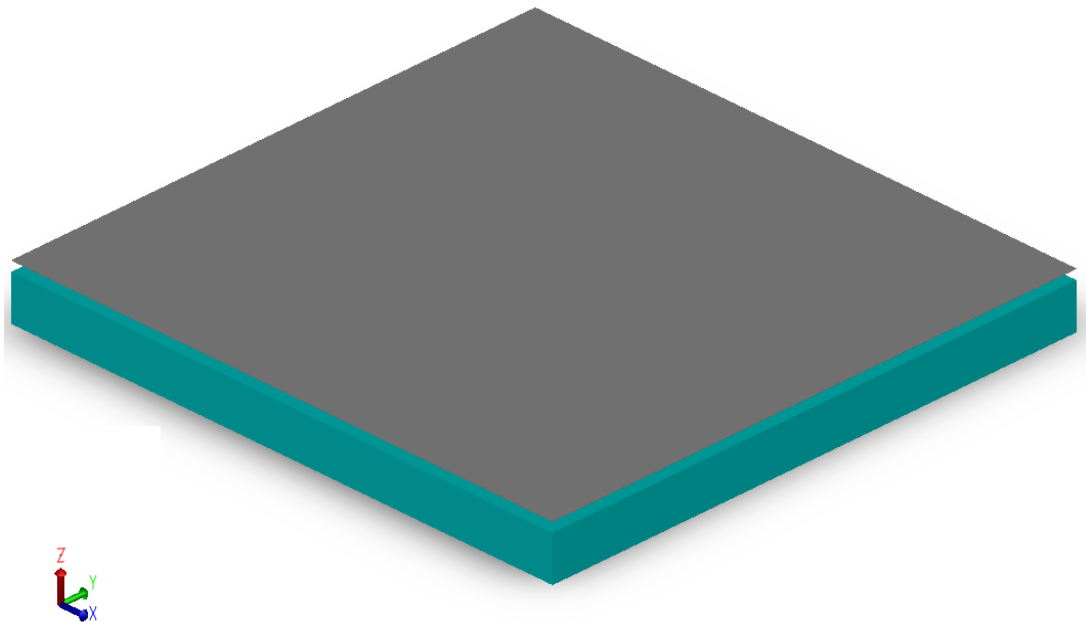


**Figure 3.11:** Removal of the supporting handle Silicon layer by DRIE etching.

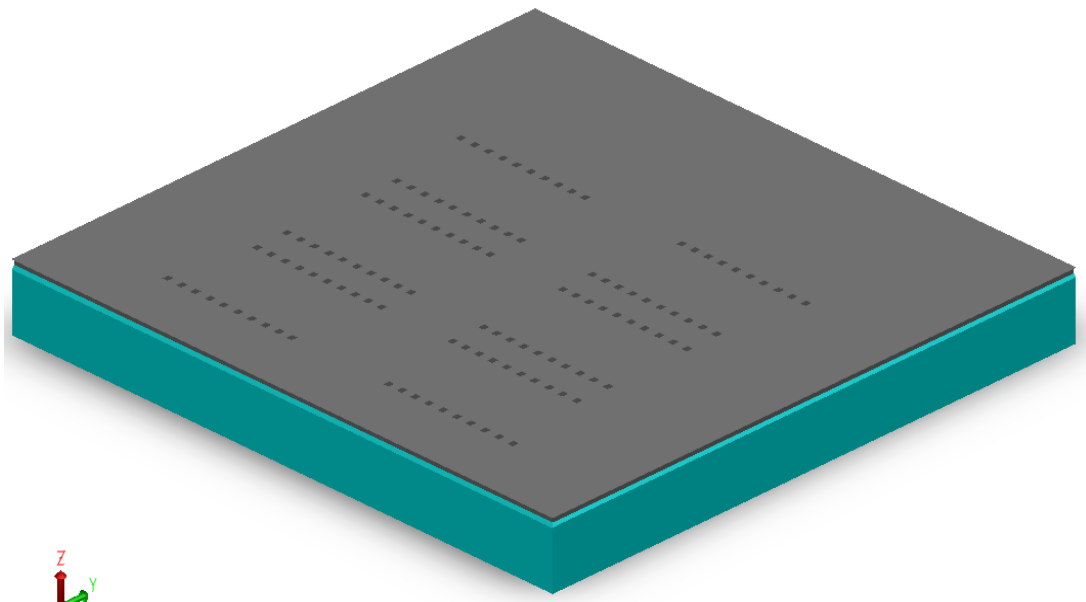


**Figure 3.12:** Formation of vias by RIE.

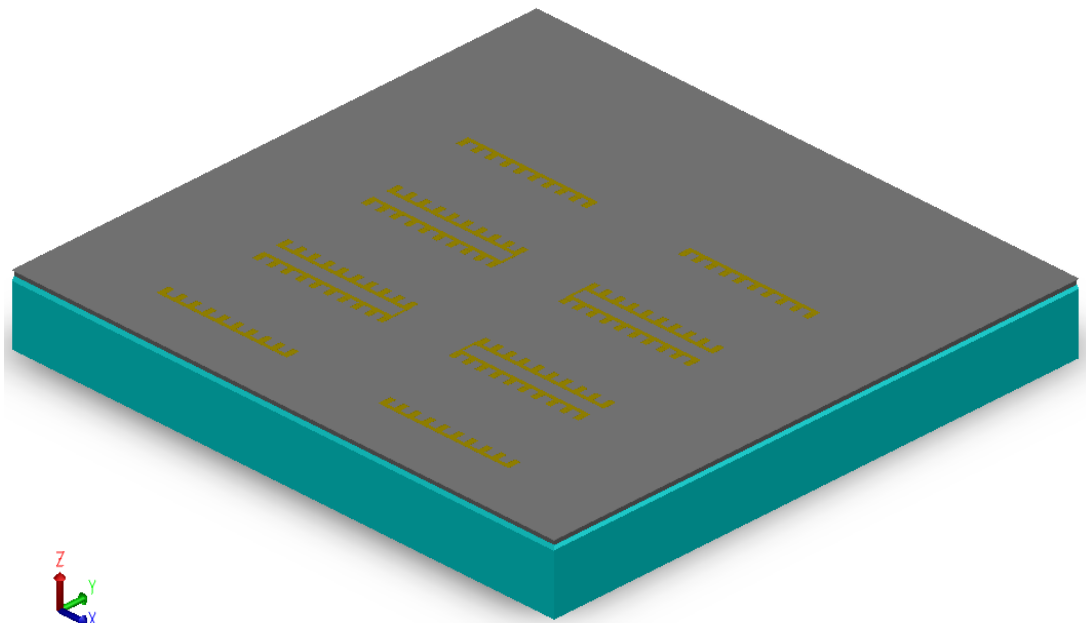


**Figure 3.13:** Patterning the deposited Cr/Au layer.

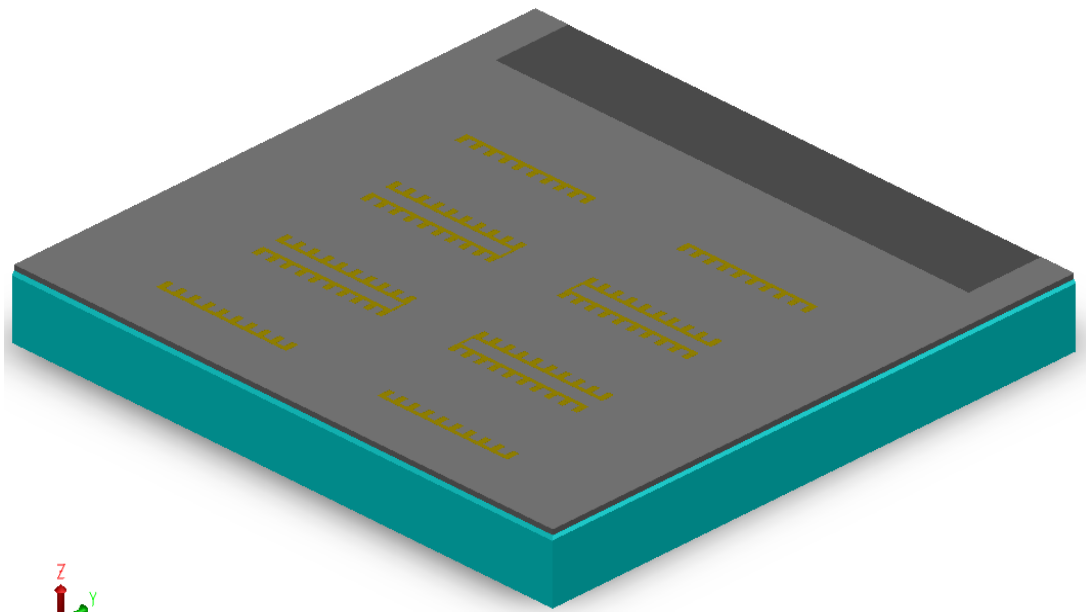


**Figure 3.14:** Reaching out the device Silicon layer by RIE etching of the topmost oxide layers.

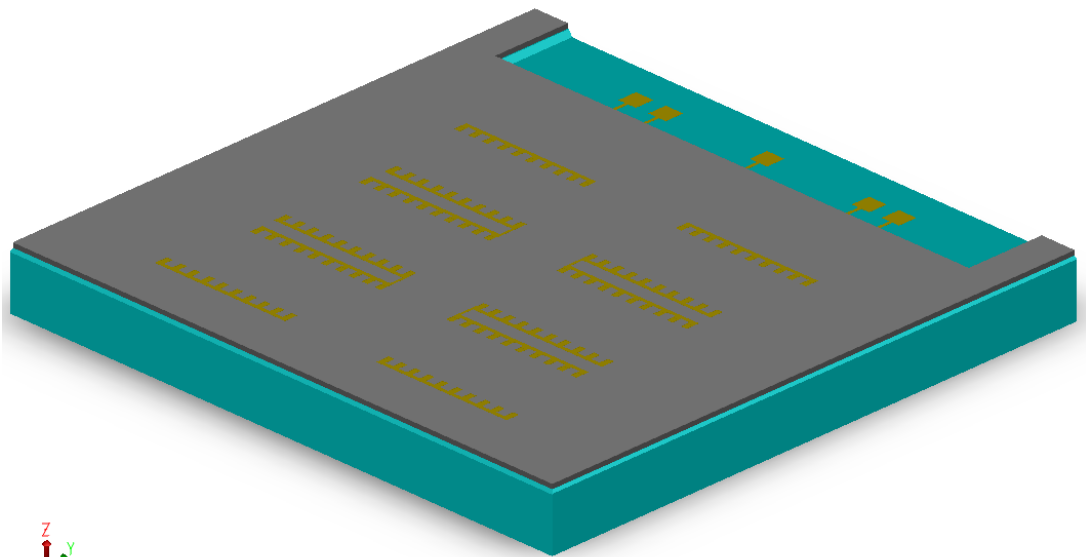


**Figure 3.15:** Uncover of the pads by RIE etching of the device Silicon layer.

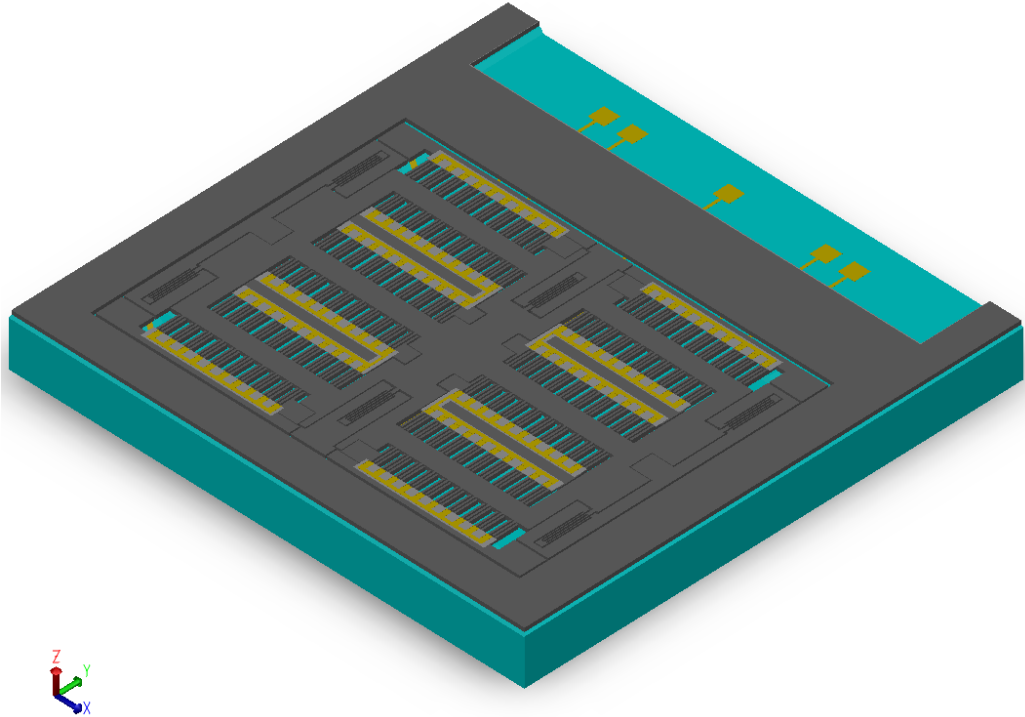


**Figure 3.16:** Release of the devices by RIE etching of the BOX layer.

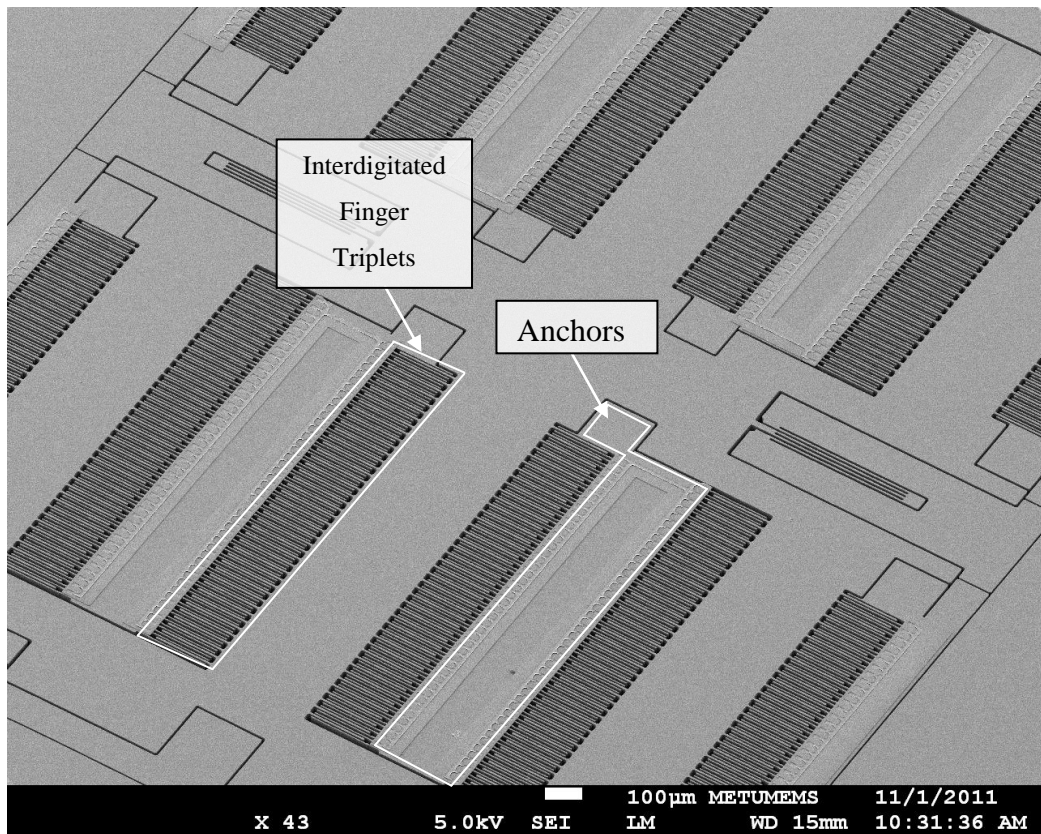


**Figure 3.17:** General view of a fabricated 1<sup>st</sup> generation FD accelerometer die.

### 3.2.5 Problems and Modifications

During the process of the FD sensor fabrication, a number of problems have been encountered. The compressive stress of the BOX layer in the SOI wafer and the unforeseen spark discharge during the anodic bonding necessitates the modifications in the design and process flow. Figure 3.18 and Figure 3.19 show the problems that have been encountered during the fabrication.

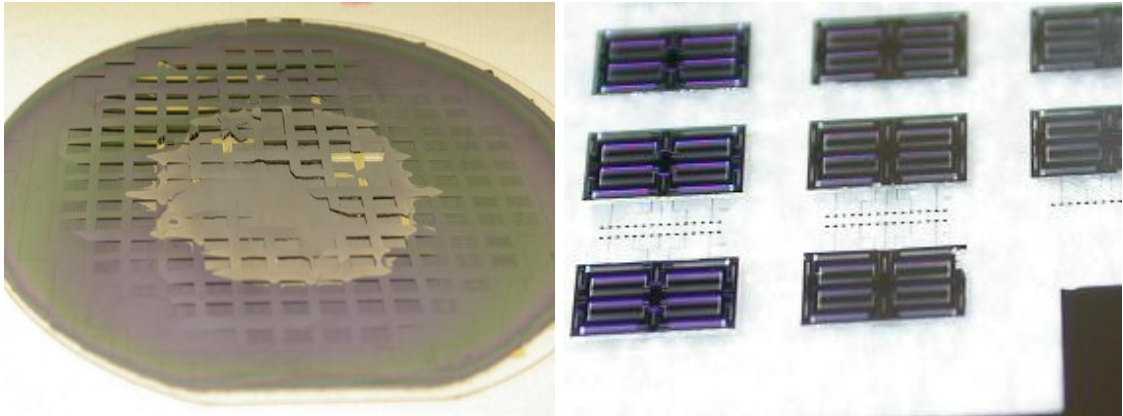


**Figure 3.18:** The compressive stress of the BOX layer results in bursting of the frame.

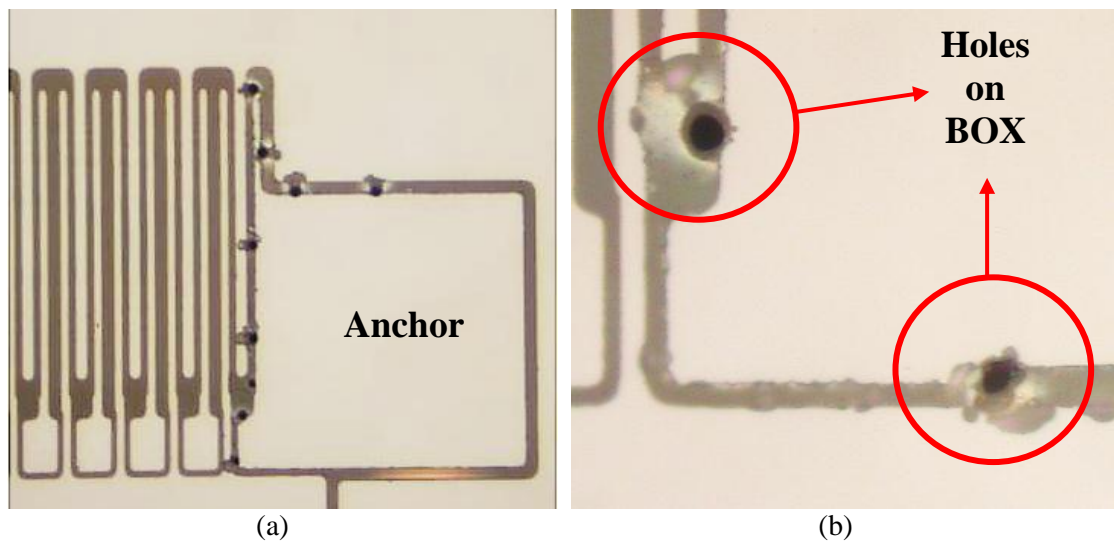


**Figure 3.19:** The accumulated charge on the isolated anchor regions is the reason of the spark discharge, which pierces through the BOX layer.

The problems are solved with the modifications in the mask set. The following sections present those modifications for the mentioned problems.

### 3.2.5.1 Frameless Wafer Process

The SOI wafer fabrication given in Section 3.2.4, results in the release of the suppressed stress of the BOX layer. The stress on the BOX layer shows its strength by bending the frame that encompasses the dies on the wafer. During the removal of the handle layer of the SOI wafer in DRIE etching, the edges of the frame buckles starting from the outer perimeter of the wafer. Eventually, the frame bursts out at the point where the device silicon cannot compete with the stress of the BOX layer before the etching of the handle silicon layer is completed. Figure 3.20 shows the damages formed around a die. Figure 3.21 shows a frame successfully taken out during the thinning of the handle layer by DRIE, and compares it with itself after the BHF etching of the BOX layer.

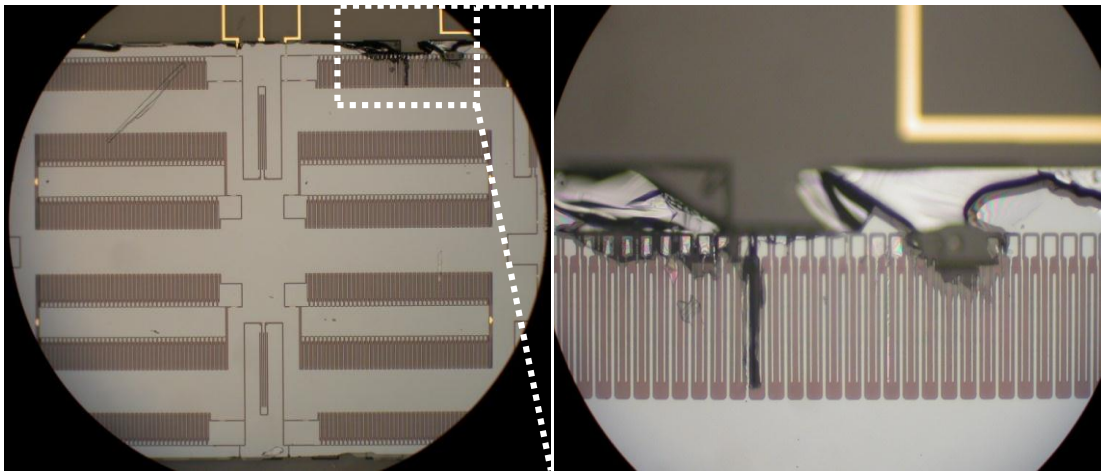


**Figure 3.20:** Burst out of silicon frame results in severe damage to the devices.

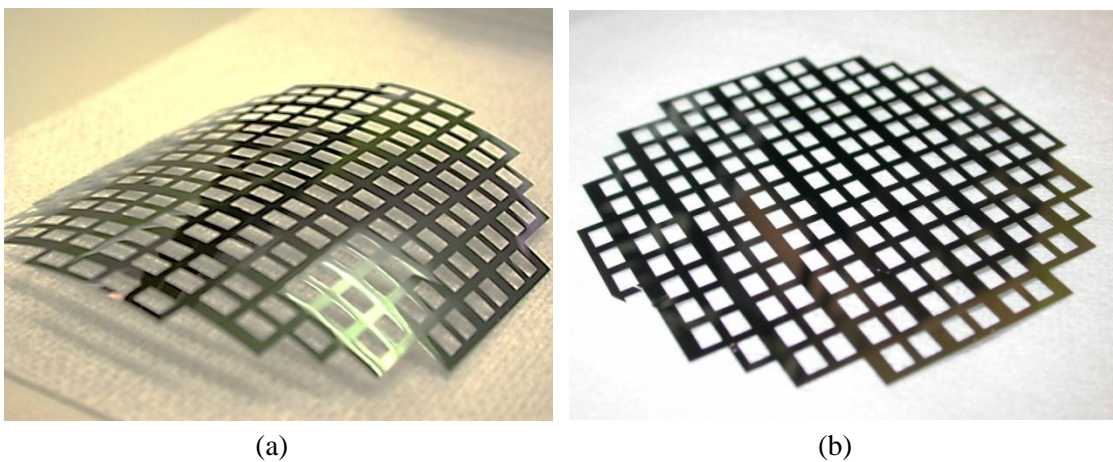


**Figure 3.21:** (a) Stress on the BOX layer buckles the Silicon frame, and (b) the frame is flattened after the BHF.

The stress problem of the BOX layer can be solved with two approaches: 1) Removal of the frame without damaging the devices, and 2) bonding the frame to the glass substrate together with the device silicon. The investigation of the first solution starts with increasing the number of the support arms around the frame, where initially two support arms exists. The support arms are thought to be standing up against the stress of the BOX layer during the fabrication period and provide easy disassembly after the fabrication. In order to find the exact number of support arms successive simulations are carried out in CoventorWARE; however, it turns out that the stress developed at the attachment areas requires many support arms in order to be relieved. Figure 3.22 shows the support arm simulation carried out, during the investigation.

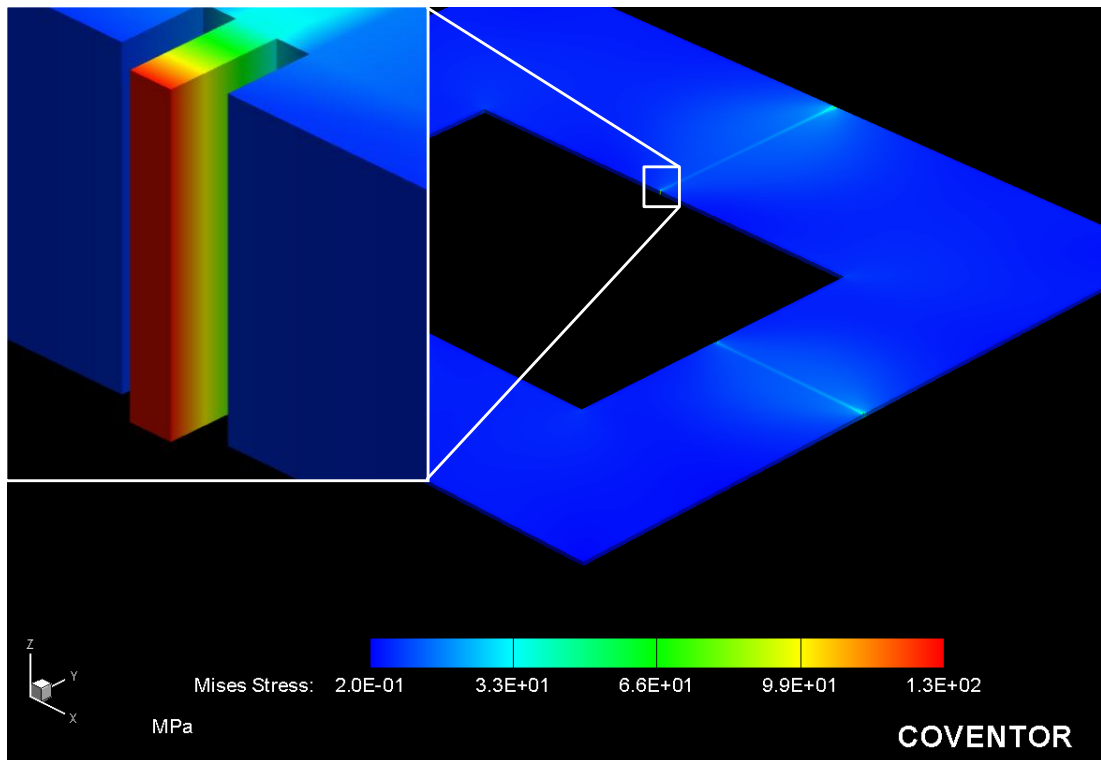


**Figure 3.22:** All of the stress accumulates at the ends of the springs, where they are attached to the sensor.

The investigation of the solution with increased number of support arms around the devices shows that the effort of optimizing the support arm is time consuming, and requires spending excess material source. Therefore, the second choice is preferred in order to complete the process because of its applicability. It only requires addition

of one more mask to the process, which is the pad window mask. In consequence the frame is anodically bonded to the glass substrate with the device Silicon layer in order to increase device Silicon layer's endurance to the innate stress of the BOX layer. Figure 3.23 shows the modification on the initial glass mask, which is used to define the anchor areas. In the second mask, the area below the frame is protected against HF etching of the anchor formation process.

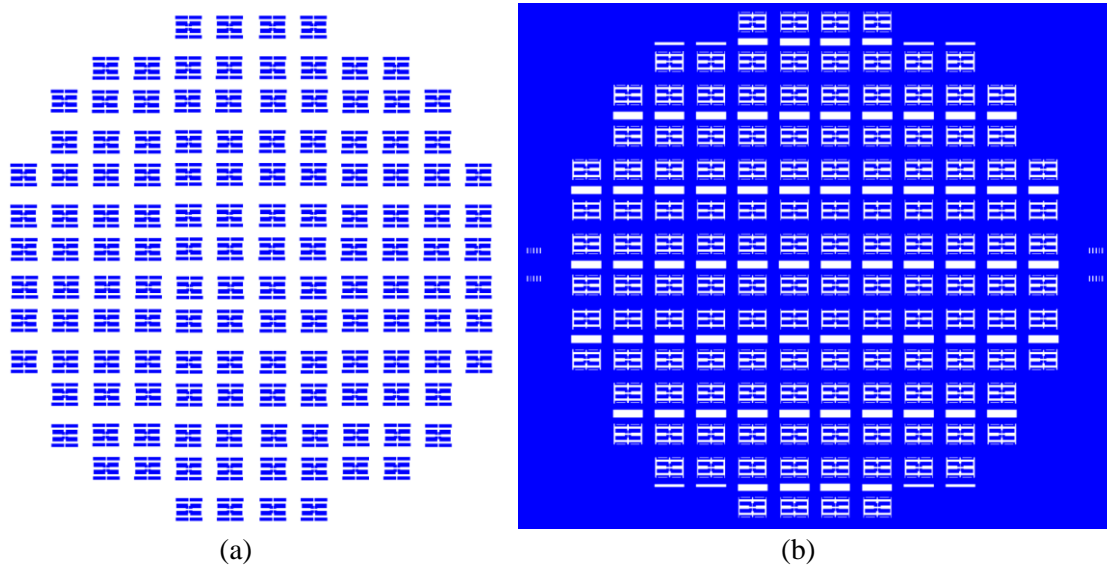


**Figure 3.23:** (a) Normal mask without short metals, and (b) mask with short metals allowing the distribution of accumulated charges equally around the wafer.

### 3.2.5.2 Shorting the Pad Metallization Mask

Holes having diameters of at most 6-7  $\mu\text{m}$  on the BOX layer is observed, after the removal of the handle Silicon layer. The presence of the holes decreases the yield by damaging the devices. The etchants leak into the devices through the holes and cannot get out till the end of the process. During the processes under the vacuum, the leaked fluids puncture the BOX layer more putting the whole wafer at risk. Figure 3.24 shows the fluids leaked inside the device and their consequences.

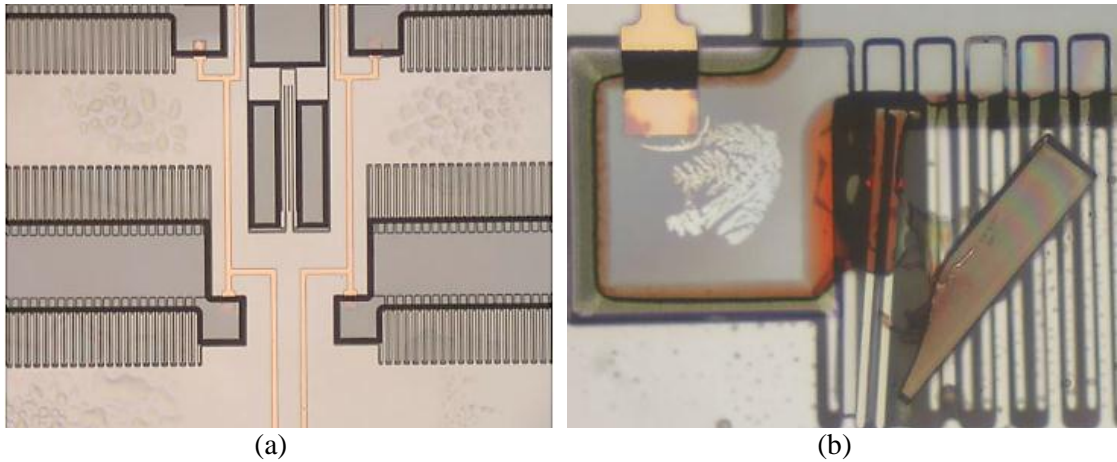


**Figure 3.24:** (a) The fluids leak into devices through the holes, and (b) damage the structure from inside.

The reason of the formation of holes is the discharge of sparks between the anchor points and the handle layer. The charge accumulation at the anchors results in the spark discharge at the anodic bonding. The solution of the problem is distributing the charges on the wafer equally. Therefore, the interconnect metallization climbing over the anchors are shorted on the pad metal mask around the devices. The proposed solution solves the problem and completes a missing point in the anodic bonding of SOI and glass wafers. Figure 3.25 shows the top metal mask and its shorted version together.

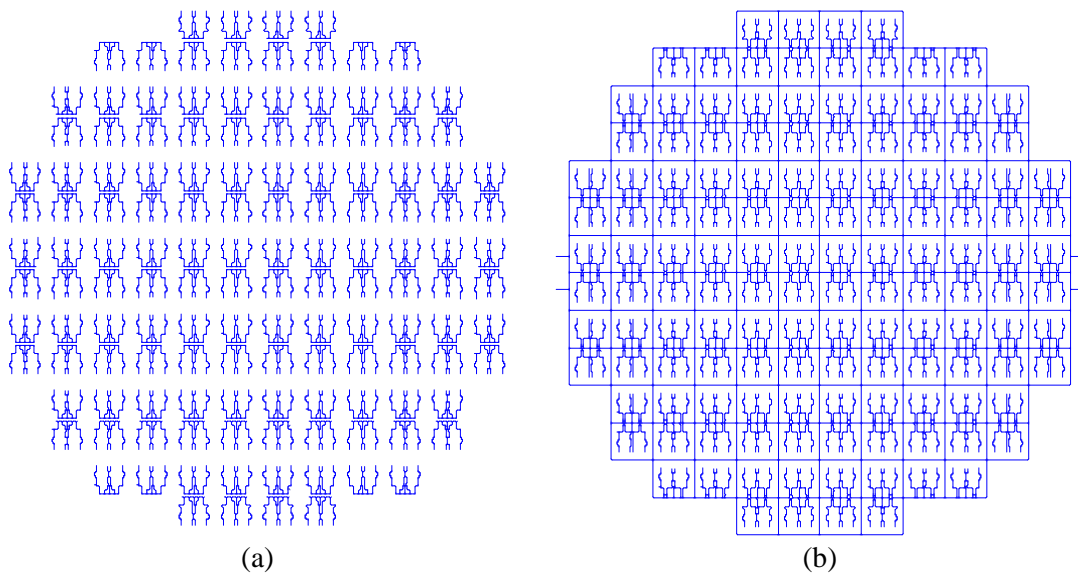


**Figure 3.25:** (a) Normal mask without short metals, and (b) mask with short metals allowing the distribution of accumulated charges equally around the wafer.

### 3.3 Fabrication Results

The evaluation of the fabrication is essential for proper calculation of the performance parameters. The performance parameters are recalculated taking the measurements made on the SEM images into consideration. The SEM images show that the exact lengths of the spaces between the structures after the fabrication. The difference between the designed values in Section 2.3 and post-fabrication values are based on some factors including the minimum feature size in the mask, PR exposure time, and DRIE etching. The each factor requires optimization; but the most dominating one among them is the undercut occurred during the DRIE etching. The undercut widens the gaps between the sensor fingers and shrinks the widths of the spring arms. The increased gap size decreases the capacitance sensitivity as well as the scale factor formulated in Table 2.2, and the shrunken widths of the spring arms decrease the spring constant, which decreases the open-loop gain of the accelerometer and resonance frequency of the sensor. Figure 3.26 shows the illustration of the DRIE undercut.

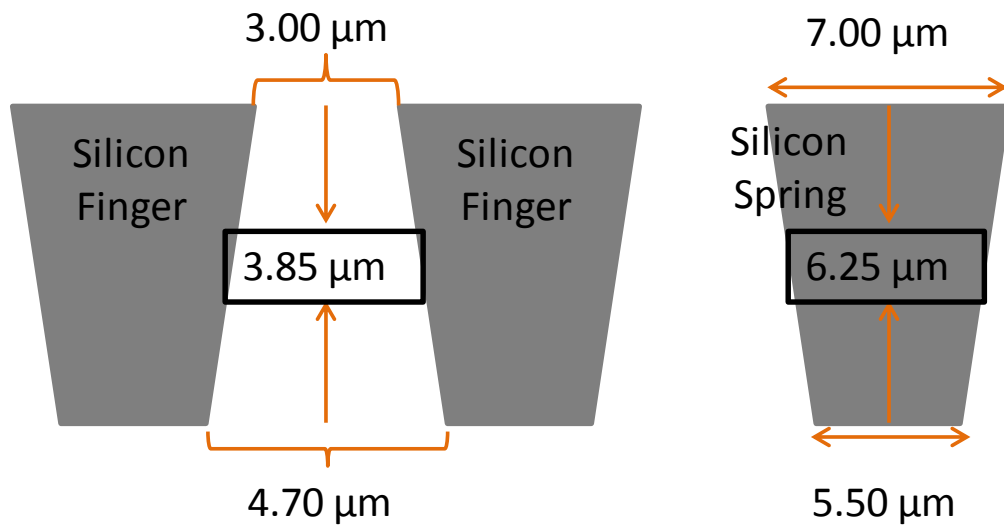
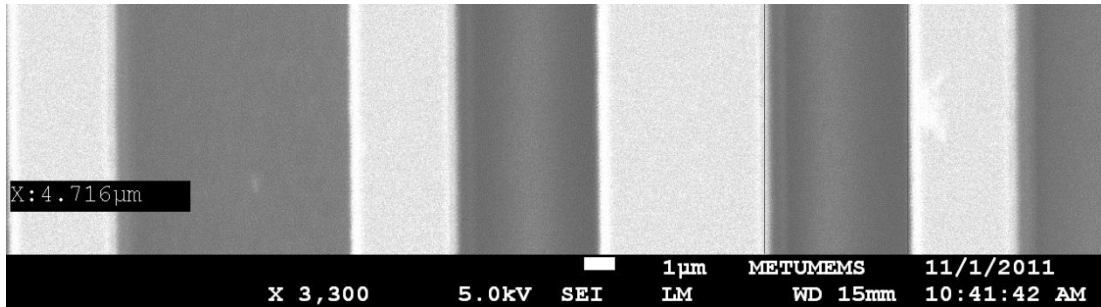
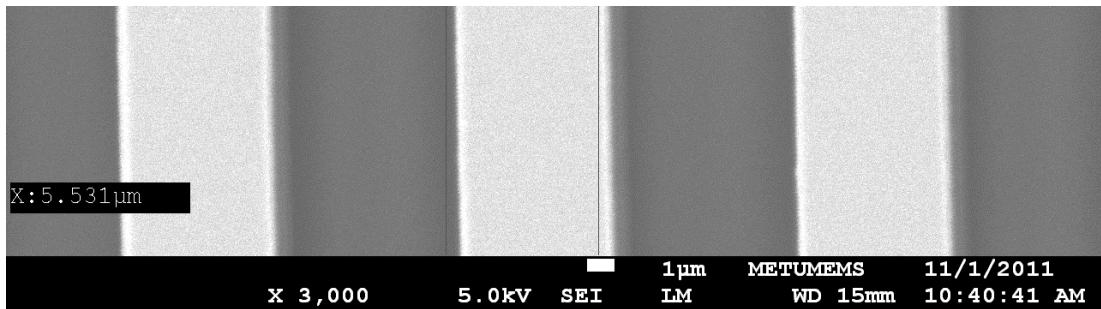


**Figure 3.26:** The DRIE undercut results in widening of the gaps and shrinking of the widths of spring arms.

The inspection on the sensors is made by a Scanning Electron Microscope (SEM). The gaps and widths are measured only for the 1<sup>st</sup> generation devices. It has been found that the gaps widen to 4.716 μm and the widths shrink to 5.531 μm. Figure 3.27 shows the measurements of finger gaps and springs widths.



(a)



(b)

**Figure 3.27:** (a) The measured finger gap is  $4.716 \mu\text{m}$ , and (b) width of the spring arm is  $5.531 \mu\text{m}$ , which are smaller than the expected design values due to DRIE undercut.

In order to visualize the difference before and after the fabrication a comparison is put through. Table 3.2 and Table 3.3 compare the performance parameters of 1<sup>st</sup> and 2<sup>nd</sup> generation sensors before and after the fabrication.

**Table 3.2:** Comparison of the performance parameters before and after the fabrication for the 1<sup>st</sup> generation sensor.

Performance Parameters of 1 <sup>st</sup> Gen. Sensor (before/after the fabrication)			
<b>Gap Distance</b>	3.00/3.85 $\mu\text{m}$	<b>Nominal Capacitance</b>	4.4/3.5 pF
<b>Spring Width</b>	7.00/6.25 $\mu\text{m}$	<b>Capacitance Change @1V</b>	4.4/2.3 fF
<b>Spring Constant</b>	214/148 N/m	<b>Operation Range (9.3 V)</b>	$\pm 8.1/4.9$ G
<b>Quality Factor</b>	4.5/8.9	<b>Damping Coefficient</b>	$2.0/1.0 \times 10^{-3}$ Kg/s
<b>Resonance Frequency</b>	3776/3135 Hz	<b>Brownian Noise</b>	1.7/1.1 $\mu\text{g}/\sqrt{\text{Hz}}$

**Table 3.3:** Comparison of the performance parameters before and after the fabrication for the 2<sup>nd</sup> generation sensor.

<b>Performance Parameters of 2<sup>nd</sup> Gen. Sensor (before/after the fabrication)</b>			
<b>Gap Distance</b>	1.80/2.30 $\mu\text{m}$	<b>Nominal Capacitance</b>	10.5/8.1 $\text{pF}$
<b>Spring Width</b>	4.70/4.40 $\mu\text{m}$	<b>Capacitance Change @1V</b>	435/178 $\text{fF}$
<b>Spring Constant</b>	45/37 $\text{N/m}$	<b>Operation Range (9.3 V)</b>	$\pm 53.7/33.0$ $\text{G}$
<b>Quality Factor</b>	0.23/0.45	<b>Damping Coefficient</b>	1.4/0.7 $\times 10^{-2} \text{ Kg/s}$
<b>Resonance Frequency</b>	2237/2028 $\text{Hz}$	<b>Brownian Noise</b>	7.2/5.0 $\mu\text{g}/\sqrt{\text{Hz}}$

The comparison indicates that the effect of capacitance change is directly reflected to the operation range and the Brownian noise. The operation ranges of the devices have reduced nearly to the half of the initial calculations. Also, the damping is reduced to its half due to the widening of the finger gap. Since, the noise is proportional with damping's root-square; the reduction in noise will be smaller than the reduction in the range. Therefore the resulting dynamic range of the sensors will be smaller than the calculated results.

In yield of view, the similar working sensors with a high yield are not obtained at the end of the fabrication for both generations. The large number of the sensors increases the occurrences of process faults during the fabrication. The faults that have been encountered can be listed as deformations on contact areas, finger ruptures, PR masking of Si during the device layer etching, and stiction of fingers to each other due to polymer or PR residues. Figure 3.28 shows the faults that make sensors inoperable.

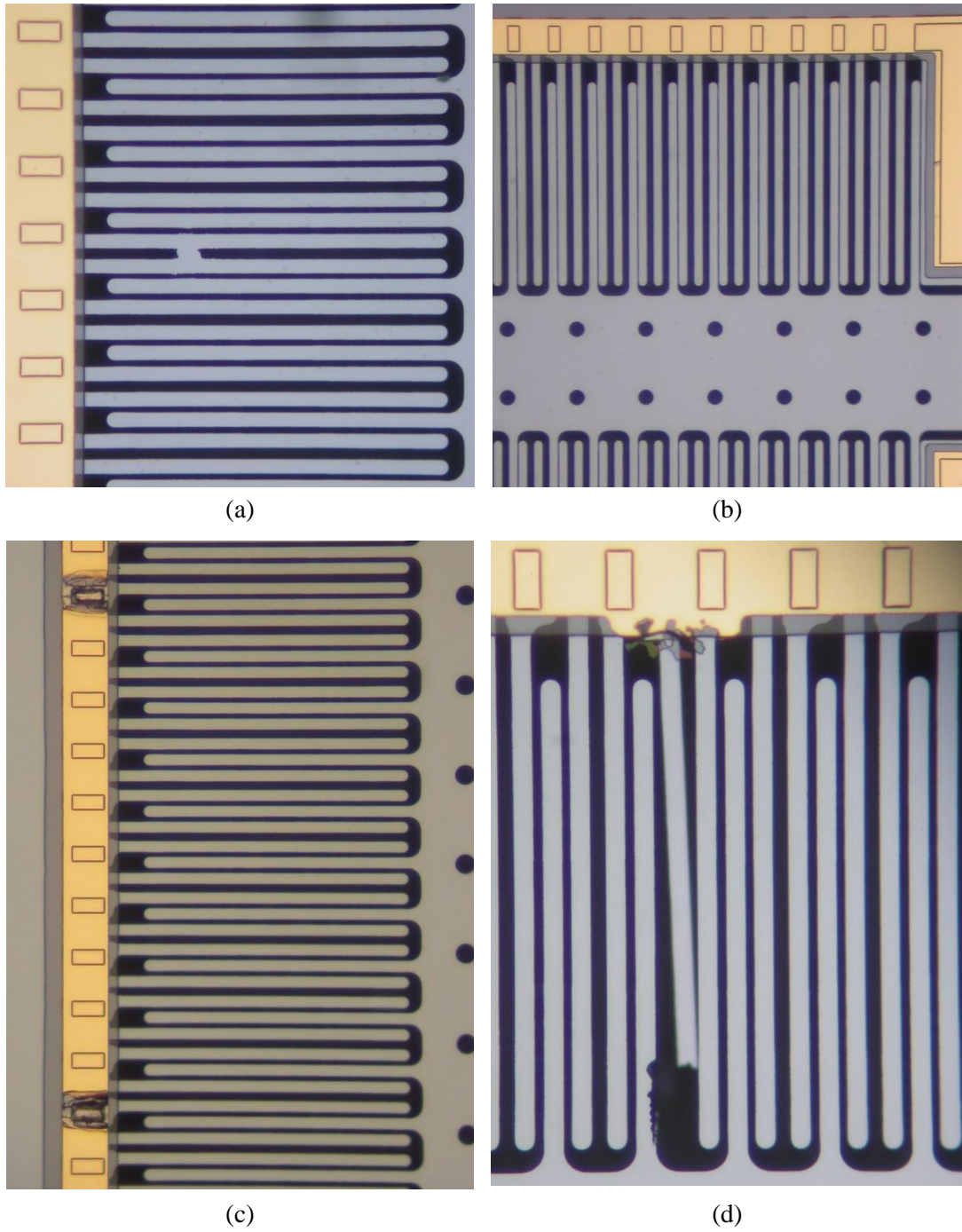


**Figure 3.28:** The faults occurred during the fabrication are (a) PR masking of Si during the device layer etching, (b) stiction of fingers to each other due to polymer or PR residues, (c) deformations on contact areas, and (d) finger ruptures.

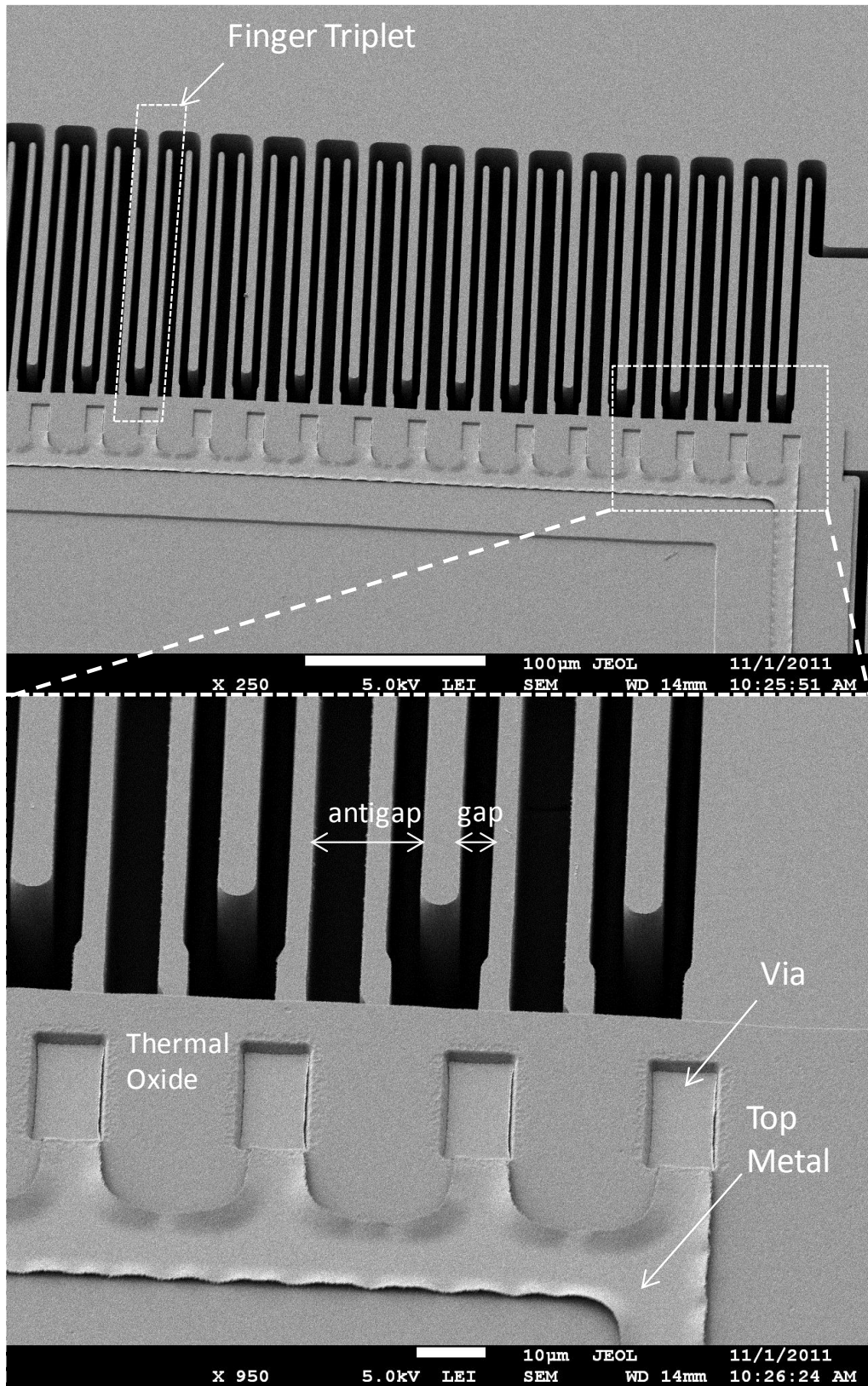


**Figure 3.29:** The top view taken from a fabricated fully-differential accelerometer die. The gaps are wider than the designed value, and edges of the top metal lines are detached due to final release.

### **3.4 Summary of the Chapter**

This chapter presented the fabrication of the designs with the proposed method at Chapter 2. The fabrication methods include basic Silicon and Glass wafer processes, as well as new on-oxide processes in optimized status. Moreover, the chapter includes solutions to frame buckling, and more importantly the specific spark discharge phenomena during SOI and glass anodic bonding, completing the work [54] that describes the SOI and glass anodic bonding mechanics.

# CHAPTER 4

## TEST RESULTS AND DISCUSSIONS

This chapter presents the test results of the 1<sup>st</sup> and 2<sup>nd</sup> generation sensors fabricated with the processes given in the previous chapter. The tests of the fabricated fully-differential (FD) accelerometer sensors comprise of measurements in both sensor and system level. The sensor level tests measures the operability of the sensor within the estimated performance parameters by voltage excitation and measurement of contact resistances, while the system level test covers the noise and bias drift by static measurements, and also the range and nonlinearity measurements by applying artificial accelerations in a centrifuge device. The results are evaluated and discussed with the characterization of the sensor according to formulations given in Chapter 2.

The chapter begins with a brief introduction of the test environment in Section 4.1, and gives place to C-V curve and contact resistance measurements results at applied voltages.

Section 4.2 introduces the sensor level test environment and shows how the tests are conducted. The sensor is packet with a readout having a full-bridge interface employing on-chip reference capacitors on a glass substrate allowing the connection of the FD sensor with the interface. The packed sensor is subjected to static and dynamic tests in a centrifuge device. The accomplished tests are made to extract the noise, bias drift, nonlinearity, and operation range data of the tested FD accelerometers.

Section 4.3 makes a comparison of the tested sensors with a previous work conducted at MEU-MEMS Center [57]. The compared parameters are design values and measurement results.

Lastly, Section 4.4 draws the summary of the chapter.

#### 4.1 Sensor Level Tests

Sensor level test compromise the capacitance, and contact resistance measurements from the C-V curve measurements of the fabricated 1<sup>st</sup> and 2<sup>nd</sup> generation FD sensors. The test environment of the FD sensors requires a probe station and an impedance analyzer for capacitance and resistance measurements. Figure 4.1 shows the test equipment used in the C-V curve measurements.

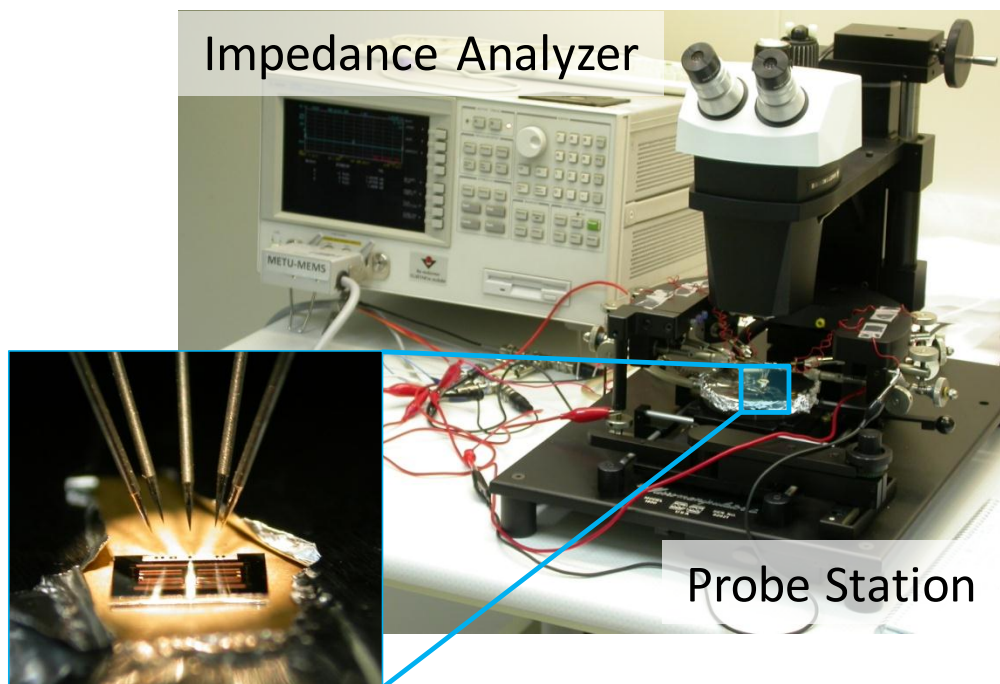


**Figure 4.1:** The Agilent 4294A Impedance Analyzer, and probe station are used for the C-V curve measurements.

The sensor is placed on the probe station, and the pads are grounded except the pad that will be tested. The grounding of the remaining pads eliminates the effects of parasitic capacitances in order to make a correct measurement. The pad, whose capacitance will be measured, is connected to the impedance analyzer in order to make capacitance measurements at different voltage levels. The proof mass is

expected to deflect towards the biased pad as the voltage is increased; therefore the capacitance sensitivity can be extracted out. Figure 4.2 illustrates the configuration of the sensors for the C-V curve measurements.

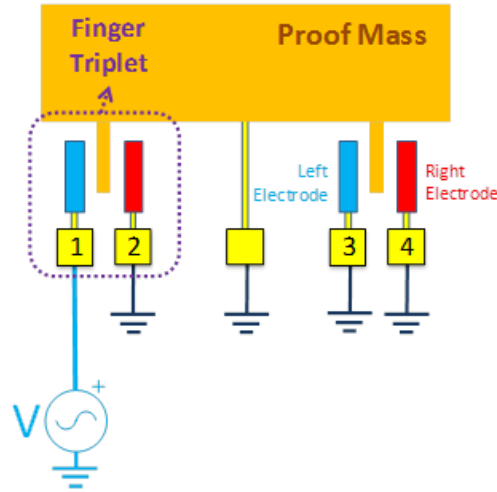


**Figure 4.2:** Test configuration of a FD accelerometer sensor. All of the pads are grounded excepted test pad.

Sensor level tests include nominal capacitance measurements and capacitance change under the applied voltages. Also contact resistance measurements are made during the C-V curve tests. All of the measurement results are compared with the recalculated performance parameters according to the fabrication results given in Section 3.3.

#### 4.1.1 1<sup>st</sup> Generation Sensor Tests

In the FD test configuration, the measurements are made at voltage ranges  $\pm 5V$ . In all of the tests, the sensitivities are very close to each other, being around 70 fF. It is expected that the electrodes taking contact from the top metal, which are connected to pads 2 and 3 in the above figure have close nominal capacitances. However, due to the process mismatches the capacitances between the proof mass and electrodes are 3.88 pF, and 4.10 pF for pads 2 and 3, respectively. The other capacitances between the proof mass and electrodes are 4.27 pF, and 4.06 pF for pads 1 and 4, respectively. Figure 4.3 shows the related C-V curve measurement results at  $\pm 5V$  for the examined 1<sup>st</sup> generation sensor.

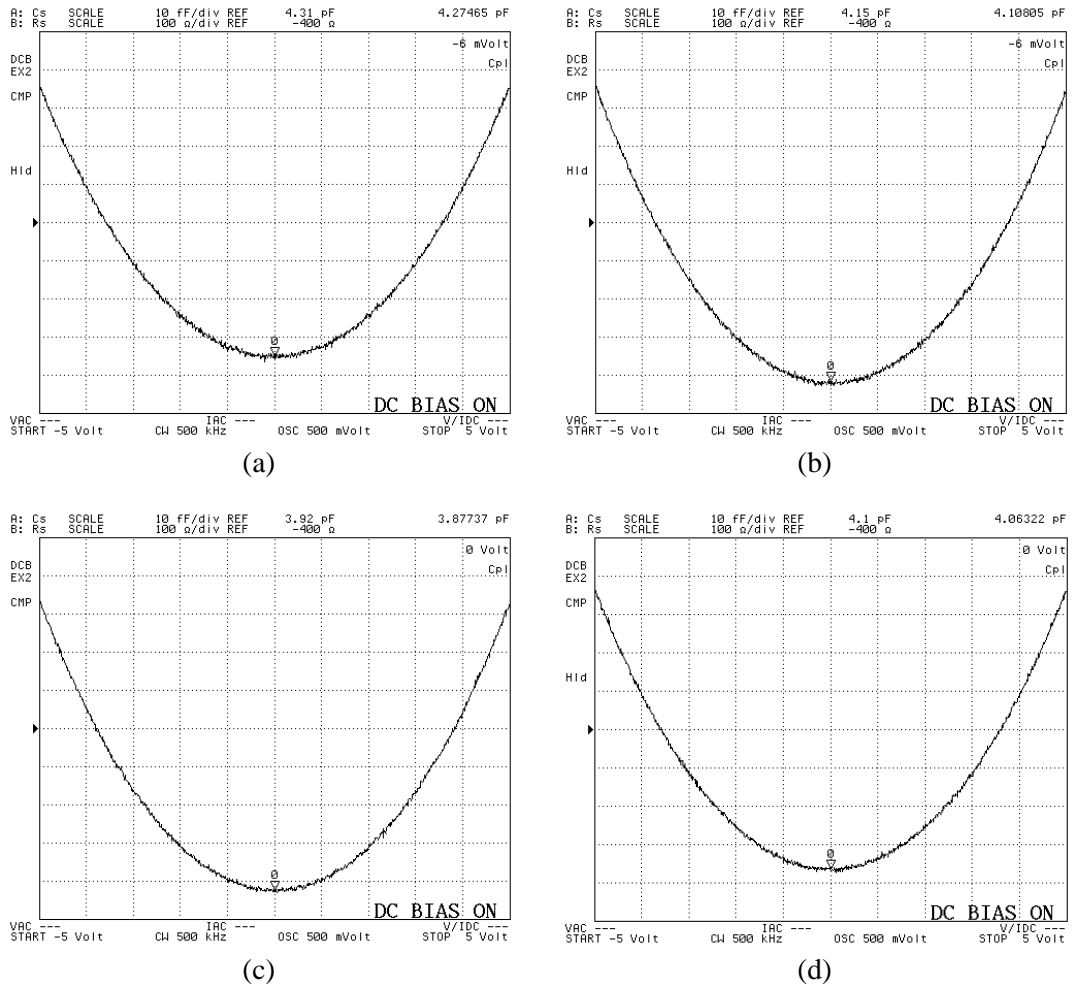


**Figure 4.3:** The measured sensitivities from (a) the first electrode, (b) second electrode, (c) third electrode, and (d) fourth electrode at  $\pm 5$  V.

Based on the above C-V curve measurements, a comparison is made with the calculation results regarding post-fabrication SEM measurements and calculations based on these measurements. In order to make a fair comparison, all of the capacitance changes, are calculated for all voltages up to 5V and the results are compared with the measured capacitance changes. Figure 4.4 shows comparison of the capacitance changes between the calculation and measured results.

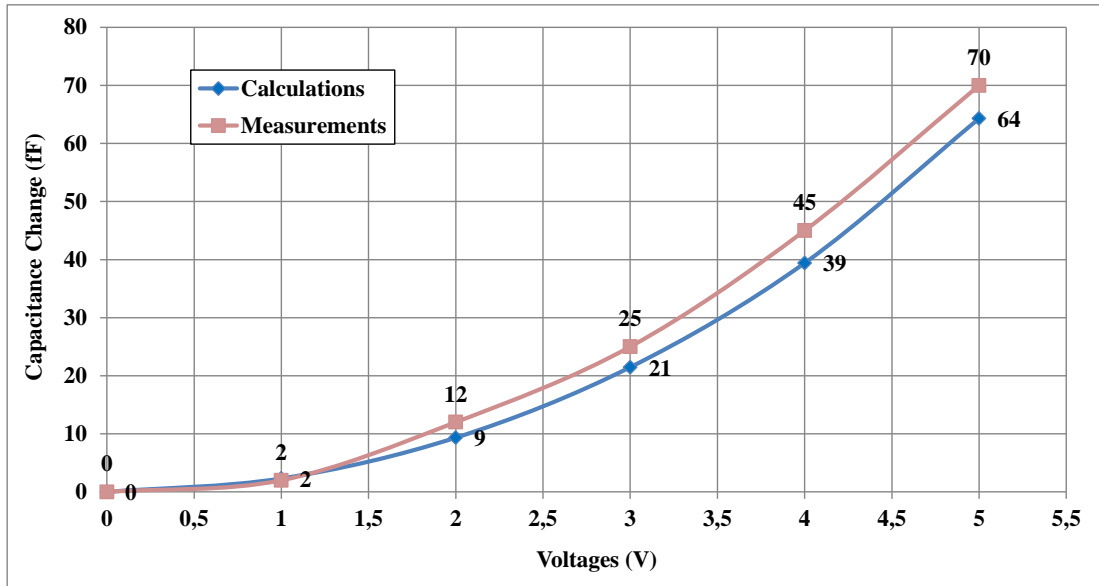


**Figure 4.4:** Measurement results are very close to the calculation results based on the post fabrication SEM measurements.

According to the above figure, the calculations are very close with the measurement results. Even though the voltage is increased, the capacitance difference between the compared data does not diverge. The small divergence between the compared values may arise from incalculable edge and corner capacitances. Although incalculable capacitances cause a problem during the calculations, it is evident that calculation results are pretty accurate with the measurements.

#### 4.1.2 2<sup>nd</sup> Generation Sensor Tests

The tests are conducted as the previous sensor tests. The C-V curve measurements are made, and measurement results are compared with the calculated capacitance changes up to 1V. The measurements made in the range of  $\pm 1$ V due to small pull-in voltage, 1.8V, since the sense electrodes in the 2<sup>nd</sup> generation sensor have smaller gaps and higher number of fingers than that of 1<sup>st</sup> generation sensor. In the tests of 2<sup>nd</sup> generation sensor, the measured capacitances are found to be between 8.0 and 8.5 pF, achieving a capacitance change between 140 and 180 fF, which are close to the calculated results. Figure 4.5 shows the C-V curve measurement results made on pads 1, 2, 3, and 4, respectively. Then, Figure 4.6 gives the comparison results of the calculated and measured results.

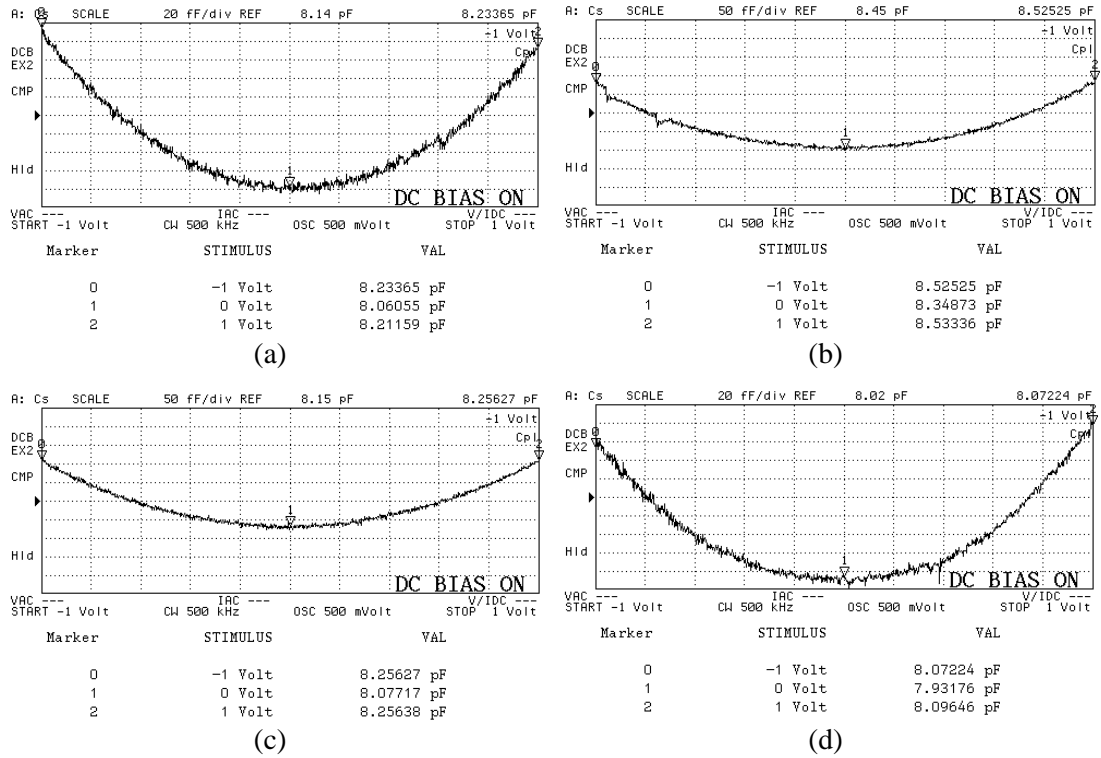


**Figure 4.5:** The measured sensitivities from (a) the first electrode, (b) second electrode, (c) third electrode, and (d) fourth electrode at  $\pm 1$  V.

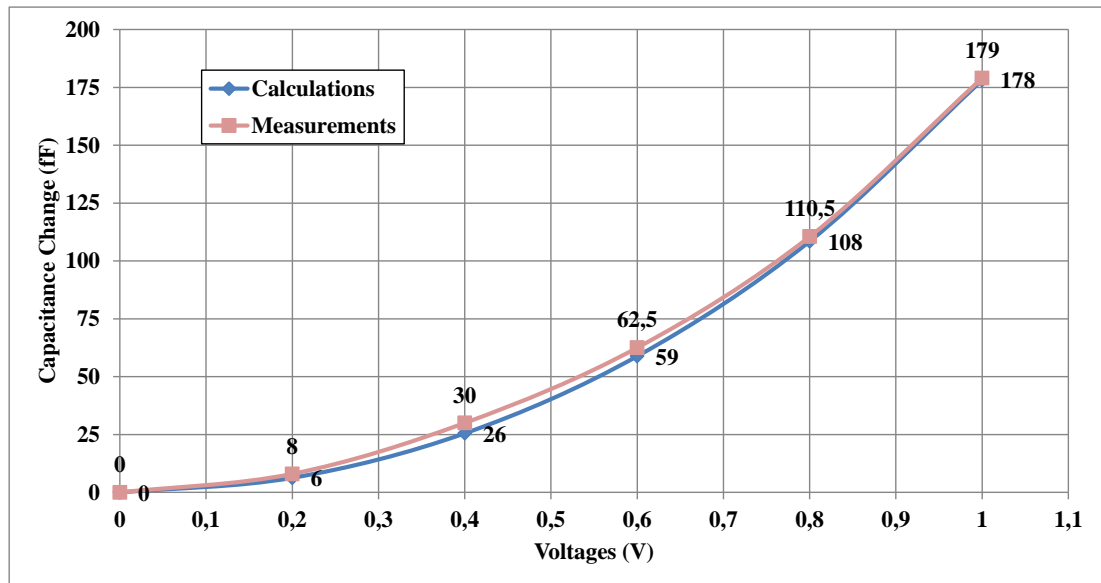


**Figure 4.6:** Measurement results are very close to the calculation results based on the post fabrication SEM measurements. The calculations are made at voltages with 0.2V increments due to low pull-in voltage.

## 4.2 System Level Tests

System level tests determine the performance parameters of the accelerometer with the static and non-static measurements. The static measurements are made for noise and bias drift measurements. The results are extracted from an Allen-Variance plot of the measured data. The non-static measurements are made in order to find the operation range and extract nonlinearity of the sensor utilizing a centrifuge device. Figure 4.7 shows the centrifuge device with accelerometer test setup.

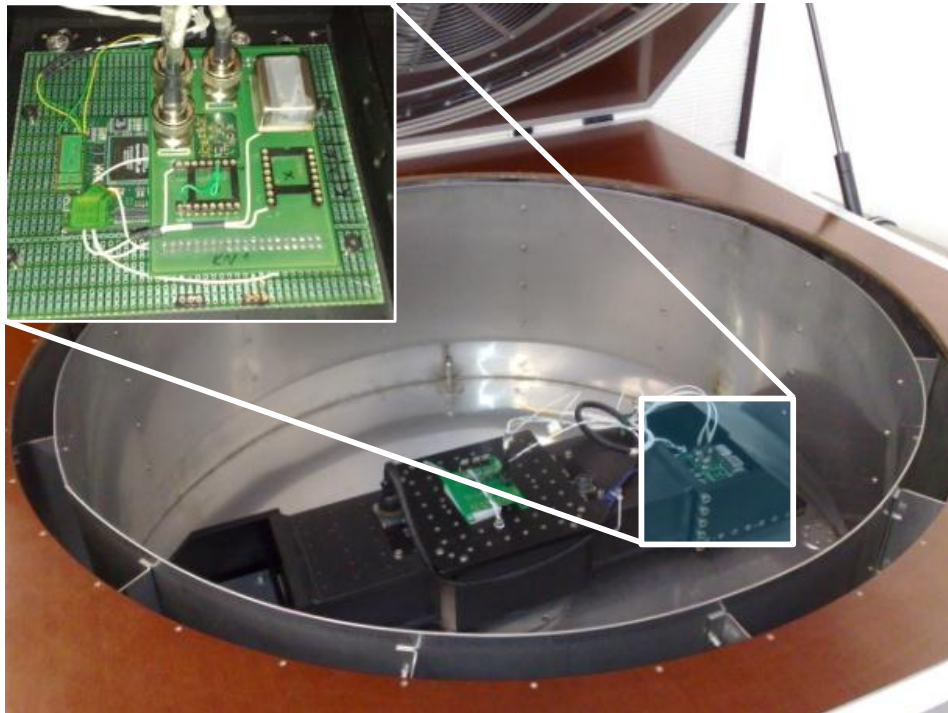


**Figure 4.7:** The accelerometer test setup is mounted on the centrifuge device.

Before the measurements, the sensor and the readout circuitry are packaged together within a 16-pin, where Figure 4.8 shows the sensor's package.

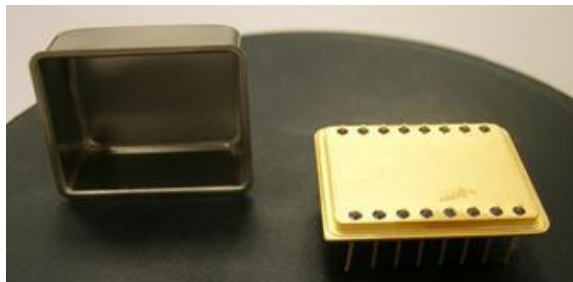


**Figure 4.8:** 16-pin package used for housing the sensor and readout circuitry together.

The packaging process requires a conductive epoxy for installation of the sensor and readout onto a glass substrate. Since the readout of the accelerometer has on-chip reference capacitors, routings on the glass substrate needs to be modified in a way that the full-bridge interface configuration is conserved.

#### 4.2.1 The Glass Substrate

The glass substrate is prepared for testing the sensors with an existing readout circuitry having a FD interface with on-chip reference capacitors. Designing the glass substrate with small parasitic capacitances is the main consideration for the best performance. Therefore, in the implementation of the glass process two fabrication methods are proposed: 1) Two layers of metal separated by a Silicon Nitride insulation layer, and 2) glass substrate with serpentine routings. From the capacitance matrix simulations in CoventerWARE, it has been validated that the first approach presents a high parasitic capacitances due to the thin film Silicon Nitride layer, which also causes the buckling of the wafer. Even the 2  $\mu\text{m}$  thick Nitride layer does not offer small parasitic capacitances that are comparable with the capacitance sensitivities of the sensor. For this reason, the second approach is evaluated, where the routings that have been arranged for equal resistances and close parasitic capacitances, with the parasitic capacitance simulations. Figure 4.9 and Figure 4.10 show the layout of the glass substrate and 3D model of the routings with related capacitances, respectively.

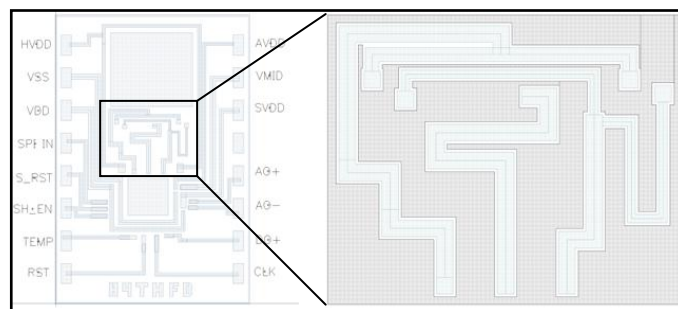


**Figure 4.9:** The layout of the single metal glass substrate with routings.

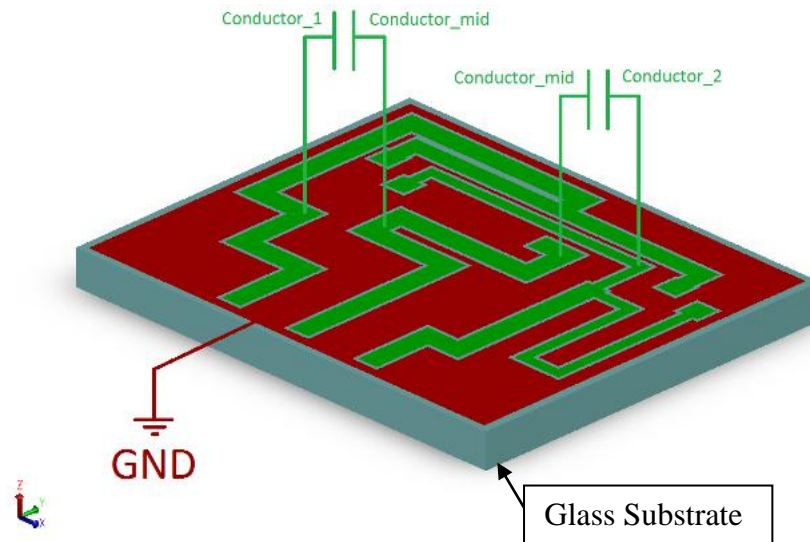


**Figure 4.10:** The 3D model is constructed for the capacitance simulations of the routings by CoventorWARE.

In the above figure, three metal routings are placed on a glass substrate, and the spacing between them is filled with a separate metal plate, GND, which held at zero Volts. The capacitances encapsulated by the GND plane are colored with green, and Table 4.1 gives the capacitance matrix results. The capacitances of side outings with the middle one is highlighted with red color.

**Table 4.1:** Simulation results show capacitances between the routings and the surrounding ground (GND) layer.

Capacitance Matrices (pF)					
Default Mesh Size (5)		Conductor-2	Conductor-1	Conductor_mid	GND
	Conductor-2	0.444	-0.0235	-0.007	-0.413
	Conductor-1	-0.024	0.472	-0.007	-0.442
	Conductor_mid	-0.007	-0.007	0.264	-0.250
	GND	-0.413	-0.442	-0.250	1.104

Unlike the double metal substrate, the parasitic capacitances can be negligible with respect to the capacitances changes of the sensor. Therefore, the proposed glass substrate is suitable for the sensor level tests.

## 4.2.2 Static Measurements

The static measurements include noise and bias drift tests. Employed readout for static measurements has variable integration and on-chip reference capacitors. The tests are conducted with a 1<sup>st</sup> generation sensor and readout having adjusted reference capacitors at 10 pF and 1 pF, respectively. The tests made by acquiring data for 10 min. with a sampling rate of 150 Hz. Figure 4.11 shows the Allan-variance plot of the 10 minutes of static measurement with 10 pF integration and reference capacitors.

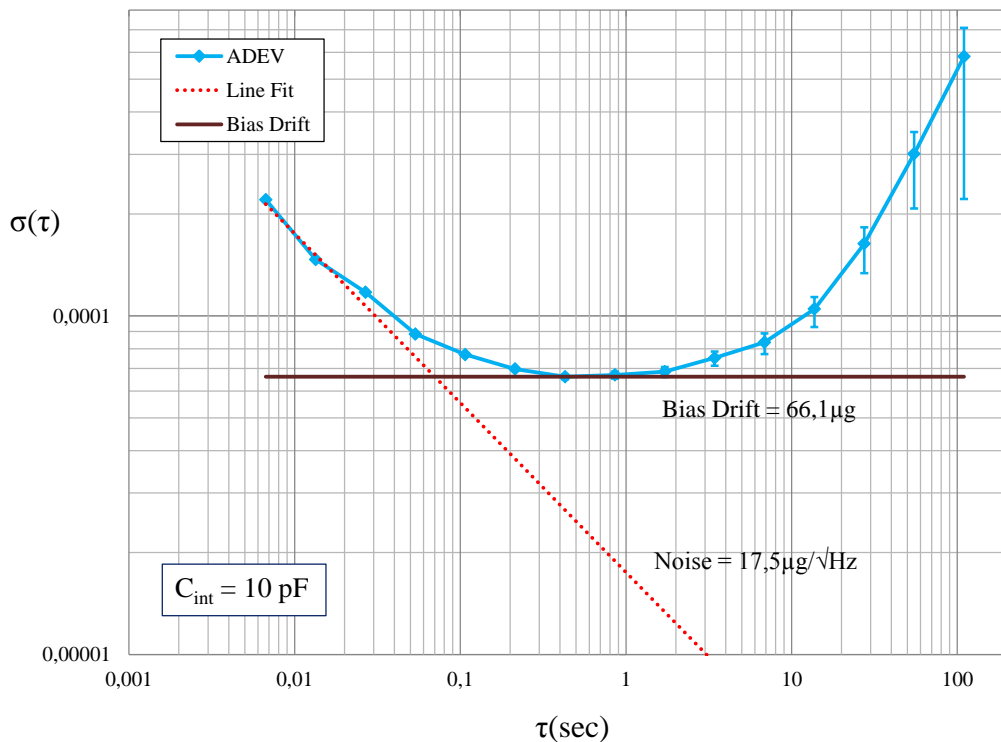


**Figure 4.11:** The Allan-variance plot of the noise data acquired by the static measurements.

Bias drift and noise are deducted from the logarithmic Allan-variance plot of the acquired static measurement data. The slope having a zero aim gives the bias drift and the slope with -1/2 aim gives the noise of the accelerometer system, in other words the velocity random walk. The sensor has bias drift of 66.1  $\mu\text{g}$ , and a noise of 17.5  $\mu\text{g}/\sqrt{\text{Hz}}$ . However, the noise of the system is the RMS value of a double-side banded data, while our data is single-sided due to the measurement made for one axis. Therefore, in order to find the noise floor, which is the RMS noise of the system, the noise is multiplied by  $\sqrt{2}$  according to the standards of IEEE [57]. This

yields a noise floor of  $24.7 \mu\text{g}/\sqrt{\text{Hz}}$ . Multiplication of noise floor with the sampling rate gives the resolution of the overall system, which is  $302.5 \mu\text{g}$ .

### 4.2.3 Dynamic Measurements

The accelerometer is also tested with artificial accelerations up to  $\pm 20 \text{ g}$  values in centrifuge device restricted with  $\pm 35 \text{ g}$  accelerations. The test is important to declare the operation range of the accelerometer and also its linearity. During the tests, effects of integration capacitance are observed by decreasing it from  $10 \text{ pF}$  to  $1 \text{ pF}$ . With the  $10 \text{ pF}$  integration capacitance the accelerometer is found to measure accelerations between  $\pm 20 \text{ g}$ , where the sensor is designed to have an operation range of  $\pm 4.9 \text{ g}$  after the fabrication with  $9.3 \text{ V}$  supply voltage as in Table 3.2. Figure 4.12 shows the nonlinearity measurement with a best curve fit between the calculated operation ranges.

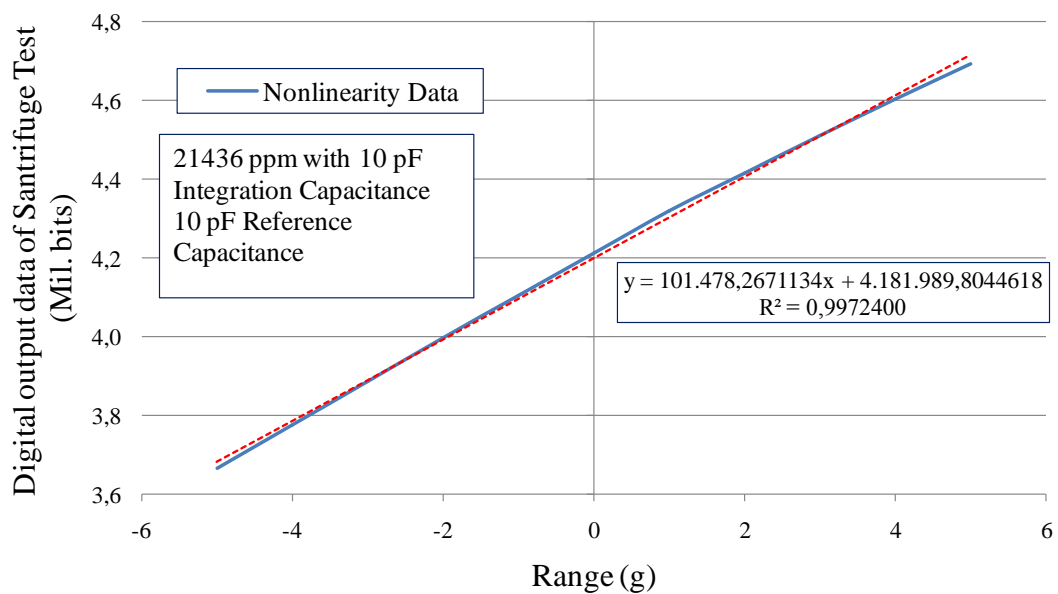


**Figure 4.12:** The nonlinearity of the 1<sup>st</sup> generation sensor is found to be 21.4 kppm between  $\pm 4.9 \text{ g}$  operation-range with  $10 \text{ pF}$  integration capacitances.

The accelerometer is designed to be working in the closed loop; however, due to the small loop gain around 0.2, the accelerometer is operating in the open loop. Therefore, the accelerometer has a nonlinearity of 20.4 kppm. It is expected that the linearity can be improved by increasing the loop-gain of the system. Changing the integration capacitance from  $10 \text{ pF}$  to  $1 \text{ pF}$  is essential for a better nonlinearity. With

increased integration capacitances, the accelerometer could operate in closed-loop, since the loop-gain of the system depends on the integration capacitance. Figure 4.13 shows the improvement in nonlinearity of the accelerometer with 1 pF integration capacitance.

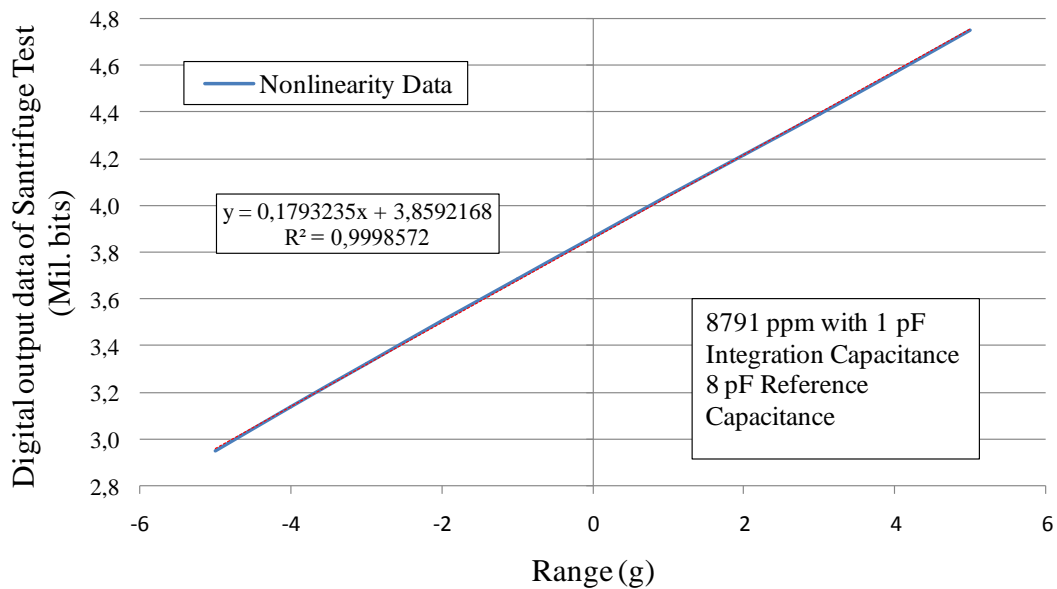


**Figure 4.13:** The nonlinearity of the accelerometer calculated for the range  $\pm 4.9$  g results with a nonlinearity of 8.8 kppm.

It is explicit that reduction of the integration capacitance increased the loop gain of the sensor, and made it operate in the closed-loop. However, the nonlinearity of the sensor is not even close to high performance tactical grade sensors.

### 4.3 Comparison of the Measurement Results

The tests on the fabricated sensors with a readout having on-chip reference capacitors are made. The static and dynamic sensor level tests result with parameters that can be used to evaluate the performance of the fabricated sensors. Evaluation of sensors performance can be made by comparing the results with results of the previous work conducted in METU-MEMS Center. Table 4.2 tabulates the performance parameters of the [57] with the performance parameters of the 1<sup>st</sup> generation sensor. Note that, the readout of the previous work and the accelerometer with 1<sup>st</sup> generation sensor are the same.

**Table 4.2:** Comparison of the measured performance parameters between 1<sup>st</sup> generation sensors with the previous work. (\*with 10pF C<sub>int</sub>, \*\*with 1pF C<sub>int</sub>, \*\*\*calculated value)

<b>Design Parameters</b>	<b>Previous Work [57]</b>	<b>This Work (1<sup>st</sup> gen. sensor)</b>	<b>This Work (2<sup>nd</sup> gen. sensor)</b>
Die Area	$24.7 \times 10^{-6} \mu\text{m}^2$	$25.8 \times 10^{-6} \mu\text{m}^2$	$23.4 \times 10^{-6} \mu\text{m}^2$
Proof Mass	$2.30 \times 10^{-7} \text{Kg}$	$3.80 \times 10^{-7} \text{Kg}$	$2.30 \times 10^{-7} \text{Kg}$
Gap Spacing	2.3 $\mu\text{m}$	3.85 $\mu\text{m}$	2.3 $\mu\text{m}$
Spring Width	6.7 $\mu\text{m}$	6.25 $\mu\text{m}$	4.4 $\mu\text{m}$
Young's Modulus	130 GPa	190 GPa	190 GPa
# of Fingers per Pad	352	256	352
# of Pads	2	4	4
Spring Constant	40 N/m	116 N/m	37 N/m
Damping	$0.9 \times 10^{-2} \text{Kg/s}$	$0.42 \times 10^{-2} \text{Kg/s}$	$6.4 \times 10^{-2} \text{Kg/s}$
Q-factor	0.36	8.9	0.45
Resonance Freq.	2385 Hz	3135 Hz	2028 Hz
Rest Capacitance	10.5 pF	3.5 pF	8.1 pF
Cap. Sensitivity per Pad	75 fF@1V	2.3 fF@1V	178 fF@1V
Noise	4.5 $\mu\text{g}\sqrt{\text{Hz}}$	17.5 $\mu\text{g}\sqrt{\text{Hz}}^*$	6 $\mu\text{g}\sqrt{\text{Hz}}^{***}$
Bias Drift	6.4 $\mu\text{g}^{**}$	66.1 $\mu\text{g}^*$	--
Range	$\pm 35 \text{g}^*$	$\pm 12 \text{g}^*$	$\pm 33 \text{g}^{***}$
Nonlinearity	150 ppm <sup>**</sup>	8791 ppm <sup>**</sup>	--

According to the table, 2<sup>nd</sup> generation sensor provides higher sensitivity than the previous work. The higher sensitivity is achieved with increased number of fingers and canceled anti-gap capacitances by employing interdigitated sense fingers. It is expected that the accelerometer with a 2<sup>nd</sup> generation sensor perform a better performance.

#### **4.4 Summary of the Chapter**

The chapter covered the fabrication and sensor level test results of the designed accelerometer sensor. In that manner, test environment and equipment were presented. C-V curve results of sensors, static and dynamic measurement results of accelerometer were demonstrated. The performance of demonstrated accelerometers was compared with the calculations. It was shown that the calculations were consistent with the measurements. At the end of the chapter, the performance parameters of the fabricated sensor were compared with that of a sensor belonging to a previous work [57] conducted in METU-MEMS Center. The comparison show that the fabricated 1<sup>st</sup> generation sensor lacks behind; but, the 2<sup>nd</sup> generation sensor offered more capacitance sensitivity.

## CHAPTER 5

### CONCLUSIONS AND FUTURE RESEARCH

The implementation of the fully-differential (FD) MEMS capacitive accelerometer, employing interdigitated fingers, was shown for the first time in the literature by utilizing bulk-micromachining technologies on a SOI wafer. The followings conclude the accomplishments carried out during this research:

1. The fabrication process of bulk-micromachined MEMS FD capacitive accelerometer sensor on a SOI wafer employing interdigitated sense fingers was realized. The problems met during the fabrication was identified, which are broken frame due to the oxide's stress during the handle layer removal of the SOI wafer and hole formations on oxide layer due to the spark discharge arisen from charge accumulation on isolated silicon during the anodic bonding. Solution of the problems were investigated and performed. Suppressing the stress of the oxide layer was tried with CoventorWARE simulations employing spring like arms attached to the frame. Many simulations were conducted by increasing the support arms. However, no simple solution was found to disassemble the frame after the fabrication. Therefore, the frame was bonded to the glass substrate. The bonding of the frame introduced one more step to the whole process; therefore mask number was increased one, which was the window opening mask for the contact pads. On the other hand, the reason of the spark discharge problem was identified as the charge accumulation during the anodic bonding of SOI and glass wafers. The discharges happened around the isolated silicon anchors.

Therefore, contact metals climbing the anchors were shorted to each silicon electrode by pad metallization surrounding the wafer. With the modification on the pad metallization mask the problem was solved without any extra mask insertion to the process.

2. The difference between interdigitated sense element and comb type sense element was put forth. It has been shown that interdigitated sense fingers achieves better sensitivity in comparison with comb-finger ones, satisfying a twofold difference at low accelerations. Based on these calculations, two FD sensor design with high sensitive interdigitated fingers were proposed with their modeling, which were verified in CoventorWARE FEM software.
3. The 1<sup>st</sup> generation sensor design aimed low noise with its large proof mass and high yield with 3  $\mu\text{m}$  gap and the 2<sup>nd</sup> generation sensor design aimed high sensitivity were fabricated. The sensor and system level tests of the fabricated sensors were carried out using a readout having fully-differential interface with on chip reference capacitors. The 1<sup>st</sup> generation sensor tests resulted with a noise floor of 24.7  $\mu\text{g}/\sqrt{\text{Hz}}$  and a bias drift of 66.1  $\mu\text{g}$ . During the tests the accelerometer achieved  $\pm 12$  g at closed-loop operation. It has been shown that the linearity of the accelerometer improved with decreasing integration capacitance from 10 pF to 1 pF.

## 5.1 FUTURE RESEARCH

The accelerometer sensor fabrication with seven masks was realized. The one additional mask was required due to the broken frame in handle layer removal step. Processing without frame bonding would decrease the mask number to six, and may increase the yield of the fabrication.

During the tests it was shown that decreasing the integration capacitance decreases the nonlinearity of the accelerometer. However, the nonlinearity was not close to nonlinearity of tactical grade accelerometers. Moreover, noise and bias drift of the accelerometers were larger than expected values. The additional noises were considered to be arisen from de-optimized readout circuitry. Even, the resolution of

the reference capacitors did not match with the sensor's sense capacitances. Therefore, investigation on an optimized readout utilizing a full-bridge interface that excludes the on-chip reference capacitors for the operation was required.

## REFERENCES

- [1] Yole Développement, “Status of the MEMS Industry,” Sept 2011.
- [2] Micronews Magaziene, pp. 4, No: 72, Sept 2008.
- [3] J. Bouchaud, “MEMS Combo Sensors to Deliver Large Revenue Growth Over Five Years,” 14 Dec 2011, <http://www.isuppli.com/MEMS-and-Sensors/MarketWatch/Pages/MEMS-Combo-Sensors-to-Deliver-Large-Revenue-Growth-Over-Five-Years.aspx>, reached on 10.01.2012.
- [4] C. M. Sun, M. H. Tsai, C. Wang, Y. C. Liu, and W. Fang, “Implementation of a Monolithic TPMS using CMOS-MEMS Technique,” *Tech. Dig. 22<sup>th</sup> Int. Conf. Solid-State Sensors and Actuators (Transducers’09)*, pp. 1730-1733, 21-25 June 2009.
- [5] VTI Technologies, “SCC1300 Combined Gyroscope and Accelerometer,” Datasheet, <http://www.vti.fi>, reached on 10.01.2012.
- [7] S. Jean-Michel, “Market Opportunities for Advanced MEMS Accelerometers and Overview of Actual Capabilities vs. Required Specifications,” *Position Location and Navigation Symposium*, 2004. PLANS 2004, pp. 78- 82, 26-29 April 2004.
- [8] K. Manoj, “MEMS: Theory and Usage in Industrial and Consumer Electronics,” Central Scientific Instruments Organization, March 2010.
- [9] Draper Laboratory, “The Draper Technology Digest,” vol. 10, pp. 3, 2006, <http://www.draper.com>, reached on 10.01.2012
- [10] N. Yazdi, F. Ayazi, and K. Najafi, “Micromachined Inertial Sensors,” *Proceedings of the IEEE*, vol. 86, no. 8, pp. 1640-1659, Aug 1998.

- [11] S. Tadigadapa and K. Mateti, "Piezoelectric MEMS Sensors: State-of-the-art and Perspectives," *Meas. Sci. Technol.*, vol. 20, no. 9, p. 92001, Jul 2009.
- [12] I. E. Ocak, "A Tactical Grade MEMS Accelerometer," *PhD. Thesis*, Middle East Technical University, Sept 2010.
- [13] L. Chang, "Foundations of MEMS," Prentice Hall, Aug 2005.
- [14] H. Seidel, U. Fritsch, R. Gottinger, J. Schalk, J. Walter, and K. Ambaum, "A Piezoresistive Silicon Accelerometer with Monolithically Integrated CMOS-circuitry," *Tech. Dig. 8<sup>th</sup> Int. Conf. Solid-State Sensors and Actuators (Transducers '95)*, vol. 1, pp. 597-600, 25-29 Jun 1995.
- [15] H. R. Shea, "Reliability of MEMS for Space Applications," *Reliability, Packaging, Testing and Characterization of MEMS/MOEMS, proc. of SPIE*, vol. 6111, 2006.
- [16] S. Sung, J. G. Lee, B. Lee, and T. Kang, "Design and Performance Test of an Oscillation Loop for a MEMS Resonant Accelerometer," *J. Micromech. Microeng.*, vol. 13, pp. 246–253, 2003.
- [17] I. Kim, S. Seok, H. C. Kim, M. K. Kang, and K. Chun, "Wafer Level Vacuum Packaged Out-of-plane and In-plane Differential Resonant Silicon Accelerometers for Navigational Applications," *J. Semicond. Technol. Sci.*, vol. 5, pp. 58–66, 2005.
- [18] T. Cui and J. Wang, "Polymer-based Wide-bandwidth and High-sensitivity Micromachined Electron Tunneling Accelerometers Using Hot Embossing," *J. Microelectromech. Syst.*, vol. 14, no. 5, pp. 895-902, Oct. 2005.
- [19] C. Yeh and K. Najafi, "A Low-voltage Bulk-silicon Tunneling Based Microaccelerometer," *IEEE Int. Electron Devices Meeting (IEDM)*, pp. 593–596, 10-13 Dec. 1995.
- [20] V. Milanovic, E. Bowen, N. Tea, J. Suehle, B. Payne, M. Zaghoul, and M. Gaitan, "Convection-based Accelerometer and Tilt Sensor Implemented in Standard CMOS," *Proc. IEEE*, pp. 487–90, 1998.

- [21] R. Hiratsuka, D. C. van Duyn, T. Otaredian, and P. de Vries, "A Novel Accelerometer Based on a Silicon Thermopile," *Tech. Dig. 6<sup>th</sup> Int. Conf. Solid-State Sensors and Actuators (Transducers '91)*, pp. 420-423, 24-27 Jun 1991.
- [22] G. Zang, H. Xie, L. E. de Rosset, and G. K. Fedder, "A Lateral Capacitive CMOS Accelerometer with Structural Curl Compensation," *Tech. Dig. 12<sup>th</sup> IEEE Int. Conf. Micro Electro Mechanical System (MEMS'99)*, pp. 606-611, 17-21 Jan 1999.
- [23] H. Xie and G. K. Fedder, "CMOS Z-axis Capacitive Accelerometer with Comb-finger Sensing," *Tech. Dig. 12<sup>th</sup> IEEE Int. Conf. Micro Electro Mechanical System (MEMS'00)*, pp. 496-501, 23-27 Jan 2000.
- [24] H. Luo, G. K. Fedder, and L. R. Carley, "1 mG Lateral CMOS-MEMS Accelerometer," *Proc. 13<sup>th</sup> Annu. Int. Conf. (MEMS'00)*, pp. 502-507, 23-27 Jan 2000.
- [25] H. Qu, D. Fang, and H. Xie, "A Single-crystal Silicon 3-axis CMOS-MEMS Accelerometer," *Proc. IEEE Sens.*, pp. 661-664, 24-27 Oct 2004.
- [26] J. Wu, G. K. Fedder, and L. R. Carley, "A Low-noise Low-offset Capacitive Sensing Amplifier for a 50  $\mu\text{g}/\sqrt{\text{Hz}}$  Monolithic CMOS-MEMS Accelerometer," *IEEE J. of Solid-State Circuits*, vol. 39, pp. 722-730, May 2004.
- [27] J. M. Tsai and G. K. Fedder, "Mechanical Noise-limited CMOS-MEMS Accelerometers," *Micro Electro Mechanical Systems (MEMS), 2005 IEEE 18<sup>th</sup> International Conference on*, pp. 630- 633, 30 Jan-3 Feb 2005.
- [28] C. Wang, M. H. Tsai, C. M. Sun, and W. Fang, "A Novel CMOS Out-of-Plane Accelerometer with Fully-differential Gap-closing Capacitance Sensing Electrodes," *Journal of Micromechanics and Microengineering*, vol. 17, pp. 1275-1280, July 2007.
- [29] H. Qu, D. Fang, and H. Xie, "A Monolithic CMOS-MEMS 3-axis Accelerometer with a Low-noise, Low-power Dual-chopper Amplifier," *Sensors Journal, IEEE*, vol. 8, no. 9, pp.1511-1518, Sept. 2008.

- [30] M. H. Tsai, Y. C. Liu, C. M. Sun, C. Wang, C. W. Cheng, and W. Fang, "A  $400 \times 400 \mu\text{m}^2$  3-axis CMOS-MEMS Accelerometer with Vertically Integrated Fully-differential Sensing Electrodes," *Solid-State Sensors, Actuators and Microsystems Conference (Transducers'11), 2011 16<sup>th</sup> International*, pp. 811-814, 5-9 June 2011.
- [31] B. V. Amini, S. Pourkamali, M. Zaman, and F. Ayazi, "A New Input Switching Scheme for a Capacitive Micro-g Accelerometer," *VLSI Circuits, 2004. Digest of Technical Papers. Symposium on*, pp. 310- 313, 17-19 June 2004.
- [32] B. V. Amini and F. Ayazi, "A 2.5-V 14-bit  $\Sigma\Delta$  CMOS SOI Capacitive Accelerometer," *Solid-State Circuits, IEEE Journal of*, vol. 39, no. 12, pp. 2467-2476, Dec 2004.
- [33] B. V. Amini and F. Ayazi, "Micro-gravity Capacitive Silicon-on-Insulator Accelerometers," *J. Microelectromech. Syst.*, vol. 15, no. 11, p. 2113, Nov 2005.
- [34] B. V. Amini, R. Abdolvand, and F. Ayazi, "A 4.5-mW Closed-loop  $\Sigma\Delta$  Micro-gravity CMOS SOI Accelerometer," *Solid-State Circuits, IEEE Journal of*, vol. 41, no. 12, pp. 2983-2991, Dec 2006.
- [35] V. Milanovic, M. Last, and K. S. J. Pister, "Torsional Micromirrors with Lateral Actuators," *Proc. Transducers'01-Euroensors XV Conf.*, pp. 1298.1301, 2001.
- [36] T. Tsuchiya and H. Funabashi, "A Z-axis Differential Capacitive SOI Accelerometer with Vertical Comb Electrodes," *Micro Electro Mechanical Systems (MEMS), 2004 IEEE 17<sup>th</sup> International Conference on*, pp. 524- 527, 2004.
- [37] H. Hamaguchi, K. Sugano, T. Tsuchiya, and O. Tabata, "A Differential Capacitive Three-axis SOI Accelerometer using Vertical Comb Electrodes," *Tech. Dig. 20<sup>th</sup> Int. Conf. Solid-State Sensors and Actuators (Transducers'07)*, pp. 1483-1486, 10-14 June 2007.
- [38] Y. C. Hsu, C. W. Lin, C. M. Sun, C. P. Hsu, Y. T. Lee, M. H. Tsai, Y. C. Liu, and W. Fang, "Implementation of Fully-differential Capacitance Sensing Accelerometer using Glass Proof-mass with Si-vias," *Micro Electro Mechanical*

*Systems (MEMS), 2011 IEEE 24<sup>th</sup> International Conference on*, pp. 589-592, 23-27 Jan 2011.

[39] T. Tekin, H. D. Ngo, O. Wittler, B. Bouhlal, and K. D. Lang, "Packaging of MEMS/MOEMS and Nanodevices: Reliability, Testing, and Characterization Aspects," *Proceedings of the SPIE*, vol. 7928, pp. 792805-792805-10, Feb 2011.

[40] W. T. Thomson and M. D. Dahleh, "Theory of Vibration with Applications," *Prentice Hall*, 1998.

[41] T. B. Gabrielson, "Mechanical-Thermal Noise in Micromachined Acoustic and Vibration Sensors," *IEEE Trans. Electron Dev.*, vol. 40, no. 5, pp. 903-909, May 1993.

[42] A. R. Sankar, "Performance Enhancement of a Silicon MEMS Piezoresistive Single Axis Accelerometer with Electroplated Gold on a Proof Mass," *J. Micromech. Microeng.*, vol. 19, no. 2, p. 025008, Feb 2009.

[43] R. Lifshiz and M. L. Roukes, "Thermoelastic Damping in Micro- and Nanomechanical Systems," *Phys. Rev. B*, vol. 61, no. 8, pp. 5600–5609, Mar 2000.

[44] Z. Hao, A. Erbil., and F. Ayazi, "An Analytical Model for Support Loss in Micromachined Beam Resonators with in-plane Flexural Vibrations," *Sens. Actuators A, Phys.*, vol. 109, no. 1, pp. 156–164, Dec 2003.

[45] J. Yang, T. Ono, and M. Esashi, "Energy Dissipation in Submicrometer Thick Single-crystal Silicon Cantilevers," *J. Microelectromech. Syst.*, vol. 11, no. 6, pp. 775–783, Dec 2002.

[46] C. Acar, "Robust Micromachined Vibratory Gyroscopes," *PhD. Dissertation*, University of California Irvine, 2004.

[47] A. Wung, R. V. Park, K. J. Rebello, and G. K. Fedder, "Tri-axial High-g CMOS-MEMS Capacitive Accelerometer Array," *Micro Electro Mechanical Systems, 2008. MEMS 2008. IEEE 21<sup>st</sup> International Conference on*, pp. 876-879, 13-17 Jan 2008.

- [49] C. P. Hsu, Y. C. Hsu, M. C. Yip, and W. Fang, "A Novel SOI-based Single Proof-mass 3-axis Accelerometer with Gap-closing Differential Capacitive Electrodes in All Sensing Directions," *Sensors, 2010 IEEE*, pp. 1188-1191, 1-4 Nov 2010.
- [50] K. Shah, A. Zayegh, and J. Singh, "Modeling and Analysis of Fringing and Metal Thickness Effects in MEMS Parallel Plate Capacitors," *SPIE conference on Microelectronics, MEMS, and Nanotechnology*, 11-14 Dec 2005.
- [51] M. M. Torunbalci, E. Tatar, S. E. Alper, and T. Akin, "Comparison of Two Alternative Silicon-On-Glass Microfabrication Processes for MEMS Inertial Sensors," *Euroensors XXV*, vol. 25, pp. 900–903, 4-7 Sept 2011.
- [52] C. Iliescu and F. E. H. Tay, "Wet Etching of Glass," *Semiconductor Conference, 2005.CAS 2005 Proceedings. 2005 International*, vol. 1, pp. 35- 44, 3-5 Oct 2005
- [53] W. H. Ko, J. T. Suminto, and G. J. Yeh, "Bonding Techniques for Microsensors," *Elsevier*, 1985.
- [54] E. Tatar, M. M. Torunbalci, S. E. Alper, and T. Akin, "A Method and Electrical Model for the Anodic Bonding of SOI and Glass Wafers," *Micro Electro Mechanical Systems (MEMS), 2012 IEEE 25<sup>th</sup> International Conference on*, 29 Jan-2 Feb 2012.
- [55] S. E. Kucuk, "Development of High Fill Factor and High Performance Uncooled Infrared Detector Pixels," *M. Sc. Thesis*, Middle East Technical University, Sept 2011.
- [56] M. A. George, Q. C. Bao, I. W. Sorensen, W. S. Glaunsinger, and T. Thundat, "Thermally Induced Changes in the Resistance, Microstructure, and Adhesion of Thin Gold Films on Si/SiO<sub>2</sub> Substrates," *Journal of Vacuum Science &Technology A: Vacuum, Surfaces, and Films*, vol. 8, no. 3, pp. 1491-1497, May 1990.
- [57] U. Sönmez, "Capacitive Readouts for High Performance MEMS Accelerometers," *M. Sc. Thesis*, Middle East Technical University, Feb 2011.